Simulation of Bubbly Flow in a Flat Bubble Column

Evaluation of Interface and Turbulence Closure Models

by

A.C.L Nygren

In partial fulfilment of the requirements for the degree of
Master of Science in Chemical Engineering

at Lund University, Faculty of Engineering

Examiner:	Prof. B. Nilsson	Lund University
Supervisors:	Prof. H. E. A. Van den Akker	TU Delft
	Dr. A. Holmqvist	Lund University

Lunds universitet
Lunds Tekniska Högskola

Abstract

Numerical, transient simulations of a meandering bubble plume in a rectangular flat bubble column was carried out, using the commercial CFD package ANSYS Fluent 15 within the framework of a Eulerian-Eulerian description. A Sensitivity analysis of turbulence closure was performed using four turbulence models: standard, RNG, Realizable $k-\epsilon$ and the Reynolds stress model. The effect of dispersed phase turbulence on the continuous phase was also investigate. The interaction force term included drag, virtual mass and turbulent dispersion. Some simulations were also made using lift and wall lubrication forces. The available drag and dispersion models available in Fluent were evaluated. Lastly, the impact of numerical methods was investigated where the model was tested for discretization scheme, gradient limiter, time step and grid size.

The standard and Realizable $k-\epsilon$ models resultsed in a meandering bubble plume that oscillated with a period of 32.5 seconds. The Reynolds stress model did not reach a quasi-steady state, as the period kept increasing during the flow-time. The RNG $k-\epsilon$ model produced an oscillating plume, but the recorded time series show that the velocity fluctuated in a more chaotic way. The analysis of the dispersed phase turbulence modelling showed that the chaotic oscillations predicted by the RNG $k-\epsilon$ was a results of under predicting the turbulent viscosity. Comparing drag models showed that the drag coefficient influenced the amplitude of the velocity measurements, and that higher drag coefficient yield a higher amplitude. It was also found that including the turbulent dispersion force is imperative to capture the dispersion of the bubble plume. The lift force did not influence the oscillation frequency of the plume, but only the dispersion. Including caused the non-physical effect of pushing the bubbles towards the back and forth wall. It was also shown that this effect could be counteracted by including wall lubrication, and keeping the dispersive effect of the lift force. The choice of time step had the largest impact on the oscillation frequency. Decreasing the time step below 4 ms caused the oscillation frequency to decrease rapidly. If a time step of 2.5 ms was used, the time between peaks doubled.

Contents

1 Introduction **1**
- 1.1 Project Overview . . . 1
- 1.2 Research Objective . . . 2
- 1.3 Project Approach . . . 2

2 Theory **5**
- 2.1 Hydrodynamics . . . 5
- 2.2 Multiphase Flow . . . 5
  - 2.2.1 Eulerian - Eulerian Modeling Approach . . . 6
- 2.3 Interaction Forces . . . 7
  - 2.3.1 Drag . . . 7
    - 2.3.1.1 Schiller Nauman Model . . . 7
    - 2.3.1.2 Morsi Alexander Drag Model . . . 8
    - 2.3.1.3 Grace *et al.* Model . . . 8
    - 2.3.1.4 Tomiyama Drag Model . . . 9
    - 2.3.1.5 Universal Drag Model . . . 9
  - 2.3.2 Virtual Mass Force . . . 10
  - 2.3.3 Lift . . . 10
  - 2.3.4 Wall Lubrication . . . 10
  - 2.3.5 Turbulent Dispersion . . . 11
    - 2.3.5.1 Simonin . . . 11
    - 2.3.5.2 Diffusion in VOF . . . 11
- 2.4 Turbulence . . . 11
  - 2.4.1 Introduction . . . 11
  - 2.4.2 Reynolds Averaging . . . 12
  - 2.4.3 Turbulence Modeling . . . 13
    - 2.4.3.1 Bossinesque Hypothesis . . . 13
    - 2.4.3.2 Standard $k-\epsilon$ Model . . . 13
    - 2.4.3.3 $k-\epsilon$ ReNormalisation Group . . . 14
    - 2.4.3.4 Realizable $k-\epsilon$ Model . . . 15
    - 2.4.3.5 Reynolds Stress Model . . . 16
    - 2.4.3.6 Near Wall Modeling . . . 18
    - 2.4.3.7 Turbulent Two-Way Coupling . . . 18
    - 2.4.3.8 Simonin et al. . . . 18
    - 2.4.3.9 Troshko-Hassan . . . 19
    - 2.4.3.10 Sato . . . 19
- 2.5 Numerical Methods . . . 20
  - 2.5.1 Spatial Discretization . . . 20
    - 2.5.1.1 Second Order Upwind . . . 20
    - 2.5.1.2 Quadratic Upwind Interpolation (QUICK) . . . 20
    - 2.5.1.3 Gradient Limiter . . . 21
  - 2.5.2 Temporal Discretization . . . 21
  - 2.5.3 Pressure - Velocity Coupling . . . 21

3 Case Studies **23**
- 3.1 Experimental Studies . . . 23
  - 3.1.1 The Becker Case . . . 23
    - 3.1.1.1 Experimental Setup . . . 23
    - 3.1.1.2 Results and Conclusions . . . 23
    - 3.1.1.3 Other Studies . . . 23

3.1.2 The Deen Case . . . 26
3.1.2.1 Experimental Setup . . . 26
3.1.2.2 Results and Conclusions . . . 26
3.2 Numerical Studies . . . 29
3.2.1 Results with Laminar Models . . . 29
3.2.2 Results with Turbulence Models . . . 29
3.2.3 Results with Large Eddy Simulations . . . 31

4 Computational Setup **33**
4.1 Introduction . . . 33
4.2 Case Setup . . . 33
4.2.1 Physical Properties . . . 33
4.2.2 Computational Grid . . . 33
4.2.3 Boundary Condition . . . 33
4.2.3.1 Wall . . . 33
4.2.3.2 Inlet . . . 35
4.2.3.3 Outlet . . . 35
4.2.4 Initial Conditions . . . 36

5 Results and Discussion **37**
5.1 Influence of turbulence model . . . 37
5.2 Influence of spatial discretization . . . 43
5.3 Influence of drag model . . . 44
5.4 Influence of turbulent two-way coupling . . . 48
5.5 Influence of Turbulent Dispersion . . . 51
5.6 Influence of Lift- and Wall Lubrication Force . . . 52
5.7 Influence of time step . . . 55
5.8 Influence of grid size . . . 56

6 Conclusions and Recommendations **59**
6.1 Fluent Development . . . 59
6.2 Turbulence Modelling . . . 59
6.3 Interaction Force . . . 60
6.4 Numerical Methods . . . 60
6.5 Conclusions . . . 60

A Estimating the Terminal Velocity of a Rising Bubble **63**

B Initial Values **65**

Bibliography **67**

1

INTRODUCTION

1.1. PROJECT OVERVIEW

Gas-liquid reactors are commonly used in many industrial applications. Examples of industrial applications include the Hyrdogenation, Chloration and gas absorption processes. This type of reactor is commonly refereed to as a "Bubble Column". A bubble column usually takes the form of a cylindrical tank with aspect ratios between 2 and 10. The gas is injected at the bottom of the column through a sparger into the continuous liquid. The buoyancy forces on gas itself provides the stirring action of the column, thus eliminating the need for any moving stirring parts in the reactor. This often provides a very cost effective solution.

The complex fluid dynamics of the multiphase flow in bubble columns makes it hard to predict the flow pattern, and design of bubble columns are usually made by performing experiments and then scaling up the results. And even through experimental scale up it has proven to be a difficult task to estimate important design parameters such as superficial velocity, hold-up, interfacial area and mass transfer coefficients [1, 2]

During the last two decades a lot of progress has been made in the field of Computational Fluid Dynamics (CFD). CFD enables the user to utilize numerical techniques to predict the spatial and temporal distribution of flow variables, thus gaining valuable information that can be either difficult, expensive or even impossible to obtain by experiments. CFD simulations of multiphase flow, such as bubble columns provide several additional challenges compared to single phase flow. The main issue is the increased complexity of the fluid dynamics, but there are also added issues with the numerics. It has also generally accepted that to fully capture the dynamic nature of the gas-liqud flow, the simulations has to be made in 3 dimensions [3, 4]. One issue is that multiphase flow modelling involves a lot more empirical models compared to modelling single phase flow. This presents an issue to the user of any CFD software. Which empirical model should be chosen, and has it been properly validated?. Therefore it is of paramount importance to investigate the effects using different models.

1.2. RESEARCH OBJECTIVE

The research question posed for this study reads as follows:

> How well can Ansys Fluent, as the leading industrial and academic CFD code, predict the flow field of a gas-liquid bubble column. Loncle [4] did a similar study in 1999 using Fluent 4.4. How has Fluent developed during the last 15 years? How is the solution influenced by factors such as:
>
> - Grid Size
> - Time Step
> - Interfacial Closure Model
> - Turbulence Closure Model
> - Discretization Schemes

This will be investigated by performing a systematic sensitivity analysis on the parameters that was mentioned above. The results will then be compared to experimental data. The experiments performed by Becker *et al.* [5] will be used as a benchmark for comparing simulated data. It comprises a very interesting system for benchmarking CFD models of bubbly flow since it reacts very strongly to changes in physical models and numerical schemes[4]. The Becker case will be described in further detail in chapter 3.

1.3. PROJECT APPROACH

This study is split into three different parts. Firstly, the benchmark geometry has to be represented as a CAD model, and then discretized on an appropriately sized grid . Secondly, the physics of the system has to be represented using mathematical models. Lastly, the numerical methods that is used to solve the discretized mathematical model has to be chosen. A schematic overview of the project approach is shown in figure 1.1. The report will be structured as follows:

- **Chapter 2** will present the underlying theory that is necessary to model multiphase flow using a Eulerian-Eulerian approach.
- **Chapter 3** will present previous experimental and numerical studies that have been made on rectangular and square bubble columns
- **Chapter 4** will present the details of the numerical setup used in ANSYS Fluent.
- **Chapter 5**, will present all results from this study.
- **Chapter 6** will present the final conclusions and recommendations for further work.

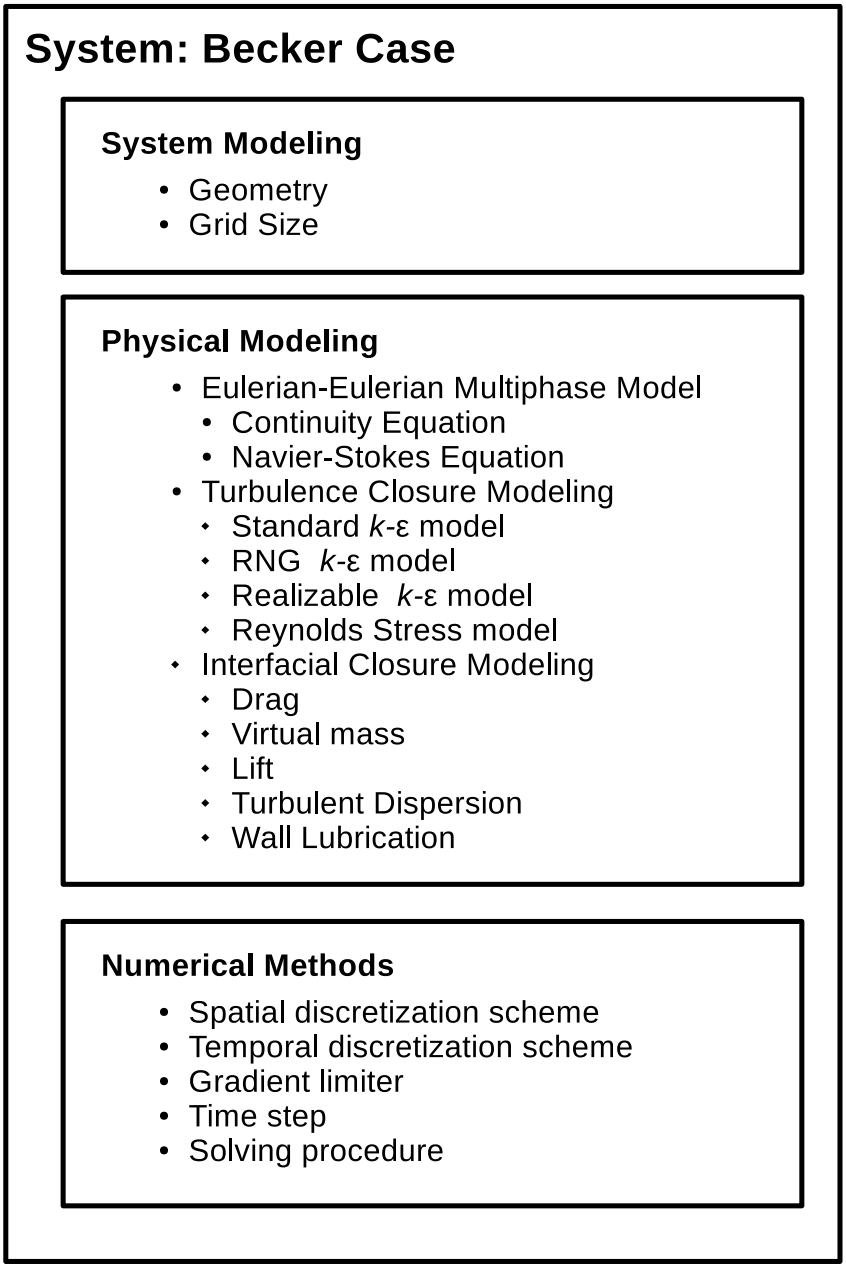

Figure 1.1: Schematic overview of the three different stages of the project.

2

THEORY

In this chapter the necessary theory for simulating two-phase flow will be explained.

2.1. HYDRODYNAMICS

Before introducing the theory of two-phase flow, it is necessary to first explain the governing equations for single phase flow.

Fluid flow is governed by the continuity equation and the Navier-Stokes equation, which represents the conservation of mass and momentum respectively. These equations can be derived directly from first principles[6].

Continuity Equation

$$\frac{\partial \rho}{\partial t} + \nabla \rho \mathbf{u} = 0 \tag{2.1}$$

Navier-Stokes Equation

$$\frac{\partial \rho \mathbf{u}}{\partial t} + \nabla \cdot (\rho \mathbf{v}\mathbf{v}) = -\nabla p + \nabla \cdot \mathbf{T} + \mathbf{f} \tag{2.2}$$

In equation 2.2 $\mathbf{T}$ is the fluid stress tensor, and $\mathbf{f}$ are the body forces acting on the fluid, which usually contains gravity. For a Newtonian fluid, the stresses are proportional to the mean strain rate:

$$\mathbf{T} = \mu \left(\nabla \mathbf{u} + (\nabla \mathbf{u})^T - \frac{2}{3} \nabla \cdot \mathbf{u} I \right) \tag{2.3}$$

The right term in equation 2.3 accounts for the compressibility of the fluid. If the fluid is in-compressible, the term disappears.

2.2. MULTIPHASE FLOW

A multiphase flow is defined as a flow with two or more phases that are separated by an interface. All multiphase flows regimes can be classified either dispersed, mixed or separated[7]. In a dispersed multiphase flow, all phases except one are dispersed (discontinuous) in a continuous fluid. In separated multiphase flows, the phases flow in a semi-continuous mode. The phases are separated by an interface, but none of the phases exists in a particulate form inside the other. A mixed multiphase flow is a combination of dispersed and separated, where dispersed particles and semi-continuous interfaces coexist. Different flow regimes require different modeling approaches, thus it is important to classify the flow in question before choosing modeling approach. Examples of different multiphase flows are shown in table 2.1.

In principle there are two approaches to modeling a dispersed two phase system.

- Eulerian-Lagrangian
- Eulerian-Eulerian

Table 2.1: Classification of multiphase flow regimes

Flow Regime	Dispersed	Mixed	Separated
	Bubbly Flow	Droplet Annular Flow	Film Flow
	Particle Laden Flow	Bubbly Annular Flow	Annular Flow
	Droplet Flow	Slug Flow	Jet Flow

The names Eulerian and Lagrangian referees to the frame of reference in which the governing equations are formulated. In a Eulerian frame of reference an observer is stationary, whilsti in a Lagrangian frame of reference an observer moves with the flow. In the Eulerian-Lagrangian approach the continuous fluid is treated in a Eulerian frame of reference, whilst the dispersed phase is treated in a Lagrangian frame of reference. In the Eulerian-Eulerian approach the continuous and dispersed phase are viewed as a interpenetrating continua.

2.2.1. EULERIAN - EULERIAN MODELING APPROACH

The Eulerian - Eulerian modeling approach starts with assuming that all the materials involved can be described as a continuum. The motion of each material is then governed by equations 2.1 and 2.2. The conservation of mass and momentum at the interface are expressed by jump conditions[8].

Jump condition for mass

$$\rho(\mathbf{u}_i - \mathbf{u}_{i,\text{Int}}) \cdot \mathbf{n} = 0 \tag{2.4}$$

Jump condition for momentum

$$\rho \mathbf{u}_i(\mathbf{u}_i - \mathbf{u}_{i,\text{int}}) \cdot \mathbf{n} - \mathbf{T} \cdot \mathbf{n} = \sigma \kappa \mathbf{n} \tag{2.5}$$

Where $u_{i,Int}$ is the velocity of the interface, σ is the surface tension, κ is the mean curvature of the interface and $\mathbf{n}$ is the unit normal. Equations 2.1 and 2.2 can be used together with the jump conditions for mass and momentum to provide an exact description of the flow and the evolution of the interface on a microscopic level. However for industrial flows with many dispersed particles, the computational needs for such a simulation would be extreme. To circumvent this, the equations 2.1 and 2.2 can be averaged to remove the details of the flow. The averaging procedure is outside the scope of this work, but detailed derivations of the averaged equations can be found in literature[7–10].

This means that the Eulerian-Eulerian modeling approach treats both the continuous and the dispersed phases as an interpenetrating continua instead of tracking individual particles. Each cell in the discritized domain contains a certain volume fraction of each phase, and for every phase a set of averaged governing equations are written down. The sub-script q denotes the phase, where $q = 1$ referees to the continuous phase, and $q = 2$ referees to the dispersed phase. The averaged continuity and Navier-Stokes equation for phase q reads as follows:

Averaged Continuity Equation

$$\frac{\partial}{\partial t}\left(\alpha_q \rho_q\right) + \nabla \cdot \left(\alpha_q \rho_q \mathbf{u}_q\right) = 0 \tag{2.6}$$

Averaged Navier-Stokes Equation

$$\frac{\partial}{\partial t}(\alpha_q \rho_q \mathbf{u}) + (\alpha_q \rho_q \mathbf{u}) \cdot \nabla \mathbf{u} = -\alpha_q \nabla p + \nabla \mathbf{T}_q + \mathbf{F}_q + \mathbf{I}_q \tag{2.7}$$

Here $\mathbf{T}_q$ denotes the stress tensor for phase q. For a Newtonian fluid $\mathbf{T}_q$ is given by[11]:

$$\mathbf{T}_q = \alpha_q \mu_q (\nabla \mathbf{u}_q + \nabla \mathbf{u}_q^T) - \frac{2}{3} \alpha_q \mu_q \nabla \cdot \mathbf{u}_q I \tag{2.8}$$

To close the equations, averaged jump conditions for mass and momentum are also required.

Averaged Jump condition for mass

$$\sum_{i=1}^{n} \alpha_i = 1 \tag{2.9}$$

Averaged jump condition for momentum

$$\sum_{i=1}^{n} \mathbf{I}_i = 0 \tag{2.10}$$

$\mathbf{I}_q$ represent the interface interaction forces, which describes the interaction force between the phases. This term is the most important characteristic of feature of multiphase flow. Since $\mathbf{I}_q$ is unknown it has to be modeled. This is done by separating the interaction force in different contributing terms. In literature the following interface interaction forces are usually discussed[10, 12, 13].

- Drag
- Virtual Mass
- Lift
- Wall Lubrication
- Turbulent Dispersion

The interaction force term is then given as follows:

$$\mathbf{I}_1 = -\mathbf{I}_2 = \mathbf{I}_d + \mathbf{I}_{vm} + \mathbf{I}_l + \mathbf{I}_{wl} + \mathbf{I}_{td} \tag{2.11}$$

All of individual terms in the interaction force will be described in detail below.

2.3. INTERACTION FORCES

2.3.1. DRAG

When a bubble rises in a surrounding fluid, it is accelerated due to buoyancy. But due to friction drag between the surface of the bubble and the surrounding liquid, it is also decelerated. The drag term is the dominant contribution in the interaction force term, and is in many cases the only force that is taken into account. The inter-phase momentum transfer due to friction drag between phase can be formulated as follows[11]:

$$\mathbf{I}_d = K_{pq}(\mathbf{u}_p - \mathbf{u}_q) \tag{2.12}$$

The proportionality constant K_{pq} is refereed to as the interphase exchange coefficient, and for a fluid-fluid system Fluent defines it as follows:

$$K_{pq} = \frac{C_D \mathrm{Re}_B A_i \mu_q}{8 d_p} \tag{2.13}$$

A_i is the interfacial area concentration which is defined as the interfacial area between phases per unit mixture. Ansys Fluent calculates it using the following algebraic equation:

$$A_i = \frac{6\alpha_p(1-\alpha_p)}{d_p} \tag{2.14}$$

The bubble Reynolds number is defined with the relative velocity between phases as the characteristic velocity:

$$\mathrm{Re}_B = \frac{\rho_1 |\mathbf{u}_2 - \mathbf{u}_2| d_p}{\mu_1} \tag{2.15}$$

C_D is used to quantify the drag force between the phases, and has to be modeled. For this purpose there exists several different models.

SCHILLER NAUMAN MODEL

Schiller and Nauman propsed the following analytical expression for the drag coefficient of a single rigid sphere[14]:

$$C_D = \begin{cases} 24(1 + 0.15\mathrm{Re}^{0.687})/\mathrm{Re} & \mathrm{Re} \leq 1000 \\ 0.44 & \mathrm{Re} > 1000 \end{cases}$$

The model attempts to fit an analytical expression to the standard experimental drag curve for a sphere. The Schiller Nauman model can also be viewed as Stokes law with an empirical correction factor to account for higher Reynolds number effects.

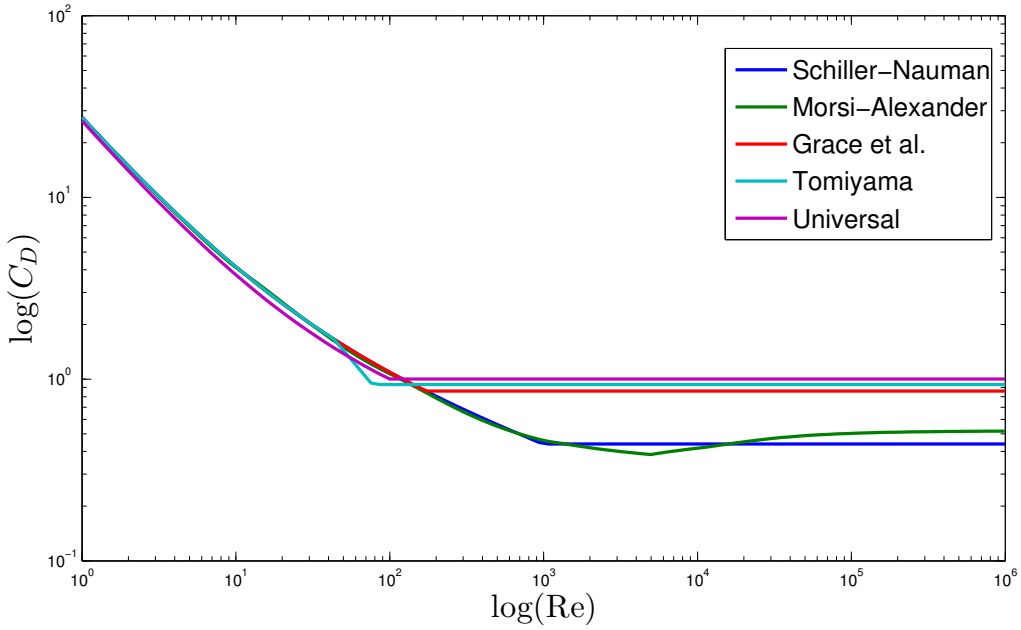

Figure 2.1: Drag coefficient as a function of the Reynolds number for different drag models

MORSI ALEXANDER DRAG MODEL

The Morsi Alexander drag model[15] defines the drag coefficient as:

$$C_D = a_1 + \frac{a_2}{\mathrm{Re}} + \frac{a_3}{\mathrm{Re}^2} \tag{2.16}$$

Where the constants a_1, a_2 and a_3 depends on the Reynolds number. The values of a_1, a_2 and a_3 for different intervals of Reynolds Numbers are listed in table 2.2 Just like the Schiller-Naumann model, the Morsi-Alexander model is also based on the experimental drag curve for a single, rigid, spherical particle[15]. The Morsi-Alexander model improves upon the Schiller-Naumann model by adjusting the expression for a wider range of Reynolds numbers. Thus better capturing the shape of the experimental drag curve for a sphere.

GRACE *et al.* MODEL

The Schiller-Naumann and Morsi-Alexander models both assumes a rigid, spherical particle. A bubble is not rigid, and it deforms to a non spherical shape from external forces. The shape of the bubble will affect the drag coefficient, thus for a bubbly flow the deformation of a bubble should be incorporated in the modeling of the drag coefficient. Grace et al [16] showed that the terminal velocity of a single bubble, rising in a stagnant liquid could be correlated with the bubble Reynolds number (equation 2.15), the Eotvos number and the

Table 2.2: Constants for different intervals of the Reynolds number for the Morsi Alexander drag model

Reynolds Number Interval	a_1	a_2	a_3
$0 < \mathrm{Re} \leq 0.1$	0	24	0
$0.1 < \mathrm{Re} \leq 1$	3.690	22.73	0.0903
$1 < \mathrm{Re} \leq 10$	1.222	29.1667	−3.8889
$10 < \mathrm{Re} \leq 10^1$	0.6167	46.50	-116.67
$10^2 < \mathrm{Re} \leq 10^3$	0.3644	98.33	−2778
$10^3 < \mathrm{Re} \leq 5 \times 10^3$	0.357	148.62	−47 500
$5 \times 10^3 < \mathrm{Re} \leq 10^4$	0.46	−490.546	578 700
$\mathrm{Re} \geq 10^5$	0.5191	−1662.5	5 416 700

Morton number. The Eotvos number is the ratio between buoyancy and surface tension forces:

$$\mathrm{Eo} = \frac{g(\rho_1 - \rho_2)d_p^2}{\sigma} \tag{2.17}$$

The Morton number is the property group of the two phases:

$$\mathrm{Mo} = \frac{g\mu_1^4(\rho_1 - \rho_2)}{\rho_1^2\sigma^3} \tag{2.18}$$

Where σ denotes the surface tension between the phases. The drag coefficient is also affected by the degree of contamination by surfactants at the interface. If the interface is contaminated, the bubbles will behave more like rigid spheres[16]. In an industrial system the interface will always be contaminated. This is the reason why rigid sphere models like Schiller-Nauman and Morsi Alexander usually perform reasonably well for bubbly flows[17]. For Bubbles in the ellipsoidal regime (Eo < 40[16]), Grace *et al* proposed the following relation between C_D, Eo and Mo for terminal conditions:

$$C_{D_{Ellipse}} = \frac{4}{3}\sqrt{\frac{\mathrm{Eo}^3}{\mathrm{Mo}}}\frac{\mathrm{Mo}^{0.298}}{\left[3.42\left(\frac{4}{3}\mathrm{EoMo}^{-0.149}\left(\frac{\mu_1}{\mu^*}\right)\right)^{-0.14} - 0.857\right]^2} \tag{2.19}$$

In Ansys Fluent the Grace *et al.* model is implemented as[11]:

$$C_D = \max(\min(C_{D_{ellipse}}, C_{D_{cap}}), C_{D_{sphere}}) \tag{2.20}$$

This implementation adjusts the drag model according to the shape of the bubble. At lower Reynolds numbers, $C_{D_{Sphere}}$ is used, which is calculated using the model by Schiller and Nauman. For high Eotvos numbers, the bubbles are in the capped regime. Capped bubbles will generate more form drag than spherical or elliptical bubbles at terminal conditions, and the following model is used in the capped regime:

$$C_{D_{Cap}} = \frac{8}{3} \tag{2.21}$$

The Grace *et al.* model significantly improves upon the Schiller Nauman and Morsi Alexander models by adjusting C_D over a wide range of shapes. However the expressions are more complicated, and they will be harder for a CFD-code to evaluate.

TOMIYAMA DRAG MODEL

The model by Tomiyama *et al.* [17] tries to address the same shortcomings of the rigid sphere models as Grace *et al.* [16].

$$C_D = \max\left(\min\left(\frac{24}{\mathrm{Re}}\left(1 + 0.15\mathrm{Re}^{0.687}\right), \frac{72}{\mathrm{Re}}\right), \frac{8}{3}\frac{\mathrm{Eo}}{\mathrm{Eo}+4}\right) \tag{2.22}$$

UNIVERSAL DRAG MODEL

The universal drag law can be used for a range of different multiphase regimes. For bubbly flow it is defined as [11]:

$$C_{D_{\mathrm{Vis}}} = \frac{24}{\mathrm{Re}}(1 + 0.1\mathrm{Re}^{0}.75) \tag{2.23}$$

$$C_{D_{\mathrm{Dis}}} = \frac{2}{3}\frac{d_p}{\mathrm{RT}}\left[\frac{1 + 17.67f^{*6/7}}{18.67f^*}\right]^2 \qquad f^* = (1-\alpha_p)^{1.5} \tag{2.24}$$

$$C_{D_{\mathrm{cap}}} = \frac{8}{3}(1-\alpha_p)^2 \tag{2.25}$$

Where λ_{RT} is the Rayleigh-Taylor instability wave length, defined as:

$$\lambda_{\mathrm{RT}} = \left(\frac{\sigma}{g|\rho_q - \rho_p|}\right)^{0.5} \tag{2.26}$$

As seen above the model differentiates between a viscous, distorted and capped bubble regime. The flow regime influences the shape of the bubbles, which in turn influences the drag coefficient. For the viscous regime, the following condition is satisfied:

$$C_{D_{\text{Dis}}} < C_{D_{\text{Vis}}}$$

In the distorted regime the following condition is satisfied:

$$C_{D_{\text{Vis}}} C_{\text{Vis}} < C_{D_{\text{Dis}}} < C_{D_{\text{Cap}}}$$

In the capped regime the following condition is satisfied:

$$C_{D_{\text{Dis}}} > C_{D_{\text{Cap}}}$$

It is worth noting that the universal drag model incorporates the volume fraction a parameter.

2.3.2. VIRTUAL MASS FORCE

The virtual mass effect occurs when the dispersed phase is accelerated relative to the continuous phase. When this acceleration occurs, part of the surrounding continuous fluid has to be accelerated as well. The Virtual Mass Force is implemented in Fluent as follows [11]:

$$\mathbf{I}_{vm} = 0.5\alpha_p \rho_q \left(\frac{D\mathbf{u}_q}{Dt} - \frac{D\mathbf{u}_q}{Dt} \right) \tag{2.27}$$

where the $\frac{D}{Dt}$ operator denotes the material derivative. The acceleration of the secondary phase depends on the buoyancy force. Thus the significance of the virtual mass force will increase if the density ratio between the phases are high.

A comparison between the different drag models as a function of the bubble Reynolds number is shown in figure 2.1 for the system of air dispersed in water.

2.3.3. LIFT

The lift force acts on a particle due to velocity gradients in the flow field of the continuous phase. The velocity gradients will introduce a force that tend to push the particles in the direction perpendicular to the flow direction. The contribution of the lift force to the total interaction force is given by [11]:

$$\mathbf{I}_L = -C_L \rho_q \alpha_p (\mathbf{u}_p - \mathbf{u}_q) \times (\nabla \times \mathbf{u}_q) \tag{2.28}$$

C_L Denotes the lift force coefficient, which has to be calculated. For potential flow and spherical particles, a constant $C_L = 0.5$ can be used. If this assumption is not valid C_L has to be modeled.

2.3.4. WALL LUBRICATION

When bubbles rises in a vertical pipe it has been observed that the dispersed phase concentrates in a region close, but not precisely at the wall. This force is referred to as the wall lubrication force, and is implemented in Fluent as follows:

$$\mathbf{I}_{wl} = C_{wl} \rho_q \alpha_p |(\mathbf{u}_q - \mathbf{u}_p)_{\parallel}|^2 \mathbf{n} \tag{2.29}$$

Where $|(\mathbf{u}_q - \mathbf{u}_p)_{\parallel}|$ is the component relative velocity that is tangential to the wall, $\mathbf{n}$ is the unit normal pointing away from the wall and C_{wl} is the wall lubrication coefficient. The wall lubrication coefficient can be modelled by Frank's model[11]:

$$C_{wl} = C_w \max\left(0, \frac{1}{C_{wd} \times \frac{1 - \frac{y_w}{C_{wc} d_b}}{y_w \left(\frac{y_w}{C_{wc} d_b} \right)^2}} \right) \tag{2.30}$$

Where C_W is dependent on the Eotvos number, $C_{wd} = 6.8$ is a dampening coefficient which determines the magnitude of the force and $C_{wc} = 10$ is a cut-off coefficient and determines the distance to the wall within the force is active.

2.3.5. TURBULENT DISPERSION

To account for the dispersion of a secondary phase due to turbulent interaction, an additional force term can be included, known as the Turbulent Dispersion Force. It is modelled in the following way, by introducing an additional "drifting velocity", u_{dr}:

$$I_{td} = K_{pq} u_{\text{dr}} \tag{2.31}$$

SIMONIN

The drifting velocity can be modelled according to Simonin and Viollet [18]:

$$\frac{D_{t,pq}}{\sigma_{pq}} \left(\frac{\nabla \alpha_p}{\alpha_p} - \frac{\nabla \alpha_q}{\alpha_q} \right) \tag{2.32}$$

Where $D_{t,pq}$ is the turbulent dispersion tensor, given by equation 2.96. $\sigma_{pq} = 0.75$ is the Turbulent Prandtl number.

DIFFUSION IN VOF

Instead of modelling the drifting velocity, a diffusion term can be included in the volume fraction equation [11]:

$$\frac{\partial}{\partial t}(\alpha_q \rho_q) + \nabla \cdot (\alpha_q \rho_q u_q) = \nabla(\Gamma_q \nabla_q) \tag{2.33}$$

Where Γ_q is the diffusion coefficient for phase q.

2.4. TURBULENCE

2.4.1. INTRODUCTION

Above a certain Reynolds number, all practical flows become unstable and the flow field goes from an ordered to a chaotic state. This chaotic state of the flow is referred to as turbulence. The Reynolds number is defined in general as:

$$\text{Re} = \frac{U \rho L}{\mu} \tag{2.34}$$

Where U and L are the relevant velocity and length scales of the flow. The Reynolds number represents the ratio between inertial and viscous forces acting on the fluid. This can also be seen in equation 2.2, where the non-linear left hand side becomes dominant as the Reynolds number increases. In theory, equations 2.1 and 2.2 combined with the appropriate boundary conditions are enough to compute any kind of flow field. However to properly resolve a turbulent flow - field, the computational grid has to be fine enough to resolve all length scales. In a turbulent flow the smallest length scales are given by the Kolmogorov scale:

$$\eta = \left(\frac{\nu^3}{\epsilon} \right)^{1/4} \tag{2.35}$$

Using dimensional analysis, the following ratio between the macroscopic length scale, L and η can be obtained[6]:

$$\frac{\eta}{L} \approx \text{Re}^{-3/4} \tag{2.36}$$

The number of grid points in one coordinate direction would scale with:

$$N \cong \frac{L}{\eta} \tag{2.37}$$

Because of its chaotic nature, turbulent flow is inherently three dimensional, thus in reality the total number of grid cells would scale with N^3. Combining this with equations 2.36 and 2.37 gives:

$$N \cong \text{Re}^{9/4} \tag{2.38}$$

This shows that even for a moderately high Reynolds Number, the grid size would be way beyond the computational capacity of most computers. This is commonly referred to as a Direct Numerical Simulation. One way of addressing this problem is to only resolve the larger length scales, whilst modeling the smallest one. This is referred to as a Large Eddy Simulation. However a more common approach is to use time averaged equations, which will be explained below.

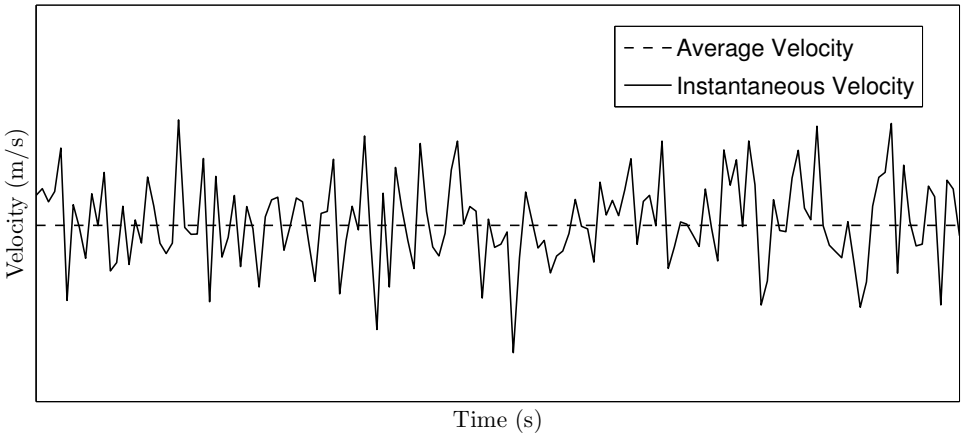

Figure 2.2: Example of a typical point measurement of velocity for turbulent flow

2.4.2. REYNOLDS AVERAGING

In most of the practical applications of CFD, the user has no need of the complete instantaneous flow field. Very often it is enough to know the time averaged flow field to compute the necessary. The computational requirements can be reduced significantly by solving time averaged equations instead of instantaneous. The process of time averaging starts with the idea that all instantaneous flow variables can be decomposed into a steady mean and a fluctuating part:

$$\phi(t) = \Phi + \phi'(t) \tag{2.39}$$

This is also known as Reynolds decomposition. An illustration of the difference between the averaged and instantaneous velocity can be seen in figure 2.2. The time average of a flow variable can be formally defined as:

$$\Phi = \frac{1}{\Delta t}\int_0^{\Delta t} \phi(t)\,\mathrm{d}t \tag{2.40}$$

Δt is the time averaging interval. For the time average to be meaningful, Δt has to be larger than the slowest time scale of the flow. By using equation 2.40 on various terms that appear in equations 2.6 and 2.7. For the general decomposed flow variables $\phi(t) = \Phi + \phi'(t)$ and $\psi(t) = \Psi + \psi'(t)$, it has been showed [6] that the following rules for time averaging can be constructed:

$$\overline{\phi'} = \overline{\psi'} = 0 \qquad \overline{\phi} = \Phi \qquad \overline{\frac{\partial \phi}{\partial s}} = \frac{\partial \Phi}{\partial s} \qquad \overline{\int \phi\,\mathrm{d}s} = \int \Phi\,\mathrm{d}s$$
$$\overline{\phi + \psi} = \Phi + \Psi \qquad \overline{\psi\phi} = \Psi\Phi + \overline{\psi'\phi'} \qquad \overline{\phi}\,\overline{\Psi} = \Phi\Psi \qquad \overline{\phi'\Psi} = 0 \tag{2.41}$$

The above rules can be applied on equations 2.6 and 2.7 to derive equations for time averaged velocities. These equations are commonly refereed to as Reynolds averaged equations. Note that from this point on, tensor notation will be used instead of vector notation to make the treatment of turbulence easier.

Reynolds Averaged Continuity Equation

$$\frac{\partial(\alpha_q \rho_q)}{\partial t} + \frac{\partial}{\partial x_i}(\alpha_q \rho_q U_{q,i}) = 0 \tag{2.42}$$

Reynolds Averaged Navier Stokes Equation

$$\frac{\partial}{\partial t}(\rho_q U_{q,i}) + \frac{\partial}{\partial x_j}(\rho U_{q,i} U_{q,j}) = -\frac{\partial p}{\partial x_i} + \frac{\partial \tau_{q,ij}}{\partial x_j} + \frac{\partial \tau_{\mathrm{Re},q,ij}}{\partial x_j} \tag{2.43}$$

Where $\tau_{q,ij}$ is the Reynolds averaged stress tensor for phase q:

$$\tau_{q,ij} = \mu\left(\frac{\partial U_{q,i}}{\partial x_j} + \frac{\partial U_{q,j}}{\partial x_i} + \frac{2}{3}\delta_{ij}\frac{U_{q,l}}{x_l}\right) \tag{2.44}$$

The new term i, $\tau_{\mathrm{Re},q,ij}$ is known as the Reynolds stress tensor:

$$\tau_{\mathrm{Re},q,ij} = -\rho\overline{u_i' u_j'} \tag{2.45}$$

The Reynolds stress tensor arises from the time averaging of the non linear convective term. According to the averaging rules in equations **??**, the time average of the product of two instantaneous variables is equal to the product of the time average plus the covariance of the fluctuations. This additional shear stress represents the effect of velocity fluctuations on the mean flow due to increased eddy formation. The addition of the Reynolds stress tensor to the Navier-Stokes equation means that the system of equations are no longer closed. To close the system of equations the Reynolds stress tensor has to be modeled. Different ways of modeling turbulence will be discussed in section 2.4.3.

2.4.3. TURBULENCE MODELING

BOSSINESQUE HYPOTHESIS

Bossinesq postulated in 1877 that the Reynolds Stresses could be proportional to the mean rates of deformation:

$$-\rho\overline{u_i' u_j'} = \mu_t\left(\frac{\partial U_{q,i}}{\partial x_j} + \frac{\partial U_{q,j}}{\partial x_i}\right) - \frac{2}{3}\rho k\delta_{ij} \tag{2.46}$$

Equation 2.46 is justified by experimental data that has shown that turbulent stresses increases when the mean rate of deformation increases. Also it has been found that turbulence decays if there is no shear [6]. The Bossinesque Hypothesis introduces the concept of eddy viscosity, μ_t in addition to the molecular viscosity. One important feature of equation 2.46 is that it implies isotropic turbulence. If the first term of equation 2.46 were to be evaluated for the normal stresses($i = 1,2,3,\ j = i$):

$$\tau_{Re,q,ii} = 2\mu_t\rho_q\left(\frac{\partial U_{q,1}}{\partial x_1} + \frac{\partial U_{q,2}}{\partial x_2} + \frac{\partial U_{q,3}}{x_3}\right)$$

If continuity is invoked it can clearly be seen that the normal stresses would equal to zero for an incompressible flow. This is not physical, thus the reason for introducing the second term to equation 2.46. Turbulent kinetic energy, k can be defined in a general way as the sum of the averaged normal Reynolds stresses:

$$k = \frac{1}{2}(\overline{u_1'^2} + \overline{u_2'^2} + \overline{u_3'^2}) \tag{2.47}$$

The Kronecker delta, δ_{ij} ensures that the second term is added only to the diagonal of the Reynolds stress tensor. This means that all the normal stresses are equal to the second term in equation 2.46, which in turn implies that the turbulence is isotropic.

STANDARD $k-\epsilon$ MODEL

The standard $k-\epsilon$ model was proposed by Launder and Spalding [19]. Through dimensional analysis it was suggested that the eddy viscosity could be expressed as a product of a turbulent velocity scale v_t and a turbulent length scale l_t:

$$\mu_t = C_{v_t l_t}\rho v_t l_t \tag{2.48}$$

l represents the largest scales of turbulence and can be defined in terms of turbulent kinetic energy k and the dissipation of turbulence ϵ:

$$l = C_l\frac{k^{3/2}}{\epsilon} \tag{2.49}$$

v_t can be expressed in terms of turbulent kinetic energy:

$$v^2 = k \tag{2.50}$$

Equations 2.49 and 2.50 can be inserted in 2.48, to express the eddy viscosity in terms of k and ϵ:

$$\mu_t = \rho C_{\mu_t}\frac{k^2}{\epsilon} \tag{2.51}$$

Where $C_{v_t l_t}$ and C_l has been lumped together in a new constant C_{μ_t}. To calculate k and ϵ, it is possible to construct model transport equations[19].

Table 2.3: Constants used in standard $k-\epsilon$ model.

C_μ	$C_{1,\epsilon}$	$C_{2,\epsilon}$	σ_k	σ_ϵ
0.09	1.44	1.92	1.0	1.3

Transport Equation for Turbulent Kinetic Energy

$$\frac{\partial}{\partial t}(\alpha_q\rho_q k_q)+\frac{\partial}{\partial x_i}(\alpha_q\rho_q k_q U_{q,i})=\frac{\partial}{\partial x_j}\left[\alpha_q\left(\mu_q+\frac{\mu_{q,t}}{\sigma_k}\right)\frac{\partial k_q}{\partial x_j}\right]+\alpha_q(G_{k,q}-\rho_q\epsilon_q)+\alpha_q\rho_q\Pi_{k,q} \tag{2.52}$$

Transport Equation for the Dissipation of Turbulence

$$\frac{\partial}{\partial t}(\alpha\rho_q\epsilon_q)\frac{\partial}{\partial x_i}(\alpha_q\rho_q\epsilon_q U_{q,i})+\frac{\partial}{\partial x_j}\left[\alpha_q\left(\mu_q+\frac{\mu_{t,q}}{\sigma_\epsilon}\right)\frac{\partial\epsilon_q}{\partial x_j}\right]+\alpha_q\frac{\epsilon_q}{k_q}(C_{1,\epsilon}G_{k,q}-C_{2\epsilon}\rho_q\epsilon_q)+\alpha_q\rho_q\Pi_{\epsilon,q} \tag{2.53}$$

Equations 2.52 and 2.53 has also been modified to include the effect of multiphase flow [11]. $G_{q,k}$ is a source term for the production of turbulent kinetic energy:

$$G_{q,k}=\mu_{q,t}S_q^2 \tag{2.54}$$

Where S is the modulus of the mean strain rate tensor:

$$S_q\equiv\sqrt{S_{q,ij}S_{q,ij}} \tag{2.55}$$

$\Pi_{q,k}$ and $\Pi_{q,\epsilon}$ are source terms that accounts for the effects of turbulent two-way coupling. The constants, C_μ, $C_{1,\epsilon}$, $C_{2,\epsilon}$ and the turbulent Prandtl numbers σ_k and σ_ϵ are given in table 2.3. The values of the constants has been recommended by Launder and Spalding [19] after extensive experiments on free turbulent flows. These values were shown to give satisfactory results for plane jets and mixing layers.

The standard $k-\epsilon$ model assumes that the flow is fully turbulent [19]. This assumption has its root in how ϵ is defined in equation 2.49. As stated above, l represent the length scales of the largest eddies. ϵ Represents the dissipation of turbulence which occurs at the smallest scales of motion. So the "small scale" variable ϵ is defined using the "large scale" variable l. Equation 2.49 is justified at high Reynolds numbers because when the flow is fully turbulent, the rate which energy is passed from larger to smaller eddies is matched by the rate which the largest eddies extracts energy from the mean flow [6].

The applicability of the standard $k-\epsilon$ to multiphase flows has also been disputed. The model was originally developed with single phase flow in mind, and the constants in table 2.3 were also calibrated from experiments on single phase flows. Sokolichin and Eigenberger [3] addressed this issue, when they applied the standard $k-\epsilon$ model to their model of a flat bubble column. The results were validated against experiments by Borchers *et al.* [20], and it was shown that the simulation agreed well with experimental data when the standard $k-\epsilon$ model was used.

$k-\epsilon$ RENORMALISATION GROUP

As stated in section 2.4.3.2, the standard $k-\epsilon$ model is only applicable to fully turbulent flows. Yakhot *et al.* [21] developed a alternative to the standard $k-\epsilon$ by using a statistical technique known as renormalization group (RNG). The main difference in the derivation of the RNG $k-\epsilon$ model is that instead of determining the model constants by experiments, they are explicitly calculated by the method itself.

RNG Transport Equation for Turbulent Kinetic Energy

$$\frac{\partial}{\partial t}(\alpha_q\rho_q k_q)+\frac{\partial}{\partial x_i}(\alpha_q\rho_q k_q U_{q,i})=\frac{\partial}{\partial x_j}\left[\alpha_q\left(\mu_q+\frac{\mu_{q,t}}{\sigma_k}\right)\frac{\partial k_q}{\partial x_j}\right]+\alpha_q(G_{k,q}-\rho_q\epsilon_q)+\alpha_q\rho_q\Pi_{k,q} \tag{2.56}$$

RNG Transport Equation for the Dissipation of Turbulence

$$\frac{\partial}{\partial t}(\alpha_q\rho_q\epsilon_q)+\frac{\partial}{\partial x_i}(\alpha_q\rho_q\epsilon_q U_{q,i})=\frac{\partial}{\partial x_j}\left[\alpha_q\left(\mu_q+\frac{\mu_{q,t}}{\sigma_\epsilon}\right)\frac{\partial\epsilon_q}{\partial x_j}\right]+\alpha_q(C_{1\epsilon_q}\frac{\epsilon_q}{k}P_k-C_{2\epsilon}^*\rho\frac{\epsilon^2}{k})+\alpha_q\rho_q\Pi_{\epsilon,q} \tag{2.57}$$

Table 2.4: Constants used in RNG $k-\epsilon$ model.

C_μ	$C_{1,\epsilon}$	$C_{2,\epsilon}$	σ_k	σ_ϵ	η_0
0.0845	1.42	1.68	0.7194	0.7194	4.38

Where $C^*_{2\epsilon}$ and η is defined as:

$$C^*_{2\epsilon} = C_{2\epsilon} + \frac{C_\mu \eta^3 (1-\eta/\eta_0)}{1+\beta\eta^3} \qquad \eta = Sk/\epsilon \tag{2.58}$$

The RNG $k-\epsilon$ model also includes a differential formulation of the eddy viscosity that is supposed to account for low Reynolds number effects:

$$\mathrm{d}\left(\frac{\rho_q^2 k_q}{\sqrt{\epsilon_q \mu_q}}\right) = 1.72 \frac{\hat{\nu}}{\sqrt{\hat{\nu}^3 - 1 C_\nu}} \mathrm{d}\hat{\nu} \tag{2.59}$$

Where $\hat{\nu}$ and C_ν is defined as:

$$\hat{\nu} = \frac{\mu_{eff}}{\mu_q} \qquad C_\nu \approx 100 \tag{2.60}$$

Equation 2.59 is integrated to obtain an expression for the eddy viscosity at low Reynolds number. In the high Reynolds number limit, equation 2.59 yields equation 2.48.

REALIZABLE $k-\epsilon$ MODEL

One issue with both the standard and RNG $k-\epsilon$ models, are that neither are realizable. A model is only realizable if the predicted normal stresses are positive and if the shear stresses satisfies the Cauchy-Schwartz inequality[11]. It has been known for long that the standard eddy viscosity formulation in equation 2.46 becomes non-realizable when the mean strain rate in the fluid becomes large. Shih *et al.* [22] proposed a modified eddy viscosity formulation where C_μ is variable. This ensure that C_μ is modified properly to ensure that the model is realizable.

$$C_\mu = \frac{1}{A_0 + A_S \frac{kU^*}{\epsilon}} \tag{2.61}$$

Where U^* is:

$$U^* = \sqrt{S_{ij}S_{ij} + \tilde{\Omega}_{ij}\tilde{\Omega}_{ij}} \tag{2.62}$$

The parameters $\tilde{\Omega}_{ij}$ and Ω_{ij} are defined as:

$$\tilde{\Omega}_{ij} = \Omega_{ij} - 2\epsilon_{ijk}\omega_k \tag{2.63}$$

$$\Omega_{ij} = \overline{\Omega_{ij}} - \epsilon_{ijk}\omega_k \tag{2.64}$$

$\overline{\Omega}$ is the mean rate of rotation tensor defined as:

$$\overline{\Omega}_{ij} = \frac{1}{2}\left(\frac{\partial U_i}{\partial x_j} - \frac{\partial U_j}{\partial x_i}\right) \tag{2.65}$$

The model constants A_0 and A_S are given by:

$$A_0 = 4.04 \tag{2.66}$$

$$A_S = \sqrt{6}\psi \tag{2.67}$$

Where ψ is:

$$\psi = \frac{1}{3}\cos^1(\sqrt{(6)}W) \tag{2.68}$$

$$W = \frac{S_{ij}S_{jk}S_{ki}}{S} \tag{2.69}$$

Where S_{ij} is the mean strain rate defined by equation **??** and S is its modulus defined by 2.55. Shih *et al.* [22] also proposed a modified transport equation for ϵ:

Realizable Transport Equation for the Dissipation of Turbulence

$$\frac{\partial}{\partial t}(\epsilon\alpha_q\rho_q)+\frac{\partial}{\partial x_j}(\alpha_q\rho_q\epsilon U_{q,j})=\frac{\partial}{\partial x_j}\left[\alpha_q\left(\mu+\frac{\mu_t}{\sigma_\epsilon}\right)\frac{\partial\epsilon}{\partial x_j}\right]+\alpha_q\rho_q C_1 S\epsilon-\alpha_q\rho_q C_2\frac{\epsilon^2}{k+\sqrt{\nu\epsilon}}+\alpha_q\rho_q\Pi_{\epsilon,q} \tag{2.70}$$

The turbulent kinetic energy, k is calculated by equation 2.52. Equation 2.70 is derived by first modeling a transport equation for the mean squared vorticity fluctuations, $\overline{\omega_i^2}$. At high Reynolds numbers, $\epsilon=\nu\overline{\omega_i^2}$ [22]. Substituting this relation into the transport equation for $\overline{\omega_i^2}$ yields equation 2.70. This also implies that the realizable $k-\epsilon$ model is only valid at higher Reynolds numbers. The Realizable $k-\epsilon$ model has shown to improve upon the standard $k-\epsilon$ in many benchmark cases [22]. It has also been noticed that the realizable $k-\epsilon$ model removes the abnormal spreading of planar and round jets that has been observed with the standard $k-\epsilon$ model.

REYNOLDS STRESS MODEL

The Reynolds Stress model was originally proposed by Launder *et al.* [23] for single-phase flow. It takes a different approach in modeling the Reynolds stresses. Instead of assuming that the Reynolds stress tensor is proportional to the mean rate of deformation, a transport equation for each component in the tensor is formulated. A Reynolds Stress Model for use together with the Eulerian-Eulerian multiphase model was proposed by Cokljat *et al.* [24]. The Transport equation for the components of the Reynolds stress tensor can be written in a compact form as:

Reynolds Stress Transport Equation

$$\frac{\partial}{\partial t}(\alpha\rho\overline{u_i'u_j'})+\underbrace{C_{ij}}_{\text{Convection}}=-\underbrace{D_{T,ij}}_{\substack{\text{Turbulent-}\\\text{Diffusion}}}+\underbrace{D_{L,ij}}_{\substack{\text{Molecular-}\\\text{Diffusion}}}-\underbrace{P_{ij}}_{\substack{\text{Stress-}\\\text{Production}}}+\underbrace{\phi_{ij}}_{\substack{\text{Pressure-}\\\text{strain}}}-\underbrace{\epsilon_{ij}}_{\text{Dissipation}}-\underbrace{F_{ij}}_{\substack{\text{Production By-}\\\text{System-}\\\text{Rotation}}}+\underbrace{\Pi_{q,ij}}_{\substack{\text{Turbulent-}\\\text{Two-way Coupling}}} \tag{2.71}$$

The individual terms in 2.71 are given by:

$$C_{ij}=\frac{\partial}{\partial x_k}(\alpha\rho U_k\overline{u_i'u_j'}) \qquad P_{ij}=\alpha\rho\left(\overline{u_i'u_k'}\frac{\partial U_j}{\partial x_k}+\overline{u_j'u_k'}\frac{\partial U_i}{\partial x_k}\right)$$

$$D_{L,ij}=\frac{\partial}{\partial x_k}\left(\alpha\mu\frac{\partial}{\partial x_k}\overline{u_i'u'j}\right) \qquad D_{T,ij}=\frac{\partial}{\partial x_k}[\alpha_q\rho_q\overline{u_i'u_j'u_k'}+\alpha p(\delta_{jk}u_i'+\delta_{ik}u_j')]$$

$$\phi_{ij}=\overline{\alpha p\left(\frac{\partial u_i'}{\partial x_j}+\frac{\partial u_i'}{\partial x_i}\right)} \qquad \epsilon_{ij}=2\alpha_q\rho_q\mu_q\overline{\frac{\partial u_i'}{\partial x_k}\frac{\partial u_j'}{\partial x_k}}$$

$$F_{ij}=2\alpha_q\rho_q\Omega_k(\overline{u_j'u_m'}\epsilon_{ikm}+\overline{u_i'u_m'}\epsilon_{jkm}) \qquad \Pi_{q,ij}=\frac{2}{3}\delta_{ij}\Pi_{kc}$$

Of the above terms, C_{ij}, $D_{L,ij}$, P_{ij} and F_{ij} can be calculated exactly. However $D_{T,ij}$, ϕ_{ij} and ϵ_{ij} has to be modeled. For $D_{T,ij}$ Daly and Harlow [25] proposed the following model based on gradient diffusion:

$$D_{T,ij}=C_s\frac{\partial}{\partial x_k}\left(\rho\frac{k\overline{u_k'u_l'}}{\epsilon}\overline{\frac{\partial u_i'u_j'}{\partial x_l}}\right) \tag{2.72}$$

Evaluating equation 2.72 may result in numerical instabilities [11], and a simplified version with a scalar turbulent diffusivity can be used instead:

$$D_{T,ij}=\frac{\partial}{\partial x_k}\frac{\mu_t}{\sigma_k}\overline{\frac{\partial u_i'u_j'}{\partial x_k}} \tag{2.73}$$

Where μ_t is computed using 2.48. ϕ_{ij} represents the correlation between pressure and velocity fluctuations. The pressure and strain interacts in a manner that reduces the anisotropic production of turbulence. The classic approach to model ϕ_{ij} is to decompose it in a "slow", "rapid" and a wall reflection term[23]:

$$\phi_{ij}=\phi_{r,ij}+\phi_{s,ij}+\phi_{w,ij} \tag{2.74}$$

Table 2.5: Constants used in quadratic pressure strain model.

C_1	C_1^*	C_2	C_3	C_3^*	C_4	C_5
3.4	1.8	4.2	0.8	1.3	1.25	0.4

The term $\phi_{s,ij}$ models the reduction in anisotropy due to the direct interaction between pressure and strain. This term may be modeled as:

$$\phi_{s,ij} = -1.8\rho_q\alpha_q\frac{\epsilon}{k}\left(\overline{u_i'u_j'} - \frac{2}{3}\delta_{ij}k\right) \tag{2.75}$$

Equation 2.75 suggest that $\phi_{s,ij}$ is proportional to the degree of isotropy. Consider the isotropic case when the normal stresses are equal to $\frac{2}{3}\delta_{ij}$. The expression inside the parentheses in equation 2.75 would then be equal to zero according to the reasoning in section 2.4.3.1. Which means that if the turbulence were already isotropic, $\phi_{s,ij}$ would equal to zero. The other term, $\phi_{r,ij}$ models the reduction in anisotropic turbulence due interactions between turbulent fluctuations and the mean flow. This may be modeled as:

$$\phi_{r,ij} = -0.60\left[(P_{ij} + F_{ij} - C_{ij}) - \frac{1}{3}\delta_{ij}(P_{kk} - C_{kk})\right] \tag{2.76}$$

A similar reasoning can be applied to equation 2.76 as for equation 2.75. But for equation $\phi_{r,ij}$ the reduction in anisotropy is proportional to the production processes that generates the anisotropy.

Alternatively, the pressure and strain interaction can be modelled using a quadratic relationflu [11]:

$$\begin{aligned}\phi_j = &-(C_1\rho_q\epsilon_q + C_1^*P)b_j + C_2\rho\epsilon(b_{ik}b_{kj} - \frac{1}{3}b_{mn}b_{mn}\delta_j) + (C_3 - C_3^*\sqrt{b_jb_j})\rho_q k_q S_J \\ &+ C_4\rho_q k_q(b_{ik}S_{jk} + S_{ik} - \frac{2}{3}b_{mn}S_{mn}\delta_j) + C_5\rho k_q(b_{ik}\Omega_{jk} + b_{jk}\Omega_{ik})\end{aligned} \tag{2.77}$$

Where b_j is the Reynolds stress anisotropy tensor:

$$b_j = \left(\frac{-\rho_q\overline{u_i'u_j'} + \frac{2}{3}\rho_q k_q\delta_j}{2\rho_q k_q}\right) \tag{2.78}$$

Ω_j is the mean rate of rotation tensor, defined by equation 2.65 and S_j is the mean strain rate tensor. The constants in equation 2.77 is given in table 2.5.

The ϵ_{ij} term represents the dissipation of turbulence. This term is modeled as:

$$\epsilon_{ij} = \frac{2}{3}\delta_{ij}\alpha_q\rho_q\epsilon \tag{2.79}$$

Where ϵ i calculated by a modified version of equation 2.53 [23]:

$$\frac{\partial}{\partial t}(\alpha_q\rho_q\epsilon) + \frac{\partial}{\partial x_i}(\alpha_q\rho_q\epsilon U_{q,i}) = \frac{\partial}{\partial x_j}\left[\alpha_q\left(\mu + \frac{\mu_t}{\sigma_\epsilon}\right)\frac{\partial\epsilon}{\partial x_j}\right] - \alpha_q C_{\epsilon,1}\frac{\epsilon}{2k}P_{ii} - C_{\epsilon,2}\alpha_q\rho_q\frac{\epsilon^2}{k} \tag{2.80}$$

The model constants $C_{1,\epsilon}$ and $C_{2,\epsilon}$ are given in table 2.3. The Prandtl number is set to $\sigma_\epsilon = 1.0$. The $\Pi_{q,ij}$ term is characteristic for multiphase flow and models the effect on the mean flow from turbulence in the dispersed phase.

The Reynolds stress model has shown to offer substantial improvement over the $k-\epsilon$ models for anisotropic flows, such as strong swirling flows, and flows with high streamline curvature [23, 24]. However the model suffers from some drawbacks. The Reynolds stress tensor contains nine components, which of six are linear independent. Together with equation 2.80, the Reynolds stress model requires solving seven additional partial differential equations. This of course will require additional computer resources compared to the $k-\epsilon$ models. The Reynolds stress model also suffers from the same problems with modeling the ϵ transport equation as the $k-\epsilon$ models.

NEAR WALL MODELING

The presence of a wall provides some additional challenges when a turbulence model is used. Even for fully turbulent flows, the area close to the wall a boundary layer is present where the flow is not fully turbulent. Thus it would be inappropriate to model the turbulence in the vicinity of a wall. Experiments has shown that the behavior of a fluid close to the wall is nearly universal [26]. This is commonly refereed to as "The Law of the Wall". The law of the wall is often expressed in the form of dimensional wall units, U^* and y^*, which represents the velocity and distance to the wall in wall units [11].

$$U^* = \frac{U_P C_\mu^{1/4} k_p^{1/2} y_p}{\tau_w / \rho} \tag{2.81}$$

$$y^* = \frac{\rho C_\mu^{1/4} k_P^{1/2} y_P}{\mu} \tag{2.82}$$

Where τ_w is the shear stress at the wall. The subscript P denotes the value of a quantity at the grid node closest to the wall.

Numerous experiments has shown that the outer portion of the boundary layer, known as the *Overlap layer* has a logarithmic velocity profile [26]. Launder and Spalding [19] proposed the following logarithmic wall function to relate U^* to y^*:

$$U^* = \frac{1}{\kappa} \ln[E y^*] \tag{2.83}$$

Where $\kappa = 0.4187$ is the von Karman constant, and $E = 9.793$ is an empirical constant. The part of the boundary layer that is located closest to the wall is known as the *viscous sub-layer*. Here the fluid is completely dominated by viscous shear stress, and no turbulent eddies are formed. Experiments has shown that in the viscous sub-layer, the following linear relation holds[26]:

$$U^* = y^* \tag{2.84}$$

Between the overlap layer and the viscous sub-layer, there is a region known as the *buffer layer*, where neither equation 2.83 or 2.84 is applicable.

It is important to note that the wall adjacent grid node, P has to be a inside the overlap region of the boundary layer to properly calculate the shear stress using equation 2.83. The general rule is that $y^* > 15$. The upper limit strongly depends on the Reynolds number, but for a moderate Reynolds number the upper limit is in the order of $y^* \sim 100$ [11].

TURBULENT TWO-WAY COUPLING

In general, the Reynolds stresses are only modelled by transport equations for the continuous phase. However, the turbulence in the continuous phase influences the dispersed phase and vice versa. This is commonly refereed to as two-way coupling. Several models exists to account for the turbulent two-way coupling.

SIMONIN ET AL.

Simonin and Viollet [18] proposed to model the effect of the dispersed phase turbulence on the continuous phase as source terms in the transport equations for the turbulent quantities:

$$\Pi_{k_q} = \sum_{p=1}^{M} \frac{K_{pq}}{\alpha_q \rho_q} X_{pq} (k_{pq} - 2k_q) + \sum_{p=1}^{M} \frac{K_{pq}}{\alpha_q \rho_q} X_{pq} (\overline{u_{pq}} \cdot \overline{u_{dr}}) \tag{2.85}$$

$$\Pi_{\epsilon_q} = 1.2 \frac{\epsilon_q}{k_q} \Pi_{k_q} \tag{2.86}$$

Where X_{pq} is defined as:

$$X_{pq} = \frac{\rho_p}{\rho_p + C_{vm} \rho_q} \tag{2.87}$$

The turbulent kinetic energy in the dispersed phase, k_p and its correlation between the phases k_{qp} are predicted by extending Tchen's theory on dispersion of discrete particles [11, 18]. Tchen's theory assumes that theses quantities are given in terms of characteristic time scales of the turbulence in the continuous phase. The first time scale is associated with inertial effects acting on the dispersed phase:

$$\tau_{pq}^F = \alpha_p \rho_p K_{pq}^{-1} \left(\frac{\rho_p}{\rho_q} + C_{vm} \right) \tag{2.88}$$

The second time scale is the eddy particle interaction time, mainly associated with the "crossing-trajectory effect"[11]. It is defined as:

$$\tau_{pq}^t \frac{\tau_q^t}{\sqrt{(1+C_\beta \xi_\tau^2)}} \tag{2.89}$$

τ_{pq}^t also depends on τ_q^t, which is the time scale associated with the energetic turbulent eddies in the continuous phase , which is defined as:

$$\tau_q^t = \frac{3}{2} C_\mu \frac{k_q}{\epsilon_q} \tag{2.90}$$

The parameters ξ_τ and C_β are defined as:

$$\xi_\tau = \frac{|U_p - U_q|}{\sqrt{\frac{2}{3}k_q}} \tag{2.91}$$

$$C_\beta = 1.8 - 1.35\cos^2\eta \tag{2.92}$$

Where γ is the angle between the mean particle velocity and the mean relative velocity. The ratio between the two characteristic times is written as:

$$\eta_{pq} = \frac{\tau_{pq}^t}{\tau_{pq}^F} \tag{2.93}$$

Simonin and Viollet [18] proposed that η_{pq} could be used to predict the turbulent quantities for the dispersed phase in the following way:

$$k_p = k_q \left(\frac{b^2 + \eta_{pq}}{1+\eta_{pq}} \right) \tag{2.94}$$

$$k_{pq} = 2k_q \left(\frac{b + \eta_{pq}}{1+\eta_{pq}} \right) \tag{2.95}$$

$$D_{pq}^t = \frac{1}{3} k_{pq} \tau_{pq}^t \tag{2.96}$$

$$b = (1 + c_{vm}) \left(\frac{\rho_p}{\rho_q} + 1 \right) \tag{2.97}$$

TROSHKO-HASSAN

An alternative way of modelling the source terms due to two-way coupling was proposed by Troshko and Hassan [27]:

$$\Pi_{k_q} = 0.75 \sum_{p=1}^{M} \frac{K_p q}{\alpha_q \rho_q} |U_p - U_q|^2 \tag{2.98}$$

$$\Pi_{\epsilon q} = 0.45 \frac{1}{\tau_p} \Pi_{k_q} \tag{2.99}$$

Where τ_p is the time scale of the induced turbulence, defined as:

$$\tau_p = \frac{2 C_{vm} d_p}{3 C_D |U_p - U_q|} | \tag{2.100}$$

SATO

Sato and Sekoguchi [28] proposed a different way of modelling the turbulent two-way coupling. Instead of adding source terms to the turbulence equations, a modified expression for the eddy viscosity of the continuous was used:

$$\nu_q = C_\mu \frac{k_q^2}{\epsilon_q} + 0.6 \cdot \alpha_p d_p |U_p - U_q| \tag{2.101}$$

2.5. NUMERICAL METHODS

The non linear nature of equation 2.2 makes it impossible to solve analytically. Therefore, numerical techniques are used to discretize the partial differential equations on a grid into algebraic equations, that can be solved on a computer using numerical linear algebra.

2.5.1. SPATIAL DISCRETIZATION

Consider the following one dimensional transport equation for the general scalar quantity φ:

$$\frac{\partial}{\partial x}(\rho u \varphi) = -\frac{\partial}{\partial x}\left(D\frac{\partial \varphi}{\partial x}\right) \tag{2.102}$$

Integrating equation 2.102 over the one dimensional control volume depicted in figure 2.3 yields the following equation:

$$J_e\varphi_e - J_w\varphi_w = D\left(\frac{\varphi_E - \varphi_P}{\delta x_e} - \frac{\varphi_P - \varphi_E W}{\delta_w}\right)A \tag{2.103}$$

Where D is the constant diffusion coefficient, J is the flux over the control volume boundary and A is the area of the control volume. An upper case letter subscript denotes a control volume node, and lower case denotes a control volume face.

This procedure is known as the Finite Volume Method (FVM), and is a very common way of discretizing partial differential equations in CFD software. The problem with the FVM formulation is that the value at the control volume face is unknown. This requires the fluxes to be reconstructed in the node values using some numerical scheme.

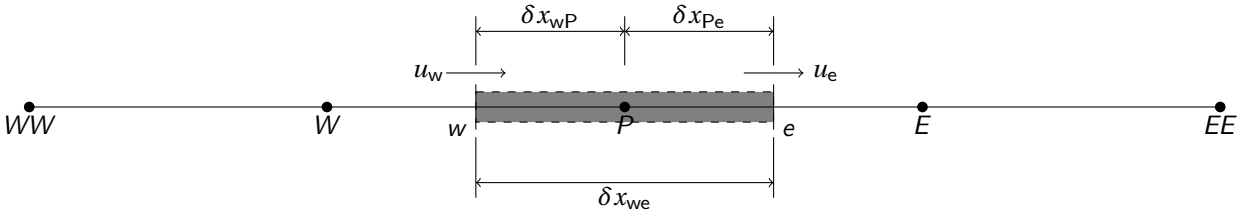

Figure 2.3: One dimensional control volume around node P

SECOND ORDER UPWIND

A second order upwind reconstructs the face value by linear interpolation in two adjacent upwind nodes. It is implemented in Ansys Fluent in the following way [11]:

$$\varphi_e = \varphi_P + \nabla\varphi_P \cdot \mathbf{r} \tag{2.104}$$

$$\varphi_w = \varphi_W + \nabla\varphi_W \cdot \mathbf{r} \tag{2.105}$$

Where $\mathbf{r}$ is the displacement vector. The gradient is evaluated by taking the arithmetic average of the values at the neighbouring cell centres. The second order upwind is second order accurate in space, which means that its truncation error decreases by a power of 2. It has acceptable accuracy, but can be susceptible to numerical diffusion.

QUADRATIC UPWIND INTERPOLATION (QUICK)

A QUICK scheme reconstructs the face value by quadratic interpolation in two upwind nodes and one downstream node. It is implemented in Fluent in the following way for a grid with constant volume control volume [11]:

$$\varphi_e = \chi\left[\frac{1}{2}\varphi_P + \frac{1}{2}\varphi_E\right] + (1-\chi)\left[\frac{3}{2}\varphi_P - \frac{1}{2}\varphi_W\right] \tag{2.106}$$

$$\varphi_w = \chi\left[\frac{1}{2}\varphi_W + \frac{1}{2}\varphi_P\right] + (1-\chi)\left[\frac{3}{2}\varphi_W - \frac{1}{2}\varphi_{WW}\right] \tag{2.107}$$

$$\tag{2.108}$$

Setting $\chi = 1/8$ yields the traditional QUICK scheme, but in Fluent it is implemented as a variable that is solution dependent to avoid introducing new solution extrema. The QUICK scheme is third order accurate, but it less stable than the second order upwind scheme.

GRADIENT LIMITER

Limiter are used to decrease the sensitivity of the solver to sudden changes, such as over and under shoots generally produces by the QUICK Scheme. In this study two types of gradient limiter will be considered. The standard and multidimensional. Both are based on a function. This function looks for the smallest gradient with the surrounding cells and then normalizes the values of the surrounding cells [11]. The difference between the standard and multidimensional limiter is that the standard limits all surrounding cells, even if it is not necessary. Whereas the multidimensional limiter only limits the cells where there is an extreme value.

2.5.2. TEMPORAL DISCRETIZATION

In addition to spatial discretization, the time derivative also has to be discretized. Consider the following one dimensional transient differential equation:

$$\frac{\partial \varphi}{\partial t} = F(\varphi) \tag{2.109}$$

Where $F(\varphi)$ is a general function of ϖ. If equation 2.109 is integrated over one time step Δt, it yields the following:

$$\frac{\varphi^{n+1} - \varphi^n}{\Delta t} = F(\varphi) \tag{2.110}$$

Where n signifies the current time level, $n+1$ signifies the future time level and $n-1$ signifies the previous time level. Evaluating $F(\varphi)$ at n is known as explicit time integration and evaluating it at $n+1$ is known as implicit time integration. Using implicit time integration has the advantage of being unconditionally stable, which makes it preferable over explicit integration. rearranging equation 2.110 with implicit time integration yields the following first order accurate time stepping formula:

$$\varphi^{n+1} = \varphi^n \Delta t F(\varphi^{n+1}) \tag{2.111}$$

Note here that the name implicit comes from the fact that φ is implicit in equation 2.111, and it has to be solved for every time step. Thus, the implicit method requires more computational resources than the implicit.

2.5.3. PRESSURE - VELOCITY COUPLING

A problem with solving a set of continuity and Navier-Stokes equations is that there is no explicit equation for pressure. To circumvent this, Patankar [29] proposed the SIMPLE algorithm, which uses a relationship between velocity and pressure known as the pressure correction equation to obtain the pressure field[11]. The governing equations are solved the equations by the following interative procedure:

1. Guess a pressure field
2. Solve the Navier-Stokes equation
3. Solve the pressure correction equation
4. Correct pressure and velocities
5. Solve all other transport equations
6. Check for Covergence

3

Case Studies

This chapter will present previous studies made on bubble columns. Both numerical and experimental studies will be presented.

3.1. Experimental Studies

3.1.1. The Becker Case

Becker *et al.* [5] made extensive research on the dynamics of a bubble column for the purpose of comparing it with CFD calculations. The Becker experiment utilized a flat bubble column with an aspect ratio of 1:3. The reasoning behind using a flat column was that it would eliminate the effect of the third dimension, basically making the flow two dimensional. The experimental data could then be compared to the two dimensional CFD model by Sokolichin and Eigenberger [30].

Experimental Setup

The experimental setup consisted of a flat bubble column that is depicted in figure 3.1. The column was filled with tap water, and air bubbles were injected through an asymmetrically located frit sparger. The liquid flow field was measured using Laser Doppler Anemometry (LDA). A long term measurement of the vertical liquid velocity was also performed in point **A**.

Results and Conclusions

Becker *et al.* [5] performed two experiments with a gas flow rate of $8\,\mathrm{l\,min^{-1}}$ and $1.6\,\mathrm{l\,min^{-1}}$ respectively. A photography and the measured liquid flow field from the experiment with high gas flow are shown in figure 3.2. It can be observed that the asymmetric placement of the frit sparger caused a gross circulation of the flow that pushes the bubble plume towards the wall. Three small vortices can be observed in three of the corners in figure 3.2b. The vortex in the upper left corner influences the flow by pushing the bubbles to the right, causing the vortex to move down towards the column as can be observed in figure 3.2a, causing the flow to reach a steady state[5].

When the gas flow rate was lowered to $1.6\,\mathrm{l\,min^{-1}}$, a rather remarkable change was observed. The previously observed stationary vortices became instationary at the lower gas flow rate. It was observed that the vortices changes size and moved down and dissipates close to the bottom. This caused the bubble plume to move in a meandering way, as can be observed in figure 3.3. Only the lower part of the plume remained stationary at all times. After a while, the plume reached a pseudo steady-state, where the plume oscillated in a periodic manner. The vertical liquid velocity was monitored at point **A**(Figure 3.1) for a long time, which is illustrated in figure 3.4. The oscillation period at point **A** was found to be approximately 41 seconds, with a mean velocity of approximately zero and an amplitude of about $0.2\,\mathrm{m\,s^{-1}}$ [5].

Other Studies

Sokolichin and Eigenberger [3] also presented results from the experiments by Becker *et al.* [5]. Interesting is that even though the same experiment is used, the results are somewhat different. If figures 3.4 and 3.5 are compared, the amplitude of the oscillations and the average velocity are different. Sokolichin and Eigenberger [3] presents no reason for the difference in the results, and it is possible that another data set that was not presented in the original article by Becker *et al.* [5] was used.

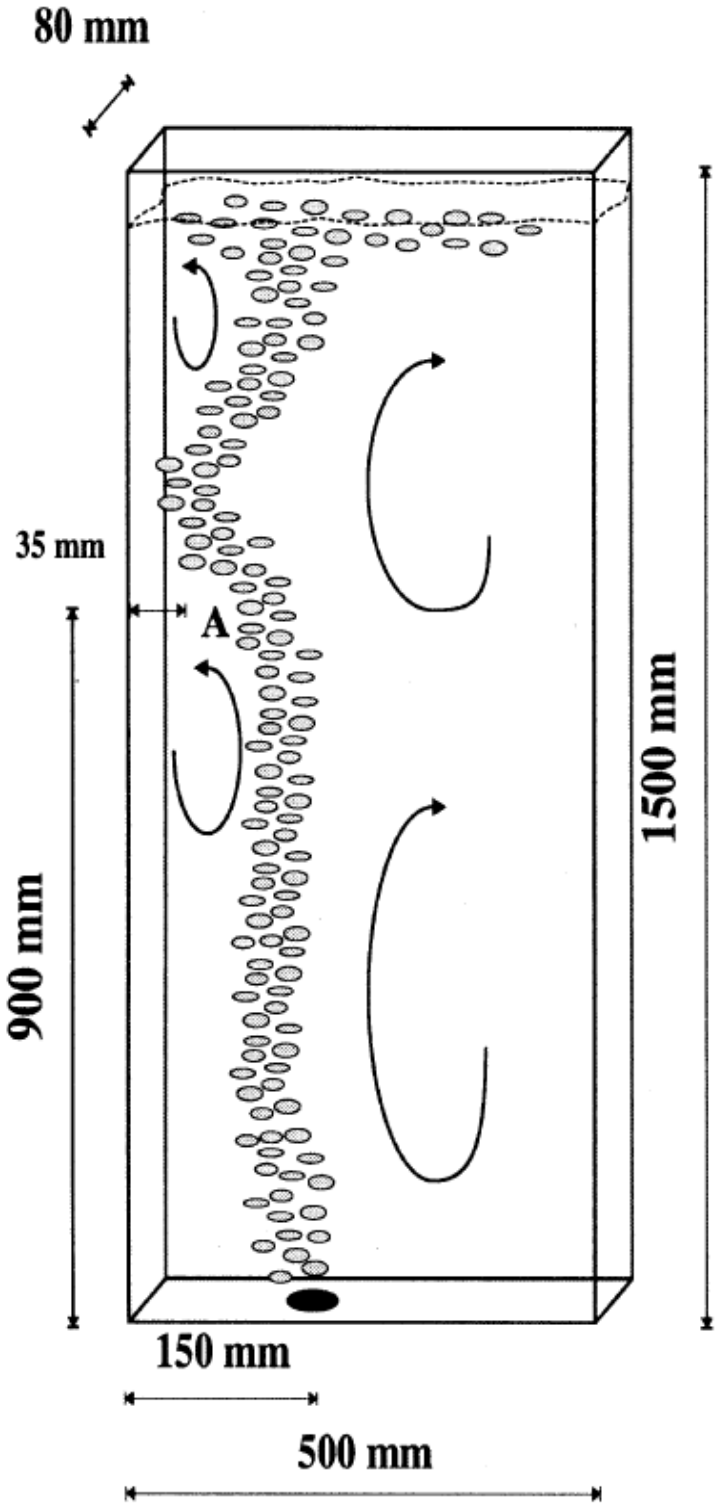

Figure 3.1: Schematic figure of the flat bubble column that was used in the experiments by Becker et al. Source: Oey *et al.* [31]

(a) Photography

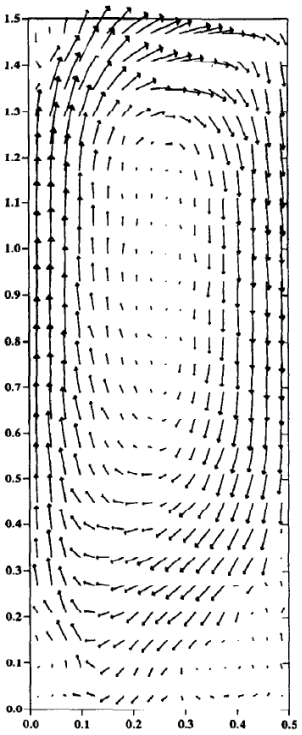

(b) LDA Measurements of the liquid flow field

Figure 3.2: Partially aerated bubble column at a high gas flow rate. Source: Becker *et al.* [5]

(a) Photography

(b) Photography

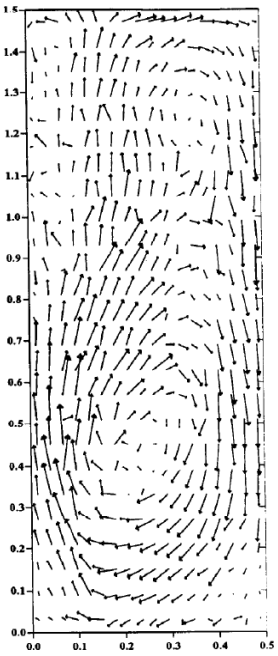

(c) LDA Measurment

Figure 3.3: Partially aerated bubble column at a low gas flow rate. Source: Becker *et al.* [5]

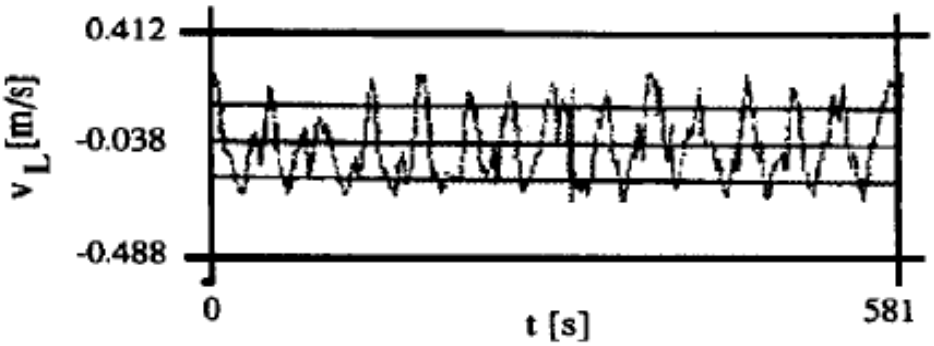

Figure 3.4: Local vertical liquid velocity measurement at point **A** (figure3.1). Source: Becker *et al.* [5]

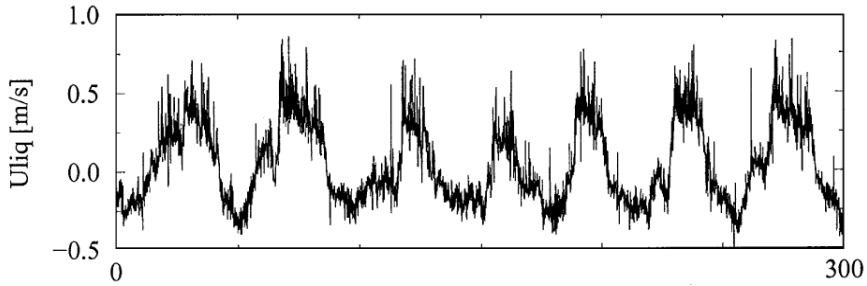

Figure 3.5: Local vertical liquid velocity measurement at point **A** (figure3.1). Source: Sokolichin and Eigenberger [3]

Borchers *et al.* [20] performed similar experiments on flat bubble columns.But rather than using the asymmetrical Becker column, they investigated an experimental setup consisting of a rectangular where the sparger is located in the middle. The experiments were performed on columns with three different aspect ratios, $H/D = 1$, $H/D = 2$ and $H/D = 3$. It was concluded that for a column with an aspect ratio of $H/D = 1$, the flow was essentially steady with only one vortex pushing the plume slightly towards the right wall. When the aspect ratio was increased, more vortices formed as shown in figure 3.6, and the plume started oscillate in the same fashion as in the experiments by Becker *et al.* [5].

case

3.1.2. THE DEEN CASE

The experimental study by Deen *et al.* [32] is another case that is frequently mentioned in literature as a benchmark for multiphase CFD calculations.

EXPERIMENTAL SETUP

The experiments were conducted in a rectangular column, but with a rectangular cross section. A schematic of the column with its dimensions is shown in figure 3.7. All experiments were carried out at a superficial gas velocity of 5.0 mm s^{-1}. The flow fields were measured by using both PIV and LDA techniques.

RESULTS AND CONCLUSIONS

In contrast to the experiments made by Becker *et al.* [5] where point measured time series of the vertical velocity was presented, Deen *et al.* [32] presents the measurements in the form of time averaged profiles of velocity and gas hold up. No information on the dynamics of the flow is presented.

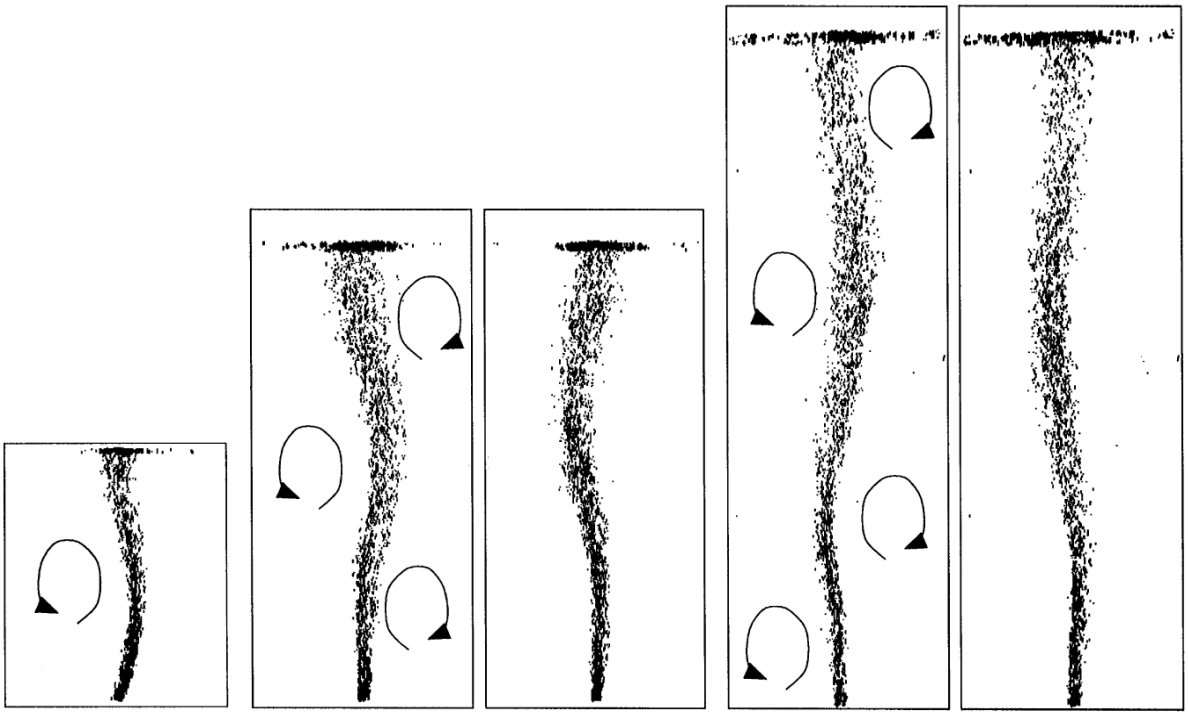

Figure 3.6: Photographs of three symmetrically aerated flat bubble columns width difference aspect ratio. From left to right: $H/D = 1$, $H/D = 2$, $H/D = 3$. Source: Borchers *et al.* [20]

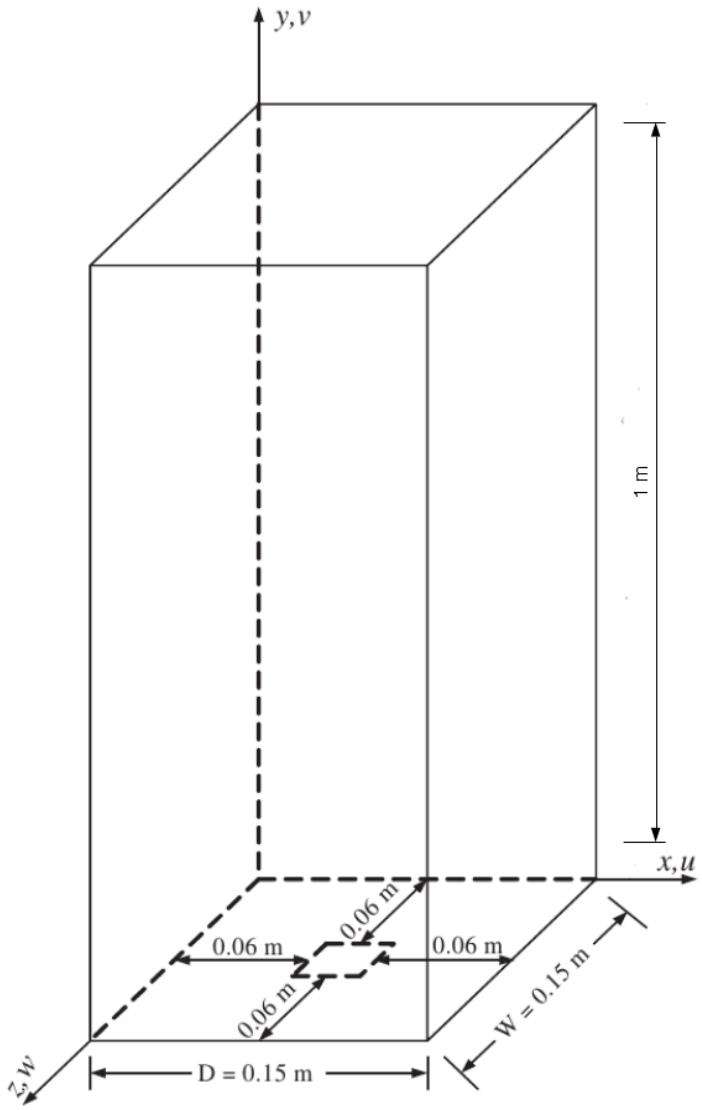

Figure 3.7: Schematic figure of the bubble column that was used in the experiments by Deen *et al.* [32]. Source: Zhang & Deen et al. [33]

3.2. NUMERICAL STUDIES

Several numerical studies based on the cases by Becker *et al.* [5] and Deen *et al.* [32] can be found in the literature.

3.2.1. RESULTS WITH LAMINAR MODELS

Sokolichin and Eigenberger [30] presented a two dimensional Eulerian-Eulerian model that was validated against the experimental data from Becker *et al.* [5]. Simulations were made on two spatial grids with a resolution of 18×25 and 36×50 grid cells. It was observed that the coarser grid gave a stationary result whereas the finer grid managed to capture the transient features, and led to the experimentally observed periodic wandering motion of the plume. No turbulence model was used. Instead a laminar model with an artificially increased viscosity was utilized [5]. The rationale behind this choice was that at the time, it was not clear if a single phase turbulence model could be extended to multiphase flow. Other studies had shown that the standard $k-\epsilon$ model would severely over estimate the eddy viscosity, which would completely dampen the transient character of the flow.

Sokolichin *et al.* [34] investigated the effect of choosing a Lagrangian over Eulerian description of the dispersed phase. For the Eulerian-Eulerian model a single momentum equation was used to model the gas-liquid mixture. The gas phase velocity was instead computed using a simple algebraic relation for the slip velocity. The conservation of mass was enforced by formulating a continuity equation for each phase. No turbulence model was used, and the turbulent viscosity was assumed to be equal to that of water. To account for the experimentally observed dispersion of the bubble plume due to turbulent fluctuations, a diffusion like term was included in the continuity equation of the gas phase. The effect of the spatial discretization scheme was also investigated, and the first order UPWIND scheme was compared with a Total Variation Diminishing (TVD) scheme. The simulations were performed on a computational grid consisting of 50×150 grid points. It was concluded that the Eulerian-Lagrangian approach gave equal results to the Eulerian-Eulerian approach within an acceptable accuracy. Both methods managed to reproduce the experimentally observed oscillating motion. It was also concluded that a first order UPWIND scheme gave rise to unacceptable levels of numerical diffusion, and that a TVD scheme should be used.

Loncle [4] performed two dimensional simulations on an asymmetrically aerated bubble column using the commercial CFD package Fluent 4.5. The simulations were made in similar fashion to those of Becker *et al.* [5] by artificially increasing the molecular viscosity of water by a factor of 100. A finite volume grid of 70×90 grid points was used with a time step of 5 ms. The effect of interfacial closure models were also investigated. An oscillating behavior of the predicted flow field was observed, but which a much higher frequency than had been observed experimentally. Furthermore, the inclusion of virtual mass and lift in addition to the drag force did not cause any significant difference in the results.

From the literature it can be concluded that a two dimensional model with an artificially increased viscosity can reproduce the unsteady movement of the bubble plume if the grid is sufficiently fine. Including a turbulence model with a two dimensional model severely over predicts the effective viscosity, and the transient features are damped out.

3.2.2. RESULTS WITH TURBULENCE MODELS

Previously, only two dimensional models had been considered. Simulations had shown that adding a turbulence model to such a model would severely over predict the turbulent viscosity [5, 30, 34]. As stated in the previous section, artificially increasing the molecular viscosity did yield an oscillating plume. But such an approach is based on trial and error, and it would be proper to instead try and find a deterministic approach to model the turbulence. A two dimensional model completely neglects the influence of the nearby walls, which has a dampening effect due to the no slip condition. Sokolichin and Eigenberger [3] evaluated the effect of including a turbulence model with an algebraic slip model in a three dimensional domain. The results from the three-dimensional computation was compared with the two-dimensional. A standard $k-\epsilon$ model was used to model the effect of turbulence. It was shown that the previously experienced difficulties with using a turbulence model was not present when using a three-dimensional model. The predicted flow field showed the transient behavior that had been experimentally observed by Becker *et al.* [5], and the results showed a surprisingly good qualitative agreement considering that the algebraic slip model was used instead

of including the momentum balance for the gas phase. The importance of using a TVD scheme for discretizing the momentum equation was highlighted. However no excessive numerical diffusion was observed if the k and ϵ equation were discretized with a first order UPWIND scheme.

Mudde and Simonin [35] performed two and three dimensional simulations using a Eulerian-Eulerian approach with a turbulence model. In addition to the drag and virtual mass forces, a turbulent dispersion term was introduced in the interaction force term. This term adds the contribution of a drifting velocity that takes into account the dispersion of bubbles due to turbulent two way coupling. The two dimensional simulations were made on two grids with a resolution of 27×52 and 38×52 grid points respectively. The two dimensional simulation showed a transient start up period of about 30 s, after which the oscillations was damped out. A ratio between turbulent and kinematic viscosity in the order of 1×10^3 - 1×10^4 for water was observed. Thus also showing that using a turbulence model in a two dimensional simulation severely over predicts the turbulent viscosity. Three dimensional simulations were also performed on two grids with a resolution of $27 \times 10 \times 52$ and $38 \times 18 \times 52$ grid points respectively. The effect of adding the virtual mass force was also investigated. The simulations which only included the drag force yielded an oscillation period of 4.44 s and an amplitude of $0.063\,\mathrm{m\,s^{-1}}$. This is much smaller than was observed in the experiments by Becker *et al.* [5]. These results were observed both on the fine and coarse grid. The addition of the virtual mass force showed a rather drastic change in the results. An oscillation period of 34 s and an amplitude of $0.2\,\mathrm{m\,s^{-1}}$ were now observed by Mudde and Simonin [35]. These results highlight the importance of including the virtual mass effect. However, the virtual mass effect is usually not expected to have a significant impact since it is only active when the air is accelerated relative to the water. This only occurs in the very lower portion of the column, before the bubbles reach a terminal velocity.

Loncle [4] investigate the effect of spatial and temporal discretization, turbulence and interaction force term with a three-dimensional Eulerian-Eulerian model. The domain was discretized on a grid consisting of $35 \times 45 \times 8$ grid points. The standard $k-\epsilon$ model was compared to the RNG $k-\epsilon$ model. Both the drag- and virtual mass force was taken into account. It was shown that both models predicted an oscillating flow field. However whilst the standard $k-\epsilon$ model predicted periodic oscillations, the RNG $k-\epsilon$ predicted a much more chaotic flow field, though with a similar character. The standard $k-\epsilon$ model predicted a higher turbulent kinetic energy than the RNG $k-\epsilon$ model, which led to a more qualitatively accurate dispersion of the bubble plume. Refining the grid led to a smaller amplitude and oscillation period, and no grid independence was reached. Simulations were also made that included the addition of a lift force to the interaction force term. It was shown that the inclusion of a lift force increased the dispersion of the bubbles at the top of the column. However, it was also observed that the plume was pushed against the back and front wall. This caused the gas fraction to be higher near the wall than the center, which has not been observed experimentally. It was concluded that the standard $k-\epsilon$ model consistently predicted results that were more similar to the experiments made by Becker *et al.* [5].

Oey *et al.* [31] investigate the sensitivity of interfacial closure model for an Eulerian-Eulerian model with respect to numerical diffusion. A set of different approaches to modeling the drag, virtual mass, turbulent dispersion and turbulent two-way coupling were tested. Two different approaches to model the drag force were tried. One which depended on the slip velocity, and another which also included a drift velocity which accounts for the dispersion effects due to the transport by turbulent motion. The simulations concluded that both drag models produced very similar results that also agreed fairly well with experimental data. It should however be noted that the model was not tested with different correlations for the drag coefficient. It was also concluded that the drag force alone was sufficient to capture the dynamics of the oscillating bubble plume, and that the other interaction forces had more of a "tuning effect". The effect of choosing a different gradient limiter was also considered. It was shown that choosing a more diffusive limiter caused smaller errors within the same order of magnitude as was caused by choosing a model for the "tuning" interaction forces. Using a first order UPWIND scheme without any gradient limiter caused excessive numerical diffusion which "smoothed out" the flow field, and the plume no longer showed any dynamic behavior.

In more recent literature, there has been an effort to systematically analyze the effect of many different models for the drag and lift coefficients. Also there has also been some efforts to implement population balances to account for the coalescence and break-up of bubbles. Gupta and Roy [36] studied the effect of using different drag velocity profile that had been experimentally obtained in a symmetrically aerated flat bub-

ble column. Four different drag coefficient models were evaluated. Those included the models by Schiller-Naumann, Ishii-Zuber, Tomiyama and Zhang-Vanderheyden. All models predicted a similar liquid velocity profile, where the velocity was somewhat over-predicted at the center of the column. The inclusion of a population balance had little to no effect at a superficial gas velocity of 1.33 mm/s. By including the lift force with a constant lift coefficient, the velocity profile was no longer over-predicted at the center of the column, and agreed very good with experimental data. The same behavior was observed when the superficial gas velocity was increased to 2.38 mm/s. The model was also tested in a square bubble column with a superficial gas velocity of 4.9 mm/s, and validated against the experiments by Deen *et al.* [32]. This resulted in a severe over-prediction of the vertical velocity profile if no lift force were included. The inclusion of a population balance had a slightly higher effect with a gas velocity of 4.9 mm/s. It was concluded that the lift force is of great importance to capture a correct velocity profile. There is however no data that is presented to draw any conclusions about the "pushing" phenomena caused by the lift force that was observed by Loncle [4]. It was also concluded that implementing a population balance had little to none effect. It is speculated that this is due to the moderate superficial gas velocity, and that a proper bubble size estimation is enough.

Masood and Delgado [13] performed a similar analysis to that of Gupta and Roy [36], but also included the turbulent dispersion and wall lubrication forces. The simulations were validated against the experiments by Deen *et al.* [32]. Similar conclusions to those of Gupta and Roy [36] were made, that the inclusion of a lift force was necessary for accurately predicting the vertical velocity profile. The inclusion of a wall lubrication term resulted in an over-estimation of the velocity profile. However, it was discussed that this might be due to a improper choice of wall lubrication model. Three different turbulence models were evaluated. The $k-\epsilon$ RNG, $k-\epsilon$ RNG Bubble induced turbulence (BIT) and the Explicit Algebraic Reynolds Stress Model (EARSM). EARSM was shown to better predict the turbulent kinetic energy profile, whilst the $k-\epsilon$ RNG and RNG BIT was shown to better predict the velocity field[13]. The results are all presented in the form of time averaged axial profiles, and no information on the dynamic behavior of the plume are mentioned.,

3.2.3. RESULTS WITH LARGE EDDY SIMULATIONS

Deen *et al.* [37] used a Large Eddy Simulation (LES) approach with an Eulerian-Eulerian model that was validated against the experimental data also provided by Deen *et al.* [32]. A large eddy simulation is different from RANS in the way that the larger eddies are resolved, and the smaller ones are filtered out and their influence on the flow is modelled using a sub-grid model. The domain was modelled according to the setup in figure 3.7, and consisted of $15 \times 100 \times 15$ grid nodes, which could be considered to be a rather coarse grid for a large eddy simulation. A filtered momentum equation was only used to model the continuous phase, whilst a laminar momentum equation with bubble induced turbulence (BIT) was used for modelling the dispersed phase. To account for the sub-grid turbulence in the continuous phase, the Smagorinsky sub-grid scale model was used. It was concluded that the LES approach gave a more accurate prediction of the time averaged flow fields compared to a RANS approach. It was also concluded that unless the lift force was included, the flow field at the centre of the column was over predicted. It should be noted that Masood and Delgado [13] did RANS simulations with a finer grid than Deen *et al.* [37], and their results did agree very well with the same experimental data. The question here is if the RANS simulations give the same results as a LES, then is grid fine enough do actually resolve all the large eddies?

Bombardelli *et al.* [38] compared a LES with a RANS approach on a geometry corresponding to the experiments made by Becker *et al.* [5]. A finite element discretization was used with an algebraic slip model. A grid of $50 \times 150 \times 8$ was used for the RANS simulations, and a grid of $300 \times 100 \times 16$ was used for the LES simulations. For the RANS approach a standard $k-\epsilon$ model was used, whilst for the LES approach the Smagorinsky sub grid model was used. It was concluded that with a RANS approach, the dynamic features of the bubble plume was dampened out, whilst with the LES the dynamic features were captured. The period time for the vertical liquid velocity was never considered. Instead the period time of the turbulent kinetic energy was presented. A constant period time for the oscillations of the turbulent kinetic energy was never found. Instead, a period of 50- and 80 seconds was reported. The dependence of initial conditions was also studied. It was concluded that after 80 seconds, the solution was practically independent of the initial conditions.

Zhang *et al.* [33] did a LES on a identical system to the one of Deen *et al.* [37] with an identical grid consisting of

$15 \times 90 \times 15$ grid nodes. However a more in depth sensitivity study regarding turbulence and interfacial closure was performed. Simulations were performed on two different geometries, with an aspect ratio of $H/D = 3$, and $H/D = 6$. A sensitivity analysis of the model constant in the Smagorinsky sub grid model was performed. It was found that a value of 0.08 predicted results that agreed very well with experimental data, whilst higher values up to 0.20 predicted results that differed significantly from experimental data. A comparison of two different sets of interfacial closure models were also made. The first set consisted of a drag coefficient model by Ishii-Zuber and constant coefficients for lift and virtual mass. The second set comprised of algebraic closure models for drag, lift and virtual mass coefficient proposed by Tomiyama [39]. It was found that the first set of interfacial closure models predicted a flat velocity profile that did not coincide with experimental data. The second set of interfacial models produced velocity profiles with a shape that were qualitatively similar to experimental data, but the velocity was under predicted. The influence of changing just the lift force coefficient was also investigated. It was shown that using a constant lift coefficient of $C_L = 0.5$ predicted velocity profiles that fitted better to experimental data than the lift coefficient calculated by the model of Tomiyama [39]. The LES results were also compared with results from simulations with a standard $k-\epsilon$ model. The same grid was used as with the LES simulations. To model the bubble induced turbulence, extra source terms were included in the transport equations for k and ϵ. It was concluded that the $k-\epsilon$ model predicted the same dynamic behaviour of the bubble plume as an LES simulation with the Smagorinsky sub grid model.

Niceno *et al.* [40] also performed Large Eddy Simulations on a square bubble column, corresponding to the experiments by Deen *et al.* [32]. A grid consisting of $30 \times 100 \times 30$ cells were used. All simulations included a drag, virtual mass and lift force. The importance of having a grid cell size larger than the bubble diameter was also highlighted. It is argued that if the bubble diameter is larger than the grid cell, they would induce "large scale motions which are not properly accounted for in a Eulerian-Eulerian LES, since there is no information on the interface details or their influence or their influence on the large-scale motions"[40]. A condition for an optimal grid is presented. This condition was developed by Milelli [41]. It states that the cell size must be at least 50 % larger than the bubble diameter for an accurate LES. It was concluded that the time averaged gas velocity profiles agreed very well with experimental data, whilst the time averaged liquid velocity profiles were somewhat under predicted.

Recently Dhotre *et al.* [42] published a review of the progress that has been made in Large Eddy Simulations for dispersed bubbly flow in the last ten years. Most of the presented cases use a Eulerian-Eulerian modelling approach and are based on the experimental setup by Deen *et al.* [32]. Some more recent studies based on a Eulerian-Lagrangian modelling approach were also presented, which shows great promise due to recent advances in computational power. One interesting study by Sungkorn *et al.* [43], where the Lattice-Boltzmann method was used to model the liquid phase. It was reported that using a Lattice-Boltzmann model led to a significant reduction of computational time, and a very efficient parallelization. Some key points were highlighted for further work. Firstly, it is pointed out that without any interface tracking method, the grid cell size has to be smaller than the bubble size. Secondly, the lift force is the main contribution to the dispersion of the bubble plume. Thirdly, the Eulerian-Lagrangian approach is getting more feasible as computers grow more powerful, and can provide an interesting approach for the future. Furthermore, it is highlighted that the effect of the interfacial forces in conjunction with the Smagorinsky sub-grid model needs to be further investigated.

From the existing literature it can be concluded that using a LES approach for simulating bubbly flow gives reasonable results when compared to experimental data. As stated above, it is often pointed out that for an accurate LES simulation, the grid size has to be larger than the bubble size. However, the justification for that statement is often somewhat vague, and usually no clear reason is given. This also conflicts with the mesh requirements for an LES, which usually has to be very fine to resolve all the large scales of motion. The question is if the grid spacing of 1 cm that was used in the studies by Deen *et al.* [37] and Zhang *et al.* [33] actually could be considered a "true" LES? Also, is there an actual advantage of performing a LES over a RANS simulation with such a coarse mesh? Furthermore, the simulations are always validated against the time averaged data provided by Deen *et al.* [37], and dynamical time series such as in the experiments by Becker *et al.* [5] are never considered. This procedure might average out some dynamical features of the flow, and transient data should also be used as validation.

4

Computational Setup

4.1. Introduction

All simulations in this study have been carried out using the commercial CFD code Fluent 15 from ANSYS using a Eulerian-Eulerian approach to model multiphase flow. All computations were made on the `hpc11` computer cluster, available at the Chemical Engineering department of Delft University of Technology.

4.2. Case Setup

4.2.1. Physical Properties

For the simulations, physical properties such as density, viscosity, bubble diameter and surface tension had to be specified for both phases. In this study, the same values as those of Loncle [4] were used for all physical properties. All physical properties are shown in table 4.1.

4.2.2. Computational Grid

A computational grid of $57 \times 100 \times 4$ was generated. A picture of the mesh is shown in figure 4.1. The mesh coordinate system is oriented in the following way: Length × Height × Depth, in the $x \times y \times z$ direction. To model the circular shape of the inlet, it was necessary to make the mesh slightly coarser in the x direction. Close up pictures of the top and bottom of the domain are shown in figures 4.2 and 4.3 respectively.

4.2.3. Boundary Condition

Wall

At the column walls, a no-slip boundary condition was imposed. The no-slip condition forces all fluids to have zero velocity at a wall. The shear-stress at the wall is calculated using the wall function that was described in section **??**. For the turbulent quantities, only the transport equation for k is solved in the wall adjacent cell with the following boundary condition at the column walls:

$$\frac{\partial k}{\partial n} = 0 \tag{4.1}$$

Where n is the local coordinate normal to the wall. It is assumed that a local equilibrium exists near the wall, where the production and dissipation rate of turbulence are equal [11]. The production term of k in equation 2.52 can then be approximated based on the logarithmic law of the wall:

$$G_k \approx \tau_w \frac{\tau_w}{\kappa \rho_q C_\mu^{1/4} k^{1/2} y_P} \tag{4.2}$$

Table 4.1: Physical Properties used in the simulations.

Phase	Substance	Density ρ (kg m^{-3})	Dynamic Viscosity μ (Pa s)	Bubble Diameter d_p (m)	Surface Tension σ (N m^{-1})
Liquid	Tap water	1×10^3	1×10^{-3}		7.28×10^{-2}
Gas	Air	1.2	1.72×10^{-5}	4×10^{-3}	

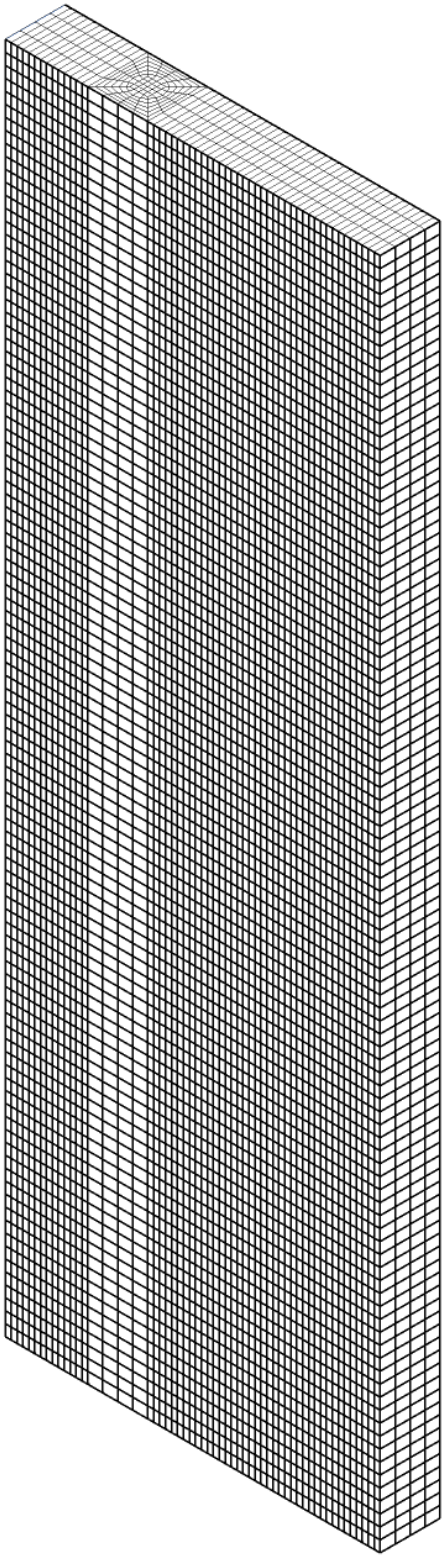

Figure 4.1: The computational grid used in this study

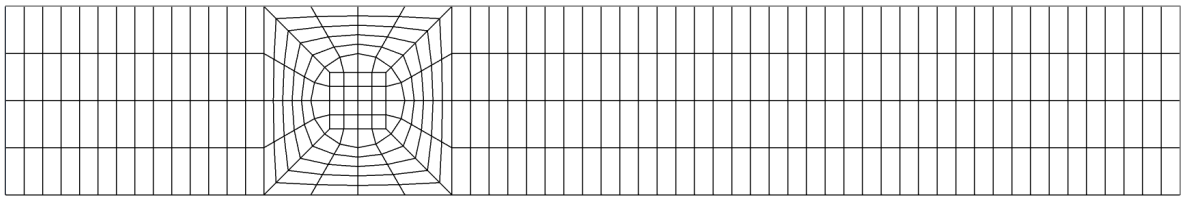

Figure 4.2: Close up picture of the top of the domain.

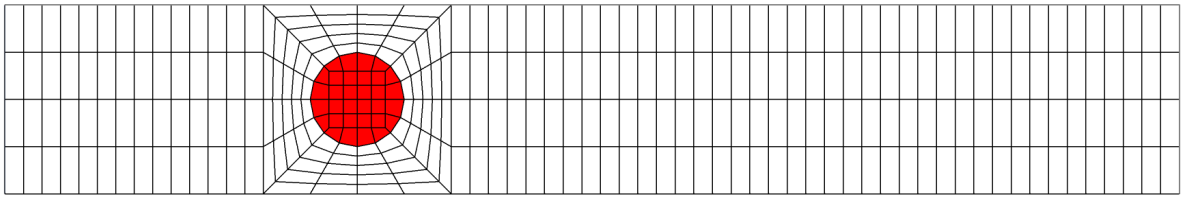

Figure 4.3: Close up picture of the bottom of the domain. The inlet cells are marked in red.

and ϵ is computed from:

$$\epsilon_P = \frac{C_\mu^{3/4} k_P^{3/2}}{\kappa y_P} \tag{4.3}$$

INLET

At the inlet, a fixed velocity boundary condition was applied for both phases. For the liquid phase a velocity of $0\,\mathrm{m\,s^{-1}}$ was imposed. The gas phase was specified with an assumed slip velocity of $U_{\text{slip}} = 0.20\,\mathrm{m\,s^{-1}}$. The gas fraction at the inlet also has to be specified. This was done in the same fashion as Mudde and Simonin [35]:

$$\alpha_2 = \frac{F}{A_s U_{\text{slip}}} = 10.6\%$$

Where the F is the gas flow rate of $1.6\,\mathrm{L\,min^{-1}}$ corresponding to the experiments of Becker *et al.* [5], and A_s is the surface area of the grid cells corresponding to the inlet. Instead of specifying k and ϵ at the inlet, the turbulent intensity, I_t and hydraulic diameter,D_H was set. For lack of a better estimate, the default value for I_t in Fluent of 5% was retained. The hydraulic diameter of the bubble column was calculated as for a rectangular duct as:

$$D_H = \frac{4 \times 0.5 \times 0.08}{2(0.5 + 0.08)} = 4.64 \times 10^{-2}\,\mathrm{m}$$

It should be noted that the turbulent boundary conditions will only influence the final solution via the diffusion terms in the transport equations for k and ϵ, since the convective terms at the inlet are zero because the liquid velocity at the inlet is set to zero [35].

OUTLET

The outlet boudary condition can be imposed in three different ways:

- **Option 1** The first alternative would be to extend the domain to include the freeboard region of air on top of the liquid water. An outflow condition could then be imposed at the top of the column. However this is generally not done for a number of reasons. Firstly, this would require a larger domain with a higher number of grid cells, leading to higher computation times. Secondly, in the freeboard region the air is no longer dispersed in the water. The turbulence modelling of the gas phase described in section 2.4.3.7 requires the gas fraction to be low. Thus, if the freeboard surface were to be included, another set of transport equations for k and ϵ would have to be solved.

- **Option 2** The second alternative would be to impose a constant pressure boundary condition. This is a physically realistic situation at a free surface. However, a fixed pressure boundary would not keep the liquid phase from exiting the domain. When this approach was used (figure 4.4), convergence problems with the continuity equation would appear. This due to the fact that water keeps exiting the domain, but not entering. For an incompressible flow, water would have to be created inside the domain to ensure mass conservation.

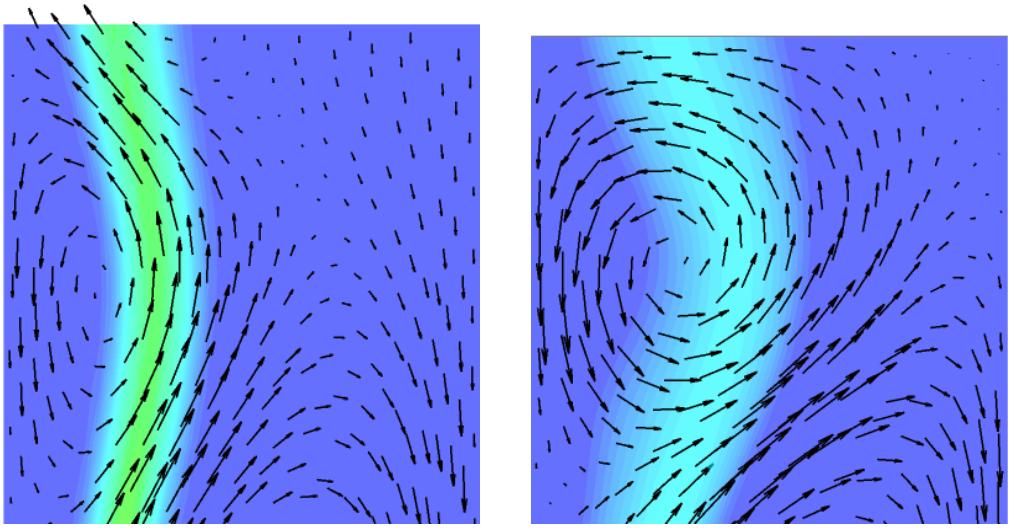

(a) Boundary Condition 2 (b) Boundary Condition 3

Figure 4.4: Snapshots of the volume fraction field at different times with the Reynolds stress model using a quadratic relation between pressure and strain.

- **Option 3** The third option would be to impose a degassing boundary condition. Such a boundary condition models the outlet as a free surface for the liquid phase, and as an outflow for the gas phase. Thus preventing only the liquid phase from exiting the domain. The gas is removed form the domain by a mass sink that is calculated using the mass flux normal to the boundary at the cells adjacent to the outlet. This type of boundary condition was used at the domain outlet in this study. This type of boundary condition was introduced in Ansys Fluent 14.5, and before it was only possible to use a degassing boundary condition if it was implemented as a used defined function

The difference between option 2 and 3 is illustrated in figure 4.4. Both pictures are taken at the same time instance. Here it can be seen that the presence of a free surface in option 3 has a influence on the fortmation of the vortex in the top left corner. The degassing boundary condition in option three predicts a bigger vortex, which pushes back, and disperses the plume more than the pressure boundary condition in option 2. It is also noticeable that the velocity vectors in option two points out of the outlet boundary, which indicates that water is leaving the domain.

4.2.4. INITIAL CONDITIONS

The purpose of this study was mainly to investigate the oscillating behaviour of the Becker case. Therefore, to save computational time only four base cases were initialized at $t = 0$ with an empty column. The four base cases differed only in the choice of turbulence model, as this was something that was thought to have a large impact on the flow. Thus the three first base cases were executed with the standard, RNG and Realizable $k-\epsilon$ models, and the fourth was executed with the Reynolds stress model. The base cases were simulated for a flow time of 200 seconds. The developed flow field from the base cases were then used as initial fields in the remaining test cases with the corresponding turbulence model.

5

Results and Discussion

5.1. Influence of turbulence model

Firstly, the model was tested for the different turbulence closure models that were available in Fluent 15. All of the cases presented in this section included virtual mass, turbulent dispersion and two-way coupling, which was calculated using the model by Simonin and Viollet [18]. The turbulence models were evaluated with the drag models of Schiller and Nauman [14] and Tomiyama *et al.* [17] respectively. All cases were initialized at $t = 200$ s using the developed flow fields described in Appendix B. The $k-\epsilon$ models were discretized by the QUICK scheme, and the Reynolds Stress cases by the Second order Upwind scheme for stability reasons.

Snapshots of the flow- and volume fraction fields for the different turbulence models with the Schiller Naumann drag model, are shown in figures 5.1 - 5.5. From a brief qualitative look at all the cases, it can be concluded that all turbulence models yields vortices that are moving down, causing the plume to oscillate. Figure 5.1 shows snapshots from a simulation made with the standard $k-\epsilon$ model. It can be seen that a vortex is formed in the upper left corner, and is moving down. It is interesting to note that the vortex moves all the way down before it dissipates, thus causing the plume to detach from the left wall. This behaviour was not seen in the experiments by Becker *et al.* [5], who observed that the lower part of the plume always remained stable. Loncle [4] did observe that the lower portion the plume were stationary at all times. But refining the mesh in the y-direction caused it to become instationary.

Figure 5.2 show snapshots from a simulation using the Realizable $k-\epsilon$ model. Qualitatively, it is very similar to the simulation with the standard $k-\epsilon$ model that is depicted in figure 5.1. But it can be observed that the vortices does not have the same position in time. Thus suggesting that the models does not reach a quasi steady-state at the same point in time.

Figure 5.3 show snapshots from a simulation using the RNG $k-\epsilon$ model. The movement and appearance of the bubble plume differs from that of the other $k-\epsilon$ models. Firstly, it can be observed that the dispersion effect due to turbulence is smaller than was observed in figures 5.1 and 5.2. Secondly, the upper left vortex dissipates earlier than with the other $k-\epsilon$ models, thus it does not cause the plume to bend towards the right wall.

Figures 5.4 and 5.5 show snapshots from simulations made with the Reynolds stress model, using both a linear and quadratic pressure-strain model. The snapshots show less dispersion than the standard and realizable $k-\epsilon$ models, but slightly more dispersion than the RNG $k-\epsilon$ model. The linear and quadratic pressure strain models seem to produce qualitatively similar results.

The snapshots only give a rough qualitative comparison between the models. For the purpose of more easily comparing the data, a time series similar to the one presented by Becker *et al.* [5] was recorded for each case with the Schiller-Naumann drag model. These can be viewed in figure 5.6. In figure 5.6 it can be seen that the vertical liquid velocity oscillate in a periodic fashion for all cases. The oscillation corresponds to the vortex from the left corner moving downwards, with the minimum velocity being the point in time where the kernel

of the vortex is aligned with the monitor point. The standard and Realizable $k-\epsilon$ models produces a constant oscillation frequency of 34.5 and 33.5 seconds respectively, whereas the Reynolds stress and RNG $k-\epsilon$ model oscillates with a non constant frequency. It can also be observed that the RNG $k-\epsilon$ model oscillates in a more chaotic fashion than the other turbulence models, where several wiggles are present. Another observation that can be made is that the amplitude of the oscillations varies in a constant manner, which was also observed in the studies made by Oey *et al.* [31].

Figure 5.7 shows time series of the vertical water velocity in the monitor point with different turbulence models using the drag model by Tomiyama *et al.* [17]. It shows a higher amplitude than with the Schiller Naumann drag model, but the oscillation frequency is the same. The case with the RNG $k-\epsilon$ model is shown separately in figure 5.8. The fluctuations are more pronounced than with the Schiller Naumann model, and large dips in the middle of the peaks can be observed.

It can be concluded that the choice of turbulence closure has a large impact on the predicted flow field. Therefore, all subsequent benchmarks were made from the point of view of different turbulence models. Figure 5.9 shows three quick snapshots of the velocity dip in figure 5.8. It shows that the dip is caused by a merging of the two left vortices whilst the left one dissipates. Then a new vortex is formed in the upper left corner.

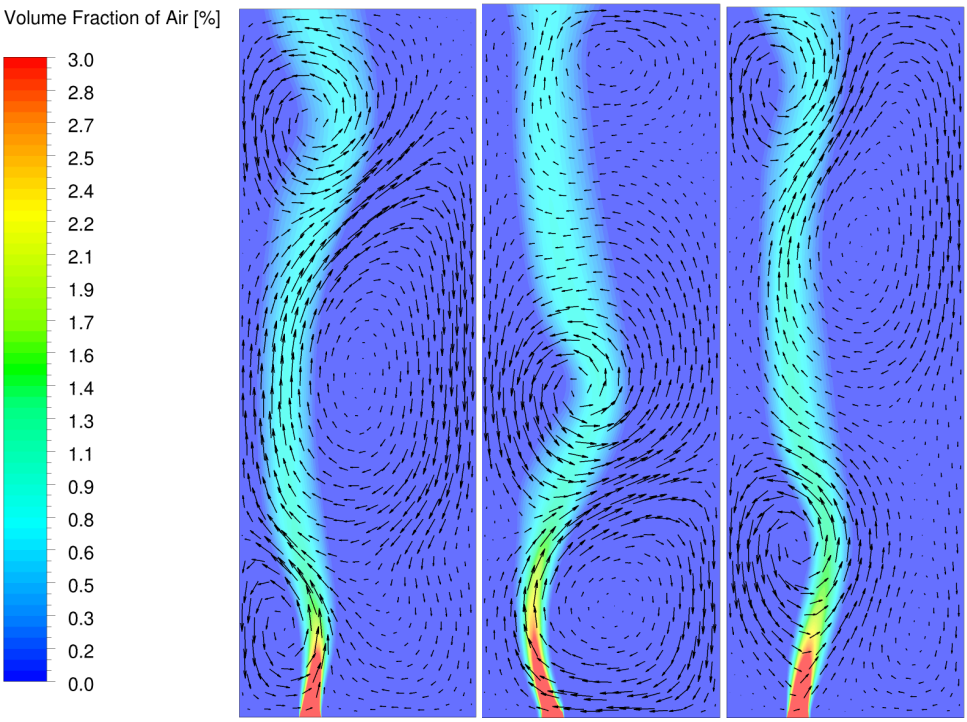

(a) $t = 265\ s$ (b) $t = 280\ s$ (c) $t = 295\ s$

Figure 5.1: Snapshots of the flow field at different times with the standard $k-\epsilon$ model.

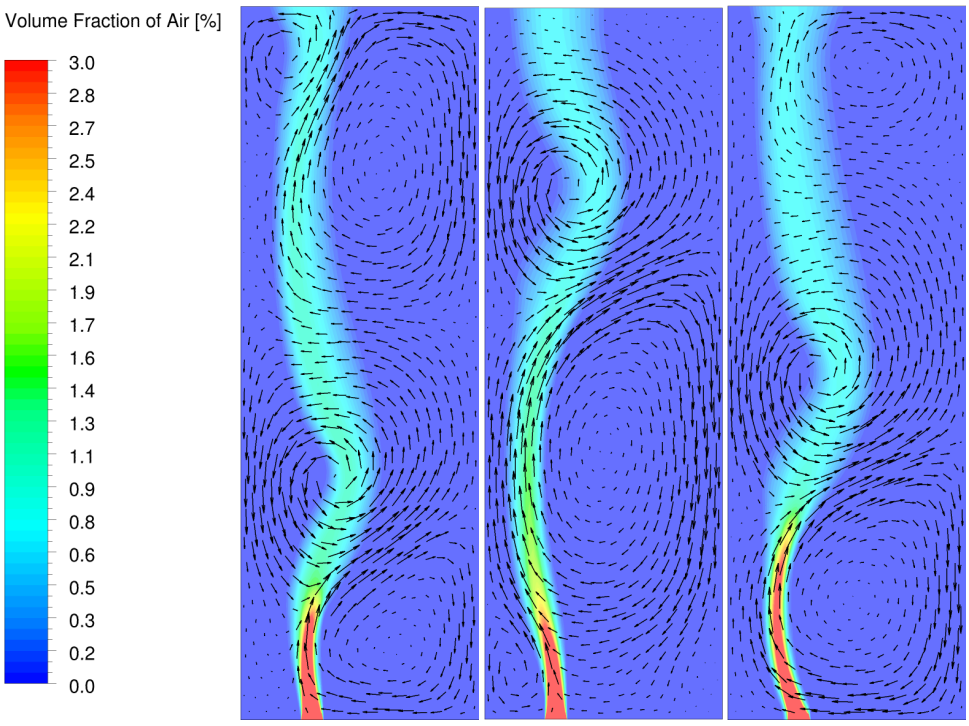

(a) $t = 265\ s$ (b) $t = 280\ s$ (c) $t = 290\ s$

Figure 5.2: Snapshots of the flow field at different times with the Realizable $k-\epsilon$ model.

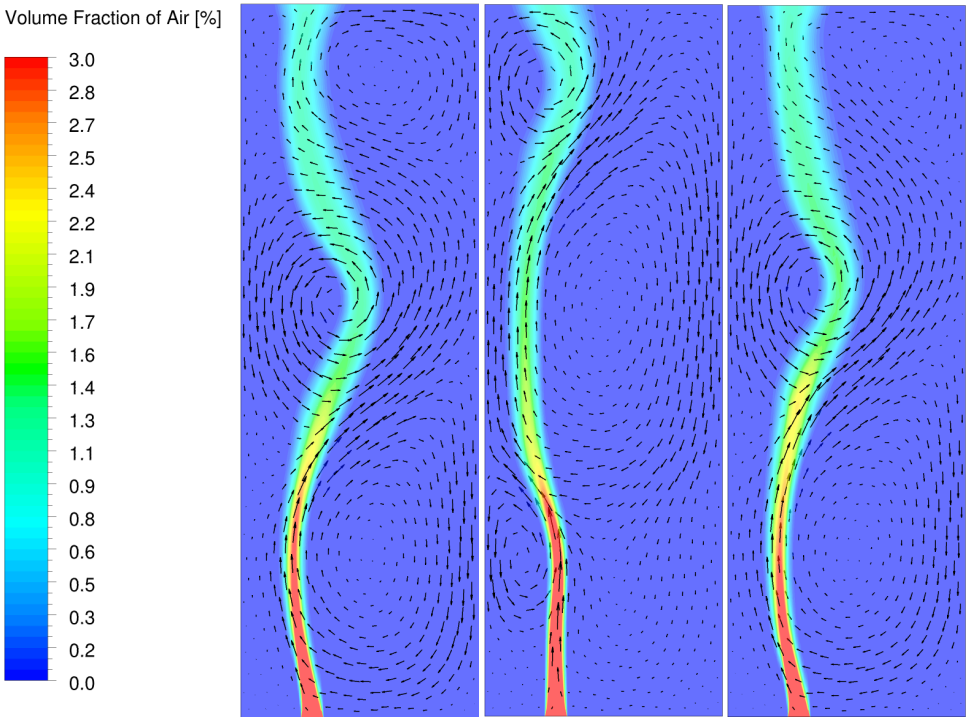

(a) $t = 265\ s$ (b) $t = 280\ s$ (c) $t = 295\ s$

Figure 5.3: Snapshots of the flow field at different times with the RNG $k-\epsilon$ model.

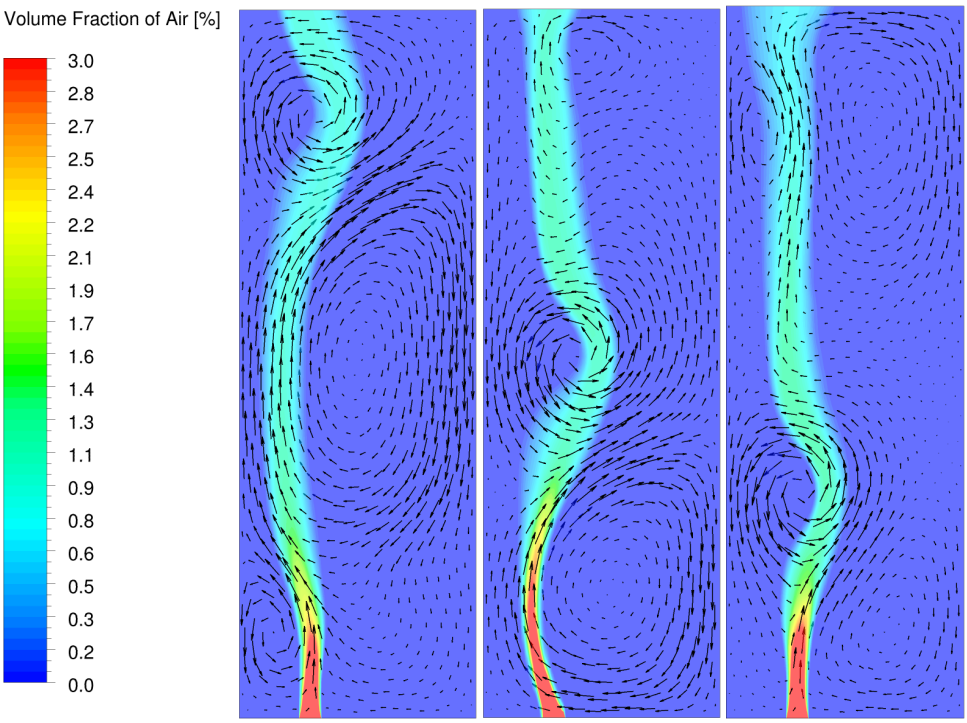

(a) $t = 265\ s$ (b) $t = 280\ s$ (c) $t = 295\ s$

Figure 5.4: Snapshots of the flow field at different times with the Reynolds stress model using a linear relation between pressure and strain.

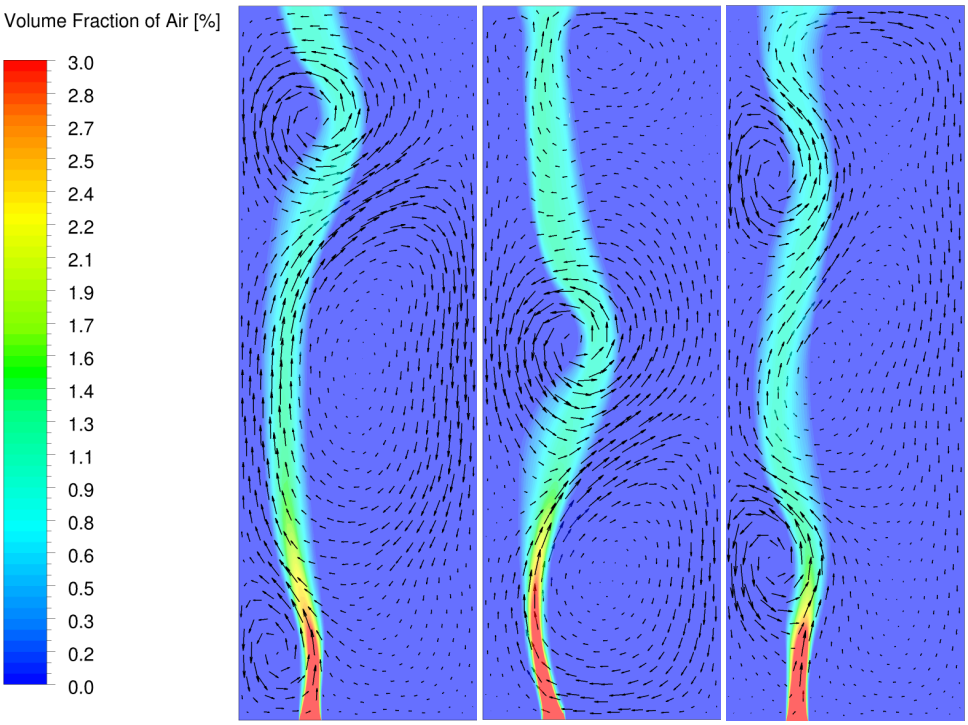

(a) $t = 265\ s$ (b) $t = 280\ s$ (c) $t = 295\ s$

Figure 5.5: Snapshots of the flow field at different times with the Reynolds stress model using a quadratic relation between pressure and strain.

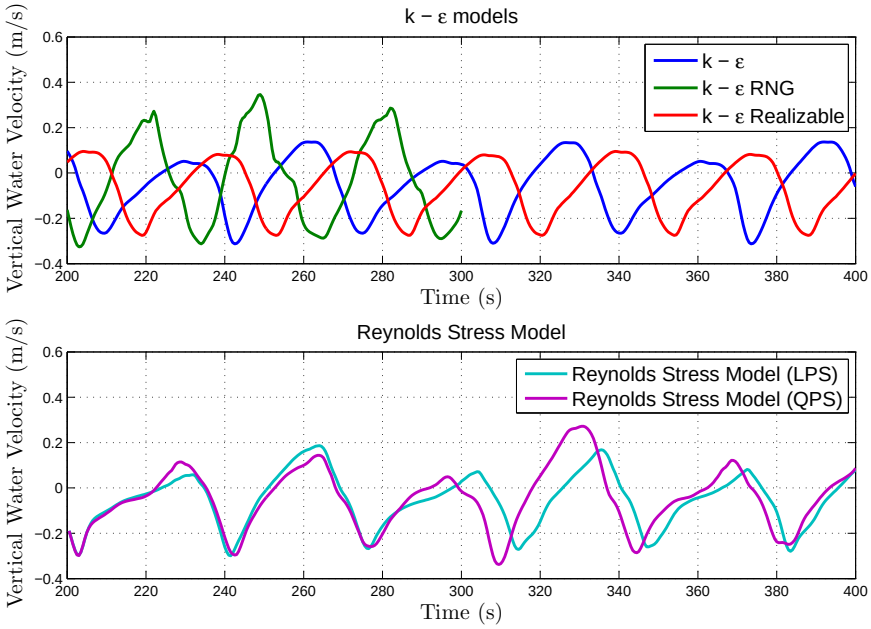

Figure 5.6: Vertical liquid velocity at the monitor point with different turbulence models, using the Schiller-Naumann drag model.

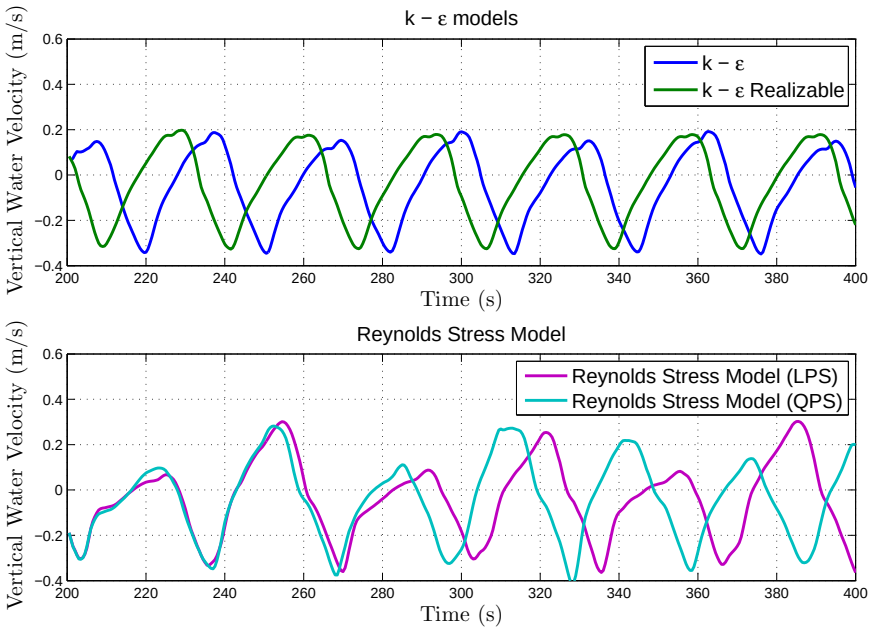

Figure 5.7: Vertical liquid velocity at the monitor point with different turbulence models, using the Tomiyama drag model.

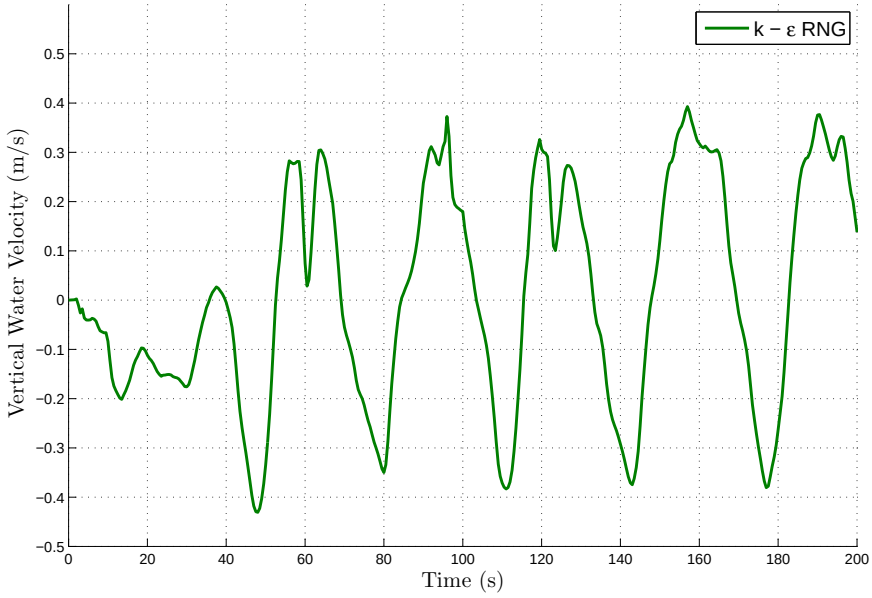

Figure 5.8: Vertical liquid velocity at the monitor point with different turbulence models, using the Tomiyama drag model.

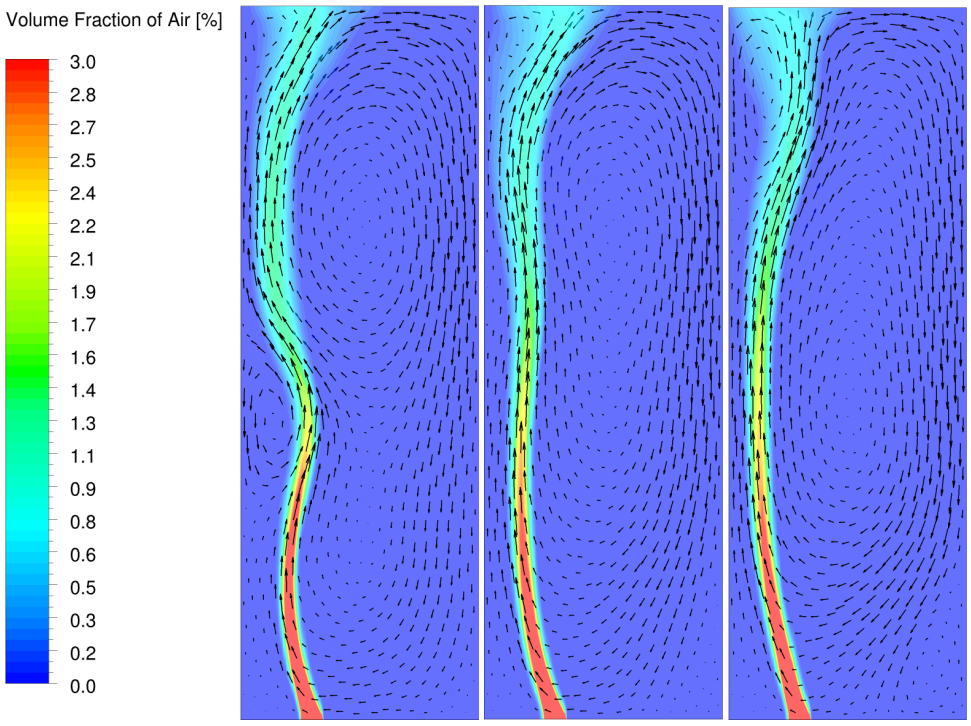

(a) $t = 119.5\ s$ (b) $t = 123.5\ s$ (c) $t = 126.5\ s$

Figure 5.9: Snapshots of the flow field at different times with the Reynolds stress model using a quadratic relation between pressure and strain.

5.2. INFLUENCE OF SPATIAL DISCRETIZATION

The model was also tested with the different spatial discretization schemes and gradient limiters that was described in section 2.5. A timestep of 5 ms was used, and the interaction force included virtual mass, the drag model by Schiller and Nauman [14], the turbulent dispersion- and two way coupling models by Simonin and Viollet [18]. Figure 5.10 depicts the effect of different discretization schemes and gradient limiters on the oscillation frequency using the standard $k-\epsilon$ model. It shows that neither the discretization scheme nor the gradient limiter has any significant influence on the oscillation frequency. However, if a closer look is taken, it can be seen that the difference between the QUICK- and second order upwind scheme increases as the flow time progresses. This could be attributed to the increased numerical diffusion from the second order upwind scheme.

Figure 5.11 shows how discretization and gradient limiter affects the oscillation frequency with the RNG $k-\epsilon$ model. It shows that the RNG $k-\epsilon$ produces an oscillating but chaotic solution. The choice of discretization scheme and gradient limiter has an impact, but it is not possible say which discretization scheme is favourable. If the residuals are examined, it can be noted that several time steps does not reach the prescribed convergence criteria if the multidimensional gradient limiter is used with both discretization schemes.

Figure 5.12 shows the effect of different discretization schemes and gradient limiters on the oscillations frequency using the Realizable $k-\epsilon$ model. It shows that the choice of discretization scheme has a small effect, where the overlap between the QUICK and Second Order Upwind cases decreases over time, possibly due to numerical diffusion. This was also present in the case where the standard $k-\epsilon$ model was used.

It clearly shows that the QUICK scheme is favourable due to it predicting a steady oscillation period, and being more accurate than the Second order Upwind scheme. Since there were no signs of the solution being numerically unstable, the QUICK scheme with the standard gradien limiter will be used to discretize all $k-\epsilon$ cases henceforth.

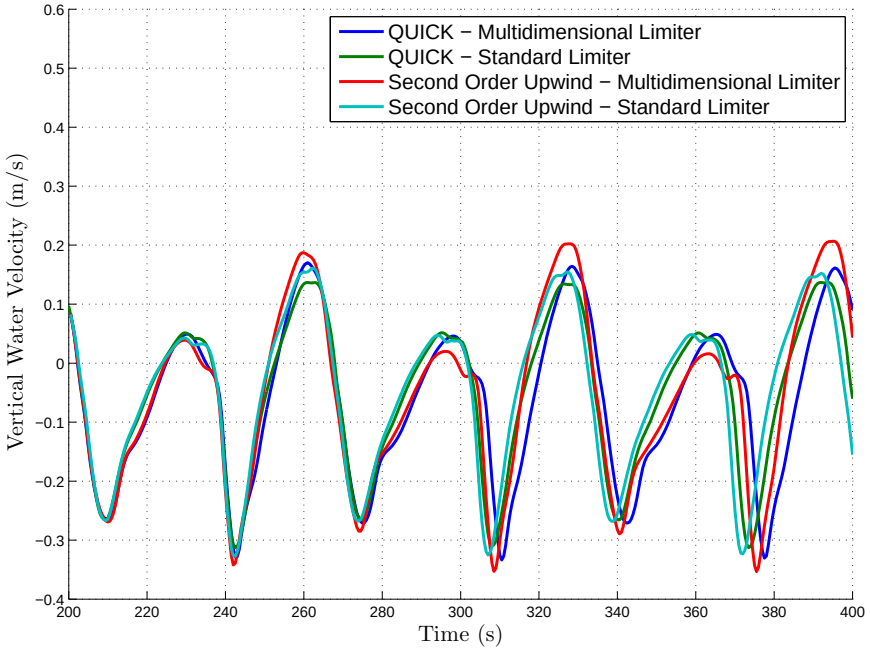

Figure 5.10: Vertical liquid velocity at the monitor point with different spatial discretization schemes and gradient limiters using the standard $k-\epsilon$ turbulence model.

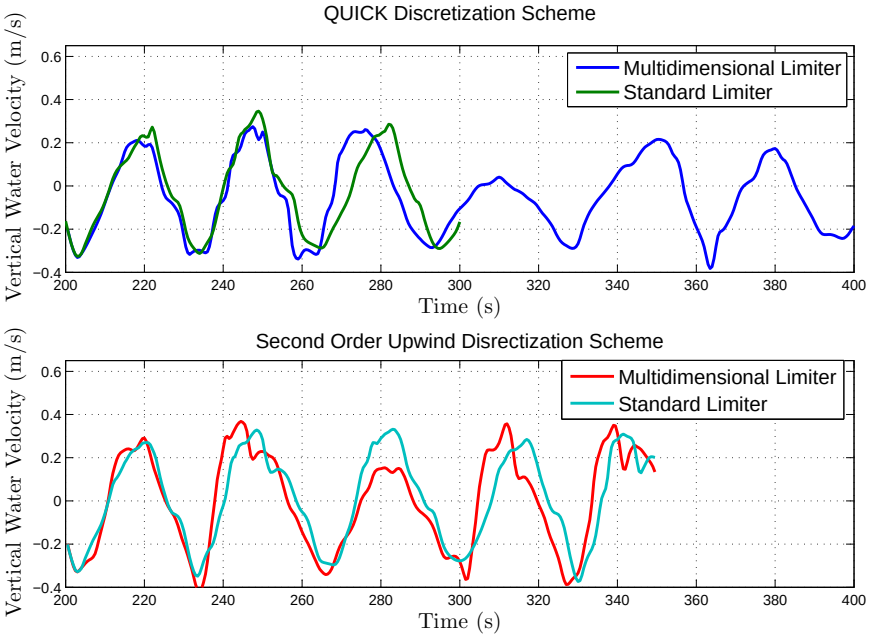

Figure 5.11: Vertical liquid velocity at the monitor point with different spatial discretization schemes and gradient limiters using the RNG $k-\epsilon$ turbulence model.

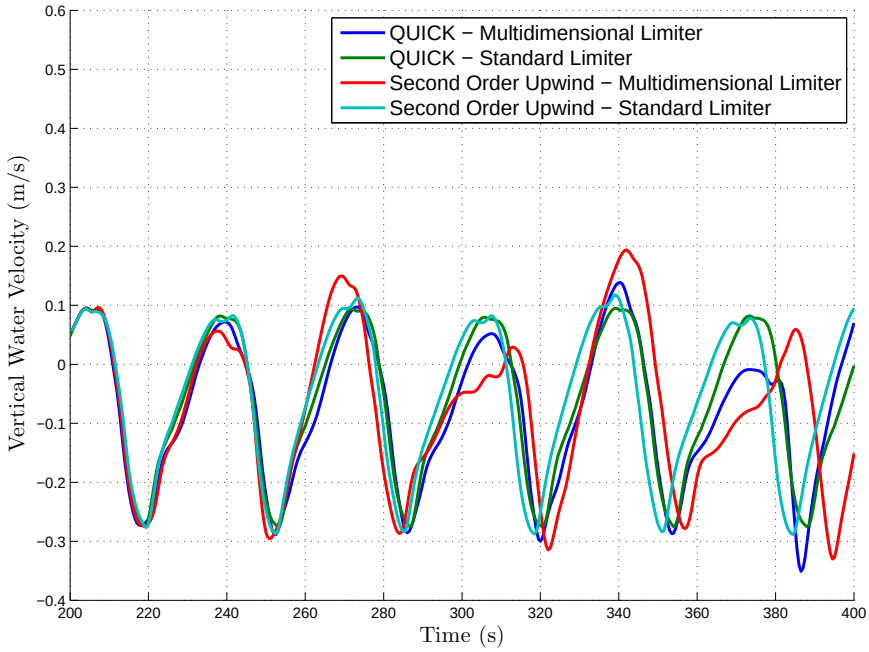

Figure 5.12: Vertical liquid velocity at the monitor point with different spatial discretization schemes and gradient limiters using the Realizable $k-\epsilon$ turbulence model.

5.3. INFLUENCE OF DRAG MODEL

The drag force is often cited as the main contributor to the interaction force term, and is often the only one considered. Therefore, a sensitivity analysis was performed to investigate the impact of choosing drag model with different turbulence models. The interaction force term also included the virtual mass force, the turbulent dispersion and two-way coupling by Simonin and Viollet [18]. The simulations were initialized at $t = 200$

s using the developed flow-fields in appendix B. Figure 5.13 shows the effect on the oscillation frequency with different drag models with the standard $k-\epsilon$ model. It shows that that the Schiller-Naumann- and Morsi-Alexander drag models produces an almost identical time series. This can be explained by looking at figure 2.1, which shows that the drag curves for the Schiller-Naumann and Morsi-Alexander models exactly overlaps until $Re_p \approx 2000$. This would be equivalent to the slip velocity being equal to $0.5\,\mathrm{m\,s^{-1}}$. It has not been suggested in any literature, nor in the calculations in appendix A that the slip velocity would be that high. It also shows that the amplitude alternates in a constant fashion, which could be explained by the fact that both drag models depends on the bubble Reynolds number, thus predicting a different drag coefficient depending on the current velocity. The Grace, Tomiyama and Universal drag models produces an almost identical oscillation period, but with a slightly different amplitude. Figure 2.1 shows that the Universal drag model predicts has the highest drag coefficient, and also has the highest amplitude whereas the Tomiyama and Grace drag models predicts a slightly lower drag coefficient and also has a slightly lower amplitude. None of the three previously mentioned drag models predicts the alternating amplitude that was observed in the cases with the Schiller-Naumann, and Morsi-Alexander models. The Grace, Tomiyama and Universal drag model assumes that the bubbles has reached a terminal velocity, and 2.1 shows that those models will predict a constant drag coefficient unless the bubble Reynolds number is low. All drag models predicts an oscillation frequency of 32.5 seconds if the standard $k-\epsilon$ model is used.

Figure 5.14 show the effect of using a different drag model with the RNG $k-\epsilon$ model. It shows that the RNG model again produces a much more chaotic time series than the standard $k-\epsilon$ model. The case with the RNG model does not show the same overlap as the other drag models. This would indicate that the chaotic nature of the oscillations, also makes the prediction of the drag coefficient vary in a much more chaotic way.

Figure 5.15 depict the time series from the monitor point, using different drag models with the Realizable $k-\epsilon$ model. The case with the Grace drag model was not initialized from a developed flow field, but instead initialized from $t = 0$ to test the effect of different initial values. The Schiller-Naumann and Morsi-Alexander drag models predicts a oscillation frequency of 34.5 and 34 seconds respectively. The Grace and Universal drag models predicts a oscillation frequency of 32.5 and 34 seconds respectively. The case with the Grace drag model is adjusted from the Universal drag model by about 8 seconds after about 60 seconds of flow time. This shows that initializing the simulation with developed flow field from a different flow field only affects the the solution by taking some time to adjust to steady state. The oscillation frequency of the Tomiyama model does not reach a state state, and increases with about 0.5 seconds every oscillation period. This was rather unexpected, as it was expected to follow the behaviour of the Grace- and Universal drag models due to the similar behaviour according to figure 2.1.

From varying the drag models it can be concluded that the Schiller-Naumann and Morsi-Alexander models produces very similar results. This would be expected since the models are very similar and based on the same assumptions. The remaining three models also produces results that are very similar to each other. All three are not based on the same assumptions as explained in chapter 2, but nevertheless they do predict very similar drag coefficients in the terminal regime for the system of air-water. The choice of drag model seems to have a large influence on the amplitude of the oscillations, where a higher drag coefficient increases the amplitude. The Universal drag model predicts an amplitude of approximately $0.2\,\mathrm{m\,s^{-1}}$, which is close to the amputate found by Becker *et al.* [5].

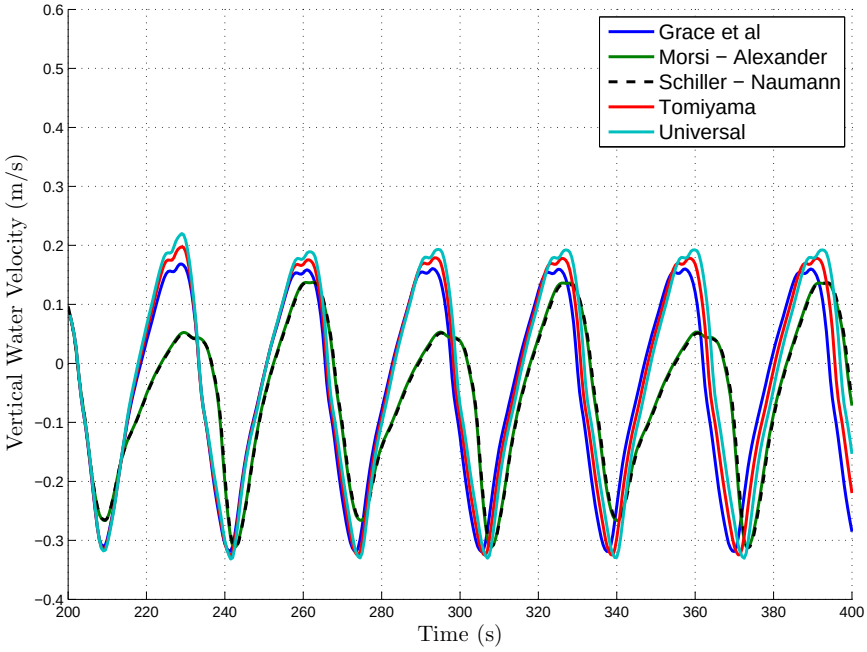

Figure 5.13: Vertical liquid velocity at the monitor point with different drag models with the standard $k-\epsilon$ model.

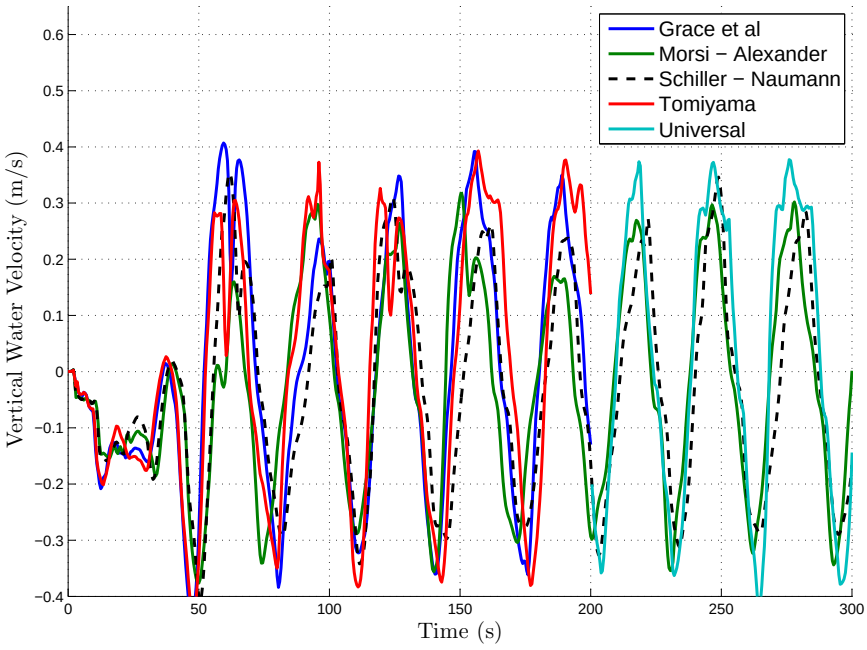

Figure 5.14: Vertical liquid velocity at the monitor point with different drag models with the RNG $k-\epsilon$ model.

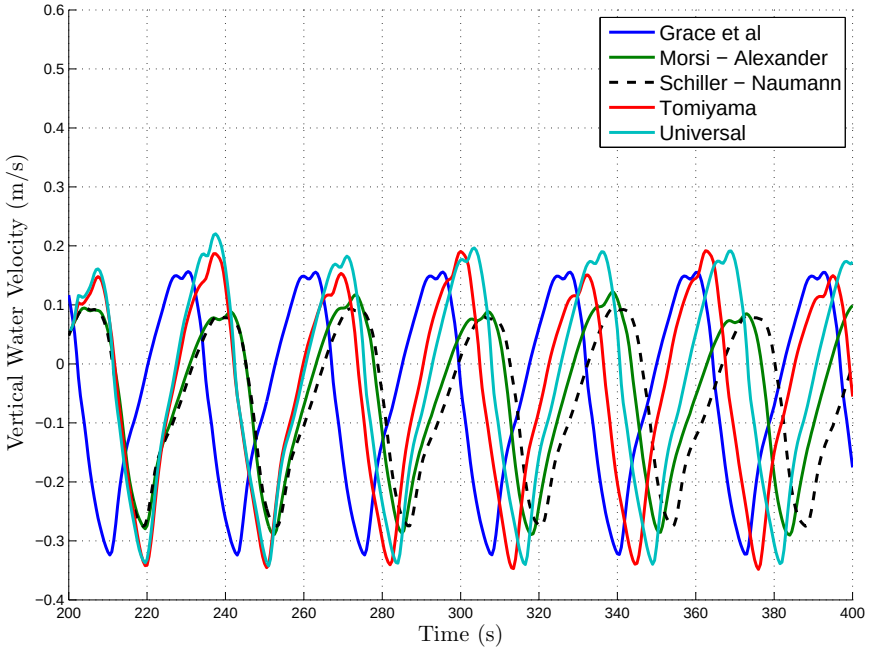

Figure 5.15: Vertical liquid velocity at the monitor point with different drag models with the Realizable $k-\epsilon$ model.

5.4. INFLUENCE OF TURBULENT TWO-WAY COUPLING

Turbulence modeling is an important factor when modelling two-phase flows. Therefore, it was also studied how modelling of the dispersed phase turbulence would affect the oscillation frequency. The interaction force term also included the virtual mass force, the turbulent dispersion by Simonin and Viollet [18] and the drag force model by Grace *et al.* [16]. The simulations were initialized at $t = 200$ s using the developed flowfields in appendix **?**], except the case of the Simonin model with the Realizable $k-\epsilon$.

Figure 5.16 show the effect of different two way coupling models with the standard $k-\epsilon$ model. It shows that the oscillation frequency is virtually indistinguishable for all cases expect if the model by Troshko and Hassan [27] is used, which produces a more chaotic time series, similar to the ones that have been produces by the RNG $k-\epsilon$ model. The predicted oscillation frequency is 32 seconds for the models that reaches a steady frequency.

Figure 5.17 show the effect of different two way coupling models with the RNG $k-\epsilon$ model. Here it is interesting to see that using the two way coupling model by Sato and Sekoguchi [28] adds stabilizes the RNG model in a way that has not been observed in any other simulation. However it still does not reach a steady oscillation frequency.

Figure 5.18 show the effect of different two way coupling models with the Realizable $k-\epsilon$ model. The result are identical to the case with the standard $k-\epsilon$ model, where all models except for the one by Troshko and Hassan [27] produces identical results.

It can be concluded that the two way coupling has little to no effect on the time series of the vertical water velocity, except in the case where the model by Troshko and Hassan [27] is used. The time series oscillates in the same chaotic fashion as has been observed with the $k-\epsilon$ RNG model. Figure 5.19 shows a time series of the eddy viscosity in the monitor point with different combinations of turbulence models, and models for two way coupling. It shows that if no two way coupling is included, the $k-\epsilon$ model predicts a higher eddy viscosity than the $k-\epsilon$ RNG model. But if the Troshko-Hassan model is included, the eddy viscosity is on more similar levels. Lastly, if the Sato model is used the $k-\epsilon$ RNG model predicts a higher eddy viscosity. Together with the observations that was made above, it suggest that the chaotic behaviour of the $k-\epsilon$ RNG model arises from under predicting the eddy viscosity. This might be due to the differential eddy viscosity model that is supposed to account for low Reynolds number effects, but as shown in these cases it produces a chaotic vertical velocity time series. This goes against the whole idea of Reynolds averaging, where small disturbances should be averaged out in time.

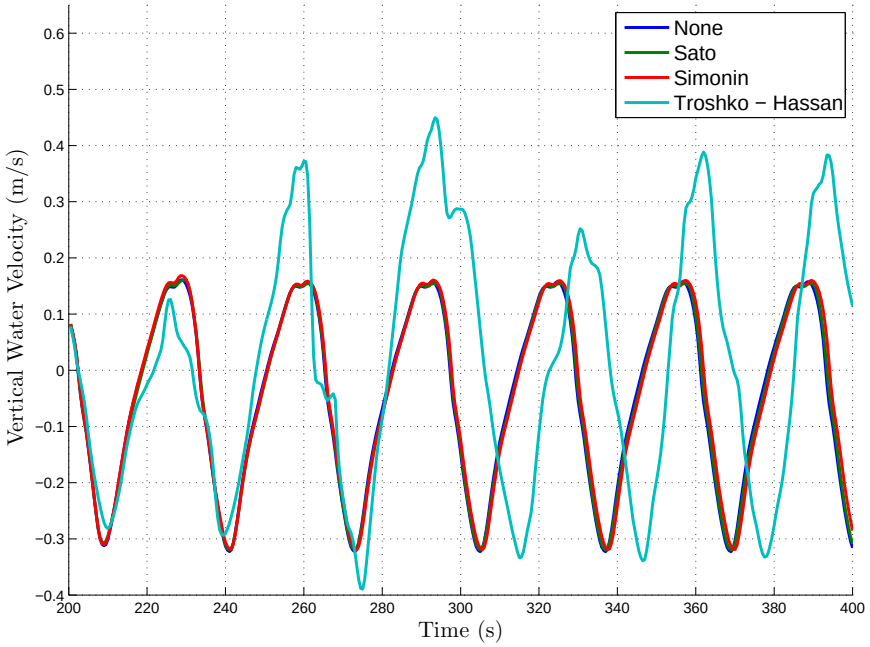

Figure 5.16: Vertical liquid velocity at the monitor point with different models for turbulent two-way coupling with the Standard $k-\epsilon$ model.

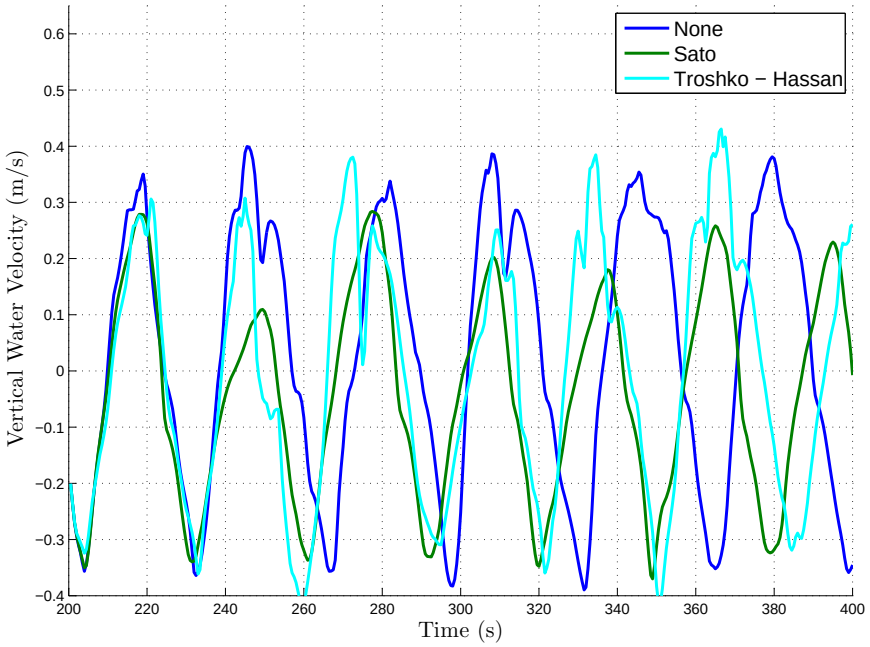

Figure 5.17: Vertical liquid velocity at the monitor point with different models for turbulent two-way coupling with the RNG $k-\epsilon$ model.

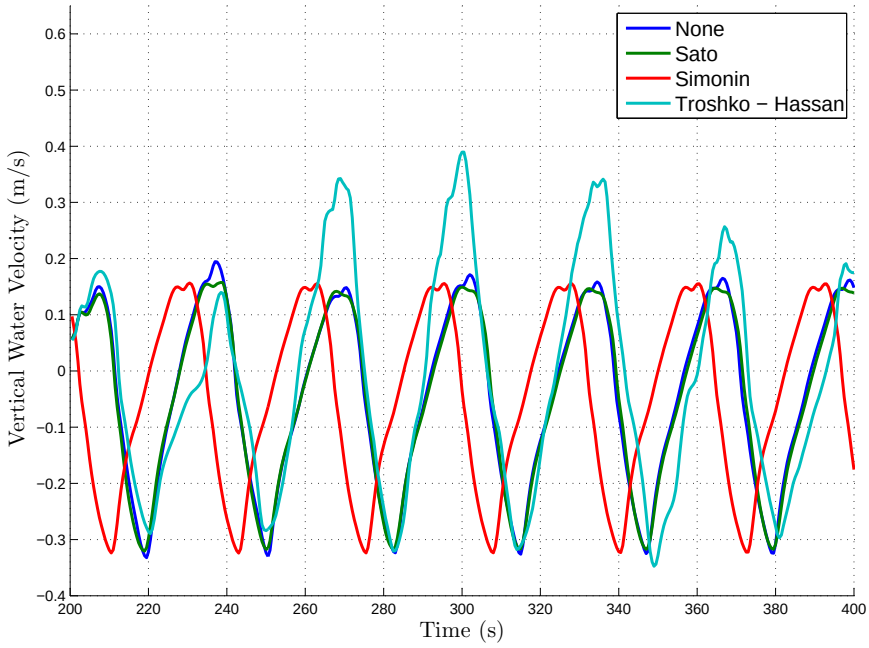

Figure 5.18: Vertical liquid velocity at the monitor point with different models for turbulent two-way coupling with the Realizable $k-\epsilon$ model.

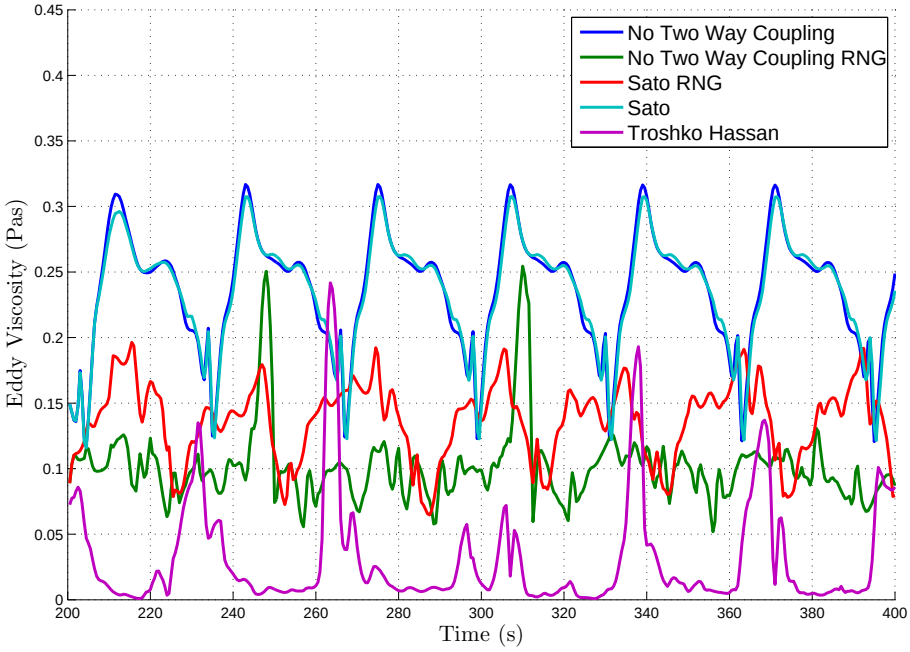

Figure 5.19: Eddy viscosity at the monitor point with different models for turbulent two-way coupling with the standard- and RNG $k-\epsilon$ model.

5.5. INFLUENCE OF TURBULENT DISPERSION

The standard $k-\epsilon$ model was also tested with two different models for turbulent dispersion, which is shown in figure 5.20. It show that the turbulent dispersion model has very little influence on the oscillation frequency. However, the turbulent diffusion force were expected to have an influence on the dispersion of the bubble plume. Snapshots at $t = 265$ s is shown in figure 5.21. It show that the turbulent dispersion force has some significant influence on the volume fraction field. If the turbulent dispersion force is completely neglected, the plume hardly disperses at all. Thus, the turbulent dispersion force should definitely be included.

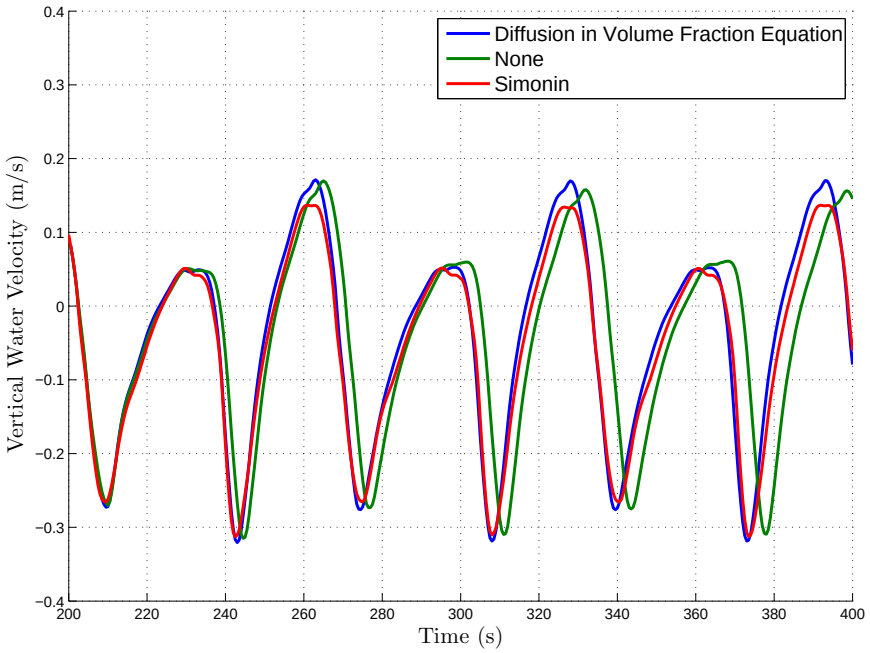

Figure 5.20: Vertical liquid velocity at the monitor point with different models for turbulent dispersion with the standard $k-\epsilon$ model.

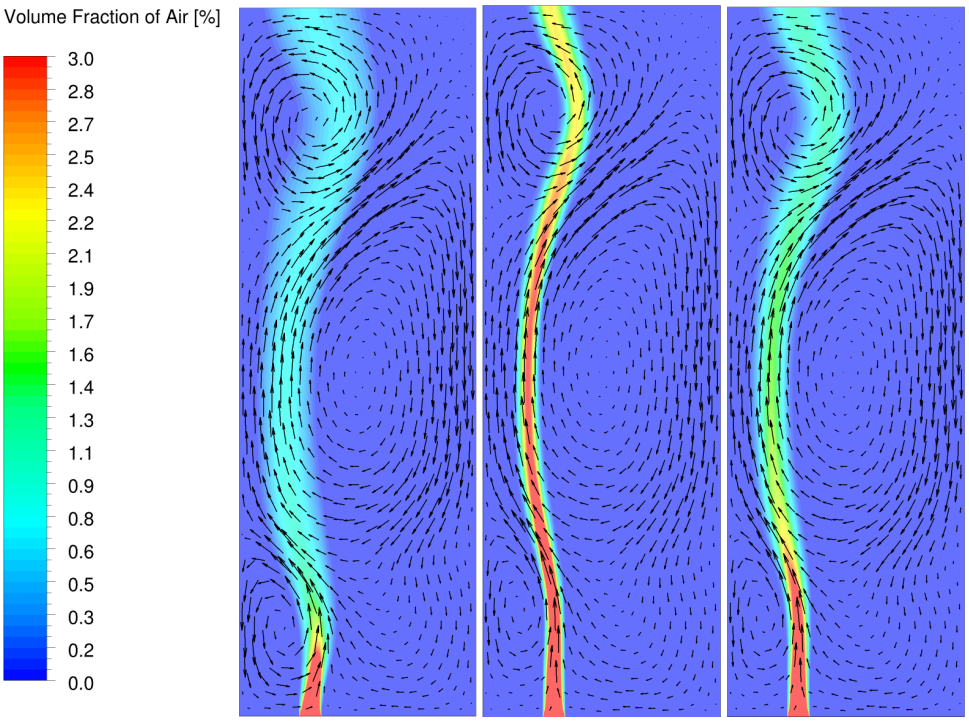

(a) Simonin's model (b) No Model (c) Diffusion in VOF

Figure 5.21: Snapshots of the flow field at $t = 265$ s with the $k-\epsilon$ model, showing the effect of using different models for turbulent dispersion

5.6. INFLUENCE OF LIFT- AND WALL LUBRICATION FORCE

Another test was made where the lift force was included in the interaction force term. In addition to lift, the interaction force included virtual mass, the drag model by Schiller and Nauman [14], the turbulent dispersion and two way coupling models by Simonin and Viollet [18]. A time step of 5 ms was used. The simulations Figure 5.22 depicts the time series of the vertical water velocity in the monitor point. It shows that the lift force does not affect the oscillation frequency, but has a small effect on the amplitude, causing the gap between the alternating peaks to be smaller. Figure 5.22 show that the lift force causes the bubble plume to disperse slightly more. This was expected since the lift force is known to push the dispersed phase perpendicular to the flow direction. If the volume fraction field is instead viewed from above as in figure 5.24, a it can be seen that the lift force also pushes the gas towards the nearby wall, where it accumulates. This is not observed in any experiments. The cause of this phenomena might be due to the no slip condition at the nearby wall, which stops the lift force from further dispersing the bubbles near the wall. All observations regarding the lift force coincides with what was found by Loncle [4].

Another test was made using the same setup as above, but with the Reynolds Stress model and the drag model by Tomiyama *et al.* [17]. In addition to the lift force, the wall lubrication force was also included since it is known to push the dispersed phase away from the wall, and it might counteract the pushing phenomena that was observed when the lift force was included whilst keeping its dispersive effect. Figure 5.23 show how the vertical velocity in the monitor point is affected by the inclusion of lift and wall lubrication forces with the Reynolds stress model. It shows that including the lift force causes the curves to eventually separate after a while, whilst including the lift force has a very small effect on the oscillation frequency. Figure 5.26 shows how the flow and volume fraction field is affected by introducing the lift and wall lubrication forces. Thus, lift force has the same effect on the Reynolds stress model as it has on the $k-\epsilon$ model. The introduction of the wall lubrication force does not have a significant influence on the flow and volume fraction field from this point of view. However, figure 5.27 show the volume fraction field from above, and it can be seen that the wall lubrication force does push the dispersed phase back from the wall if used together with the lift force. In conclusion, the lift force does not have any significant effect on the oscillation frequency but it does increase the dispersion of the plume. But the lift force is only active close to the walls due to the no slip condition.

Thus if a wall is in close proximity of the bubble plume, the wall lubrication force should also be included to counteract this phenomena.

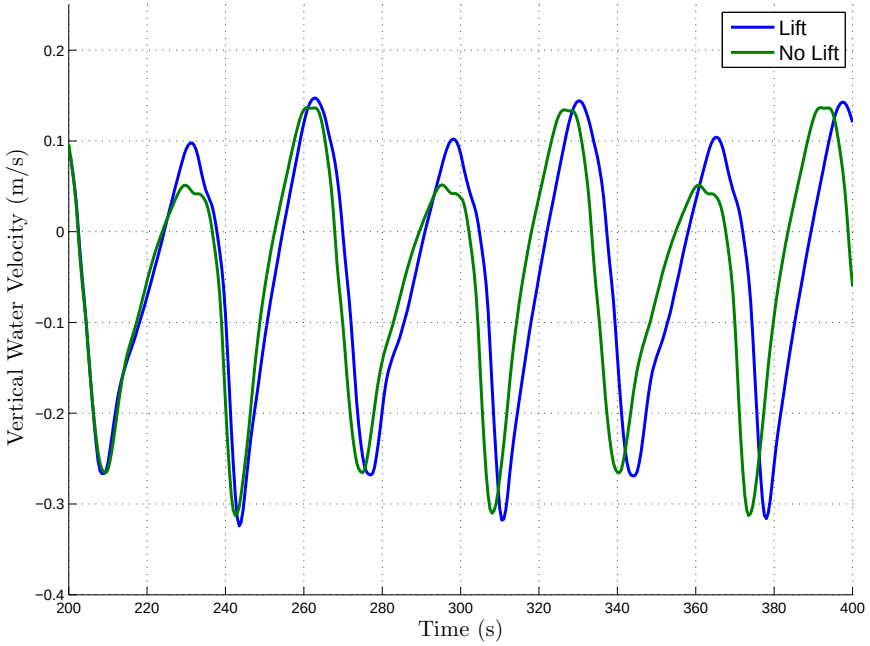

Figure 5.22: Vertical liquid velocity at the monitor point with the standard $k-\epsilon$ model. The effect of including the lift force is shown.

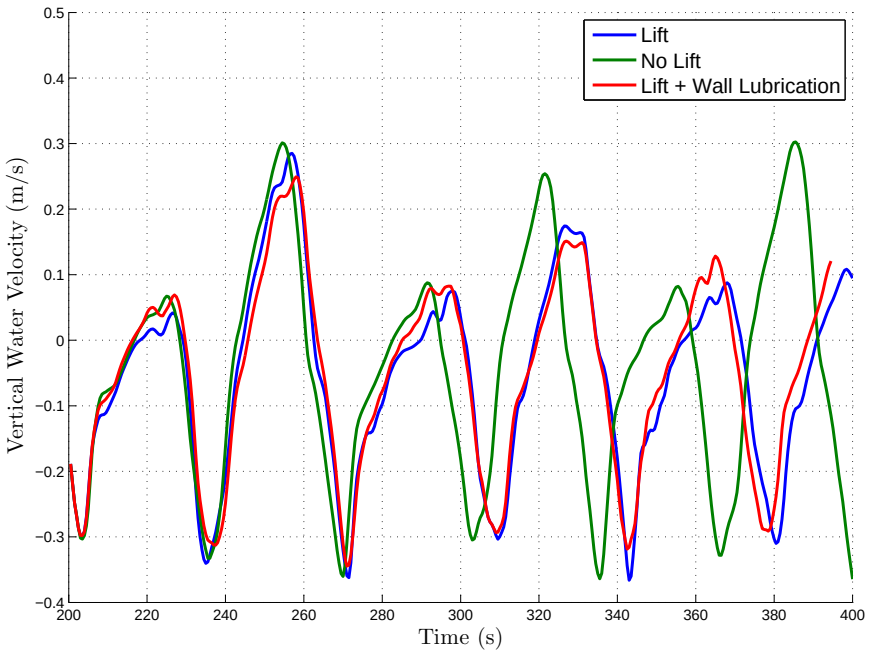

Figure 5.23: Vertical liquid velocity at the monitor point with the Reynolds stress model. The effect of including the lift- and wall lubrication force is shown.

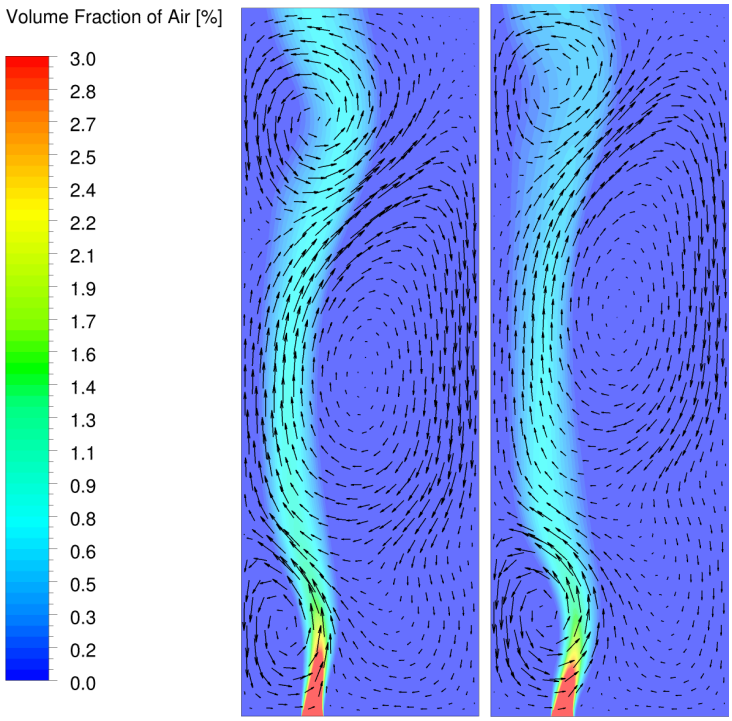

(a) No Lift (b) Lift

Figure 5.24: Snapshots of the volume fraction and flow field at $t = 265$ s, showing the effect of including the lift force together with the $k-\epsilon$ model.

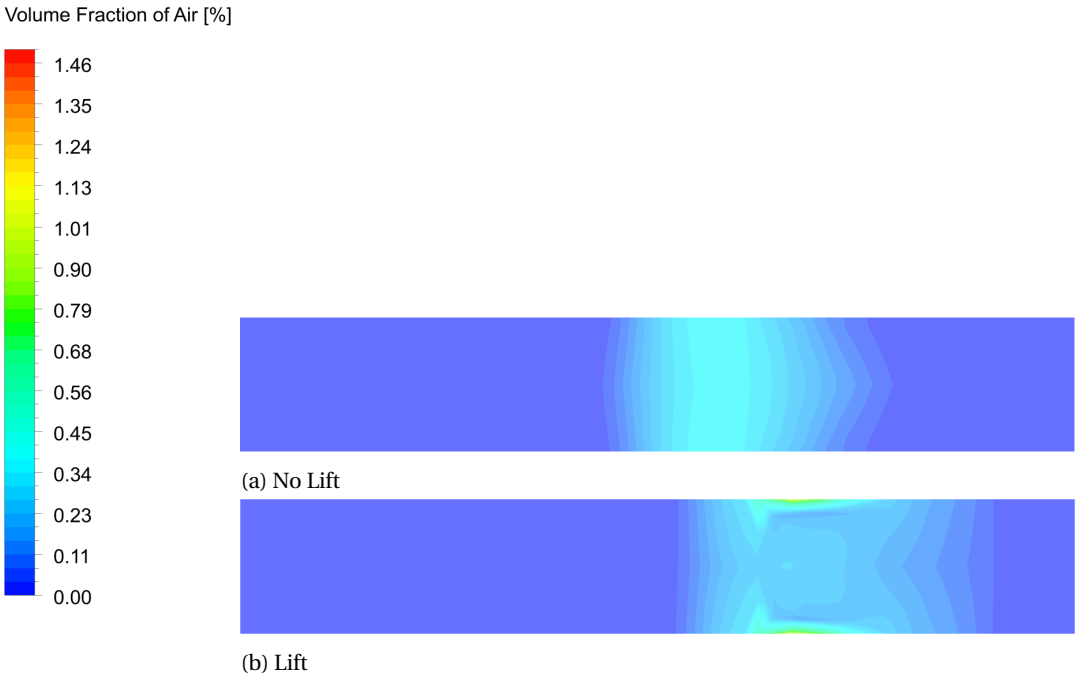

(a) No Lift

(b) Lift

Figure 5.25: Snapshots of the flow field viewed from above at $H = 1.2$ m and $t = 265$ s, showing the influence of the lift force.

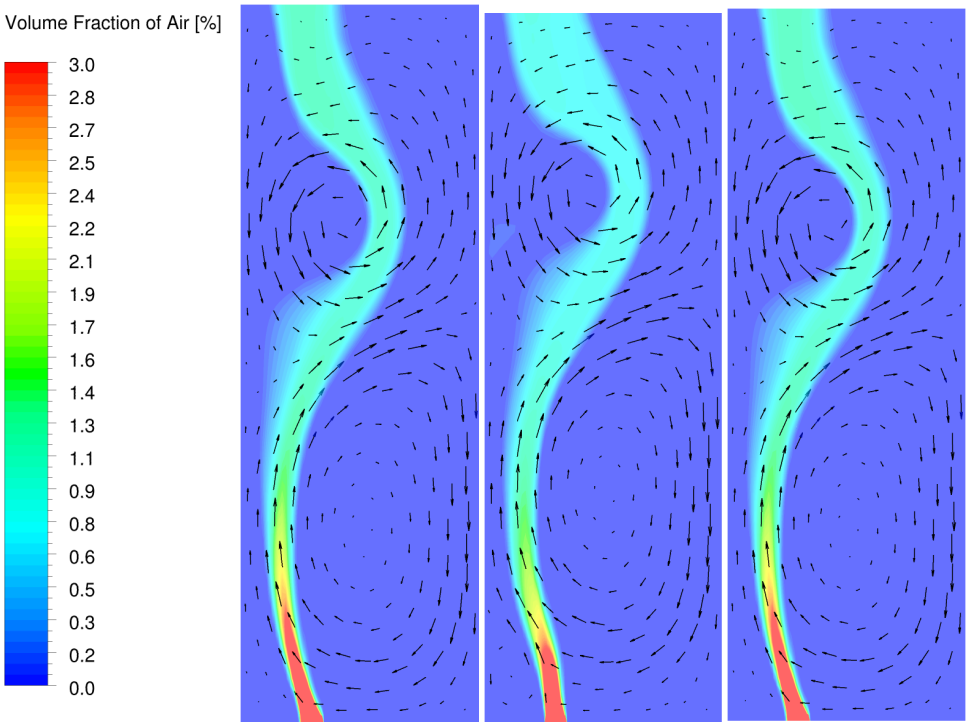

Figure 5.26: Snapshots of the flow and volume fraction field at $t = 265$ s, showing the effect of including the lift and wall lubrication force.

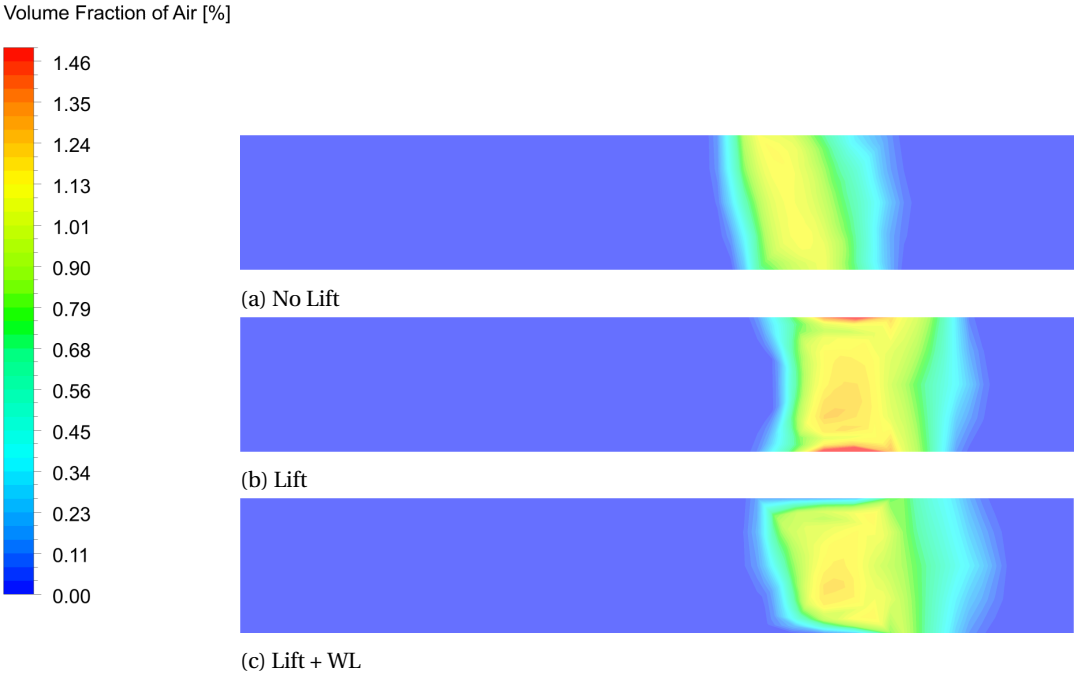

Figure 5.27: Snapshots of the flow field viewed from above at $H = 1.2$ m and $t = 350$ s, showing the influence of the lift and wall lubrication force with the Reynolds stress model. Note that the legend scale is different than figure 5.25

5.7. INFLUENCE OF TIME STEP

The influence of changing time step was also investigated. For this purpose, the standard $k-\epsilon$ model was used. The interaction force term included virtual mass, the drag model by Tomiyama *et al.* [17] and the turbulent dispersion and two way coupling model by Simonin and Viollet [18]. The time step was lowered suc-

cessively from the standard time step of 5 ms to 4, 3 and 2.5 ms. The resulting time series of the vertical water in the monitor point is shown in figure 5.28. It shows that going from 5 ms to 4 ms has virtual no effect, and both time steps shows an oscillation frequency of 32 seconds. If the time step is lowered further to 3 ms, the oscillation period increases by about 2.5 s. When the time step is lowered again by 0.5 ms to 2.5 ms, a rather remarkable increase in the oscillation frequency occurs. The frequency never reaches a constant value, but the time between the first two peaks is 47 seconds. Between the second and the third peak, the period is 59 seconds, and between the third peak and the end of the simulation the period is 62 seconds, even though the water velocity has not peaked yet. This show that the time step has a remarkable influence on the oscillation frequency, that is unlike any other parameter that has been tested in this study.

A dependence on the time step in this fashion would suggest an issue with the Courant number. However, having a Courant number that is unsatisfactory would cause the solution to become unstable, which has not been observed. Ansys Fluent also uses implicit time stepping, which is unconditionally stable. This implies that this should not be an issue with the Courant number.

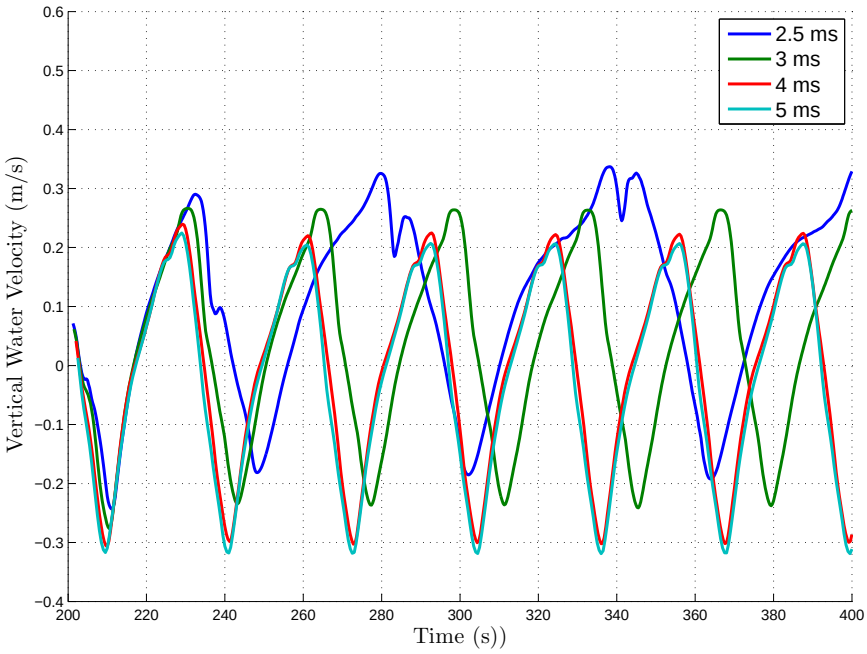

Figure 5.28: Vertical liquid velocity at the monitor point with the standard $k-\epsilon$ model. The effect of using different time steps is illustrated.

5.8. INFLUENCE OF GRID SIZE

The model was also tested for grid dependency. A second grid, finer grid with the same form as the standard grid in figure 4.1 was generated. The grid consisted of $75 \times 150 \times 6$ elements. Both cases were executed with a time step of 5 ms, and a interaction force term that included the virtual mass force, the drag force model by Schiller and Nauman [14] turbulent dispersion and two-way coupling by Simonin and Viollet [18]. Figure 5.29 show time series of the vertical water velocity in the monitor point for the two different grid sizes. It can be observed that the curves do not overlap, but the oscillation frequency is similar. It can then be concluded that running a simulating on a finer mesh takes the bubble plume slightly longer to reach a pseudo steady state than on the standard mesh. But the oscillation frequency can be considered to be independent of the two grids.

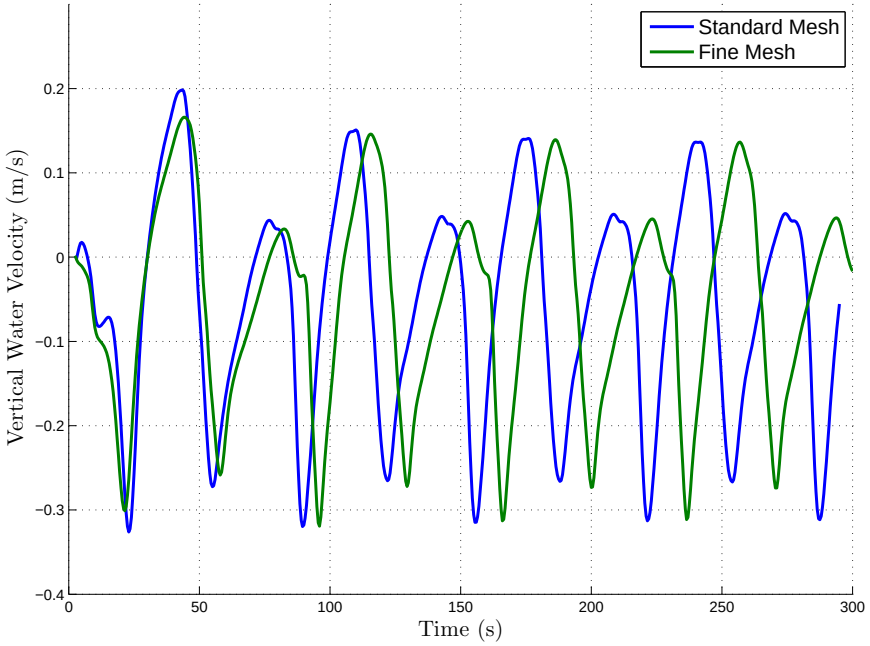

Figure 5.29: Vertical liquid velocity at the monitor point with the standard $k-\epsilon$ model. The effect of using two different grid sizes are shown.

6

Conclusions and Recommendations

In this study, simulations were performed on a rectangular, flat bubble column with an asymmetrically located frit sparger using the commercial CFD package Fluent from ANSYS. This chapter will answer the research questions that was posed in chapter 1, and provide recommendations for further usage and research.

6.1. Fluent Development

The first question posed in chapter 1 was that of whether Fluents multiphase capabilities had increased since 1999 when a similar research projected was conducted by Loncle [4]. The most prominent feature that has been introduced in Fluent since 1999 is two additional turbulence models, in the form of the Realizable $k-\epsilon$ model and the Reynolds stress model for multiphase flow. However these two models did not provide any improvement over the standard $k-\epsilon$ movement in terms of predicting the oscillation frequency of the bubble plume. The other major feature that has been introduced is the inclusion of the wall lubrication force, which was not used in any of the simulations by Loncle [4]. Newer versions of Fluent also offers many more models for the coefficients in the interaction force term. The second to last version of fluent also introduced the degassing boundary condition. Loncle [4] modelled the outlet by fixing the normal water velocity to $0\,\mathrm{m\,s^{-1}}$, and the normal air velocity to $0.2\,\mathrm{m\,s^{-1}}$ which was the assumed slip velocity. The degassing allows the outlet to be modelled as a free surface for the liquid face and as an outflow for the gas phase. The presence of a free surface was shown have effect on the formation of the vortex in the top left corner (figure 4.4), and this should serve as a substantial improvement.

6.2. Turbulence Modelling

As stated in the section above, never versions of Fluent has introduced two additional turbulence models, the Realizable $k-\epsilon$ and the Reynolds Stress model. The comparison of these newer models with the older standard and RNG $k-\epsilon$ models showed that the RNG $k-\epsilon$ and Reynolds stress model did not perform so well, with RNG $k-\epsilon$ performing the poorest. The RNG $k-\epsilon$ model very often produce an oscillating time series that never reaches a steady frequency, and the velocity fluctuates in a way that it should not do in a Reynolds averaged simulation. A sensitivity analysis with different models for turbulent two-way coupling showed that the cause of the velocity fluctuations were a under prediction of the eddy viscosity by the RNG $k-\epsilon$ model. An under prediction of the eddy viscosity causes the simulation to behave more as a non RANS simulation.

The standard and Realizable $k-\epsilon$ predicted a similar steady oscillation frequency between 32 and 33 seconds. The standard $k-\epsilon$ model predicted a higher amplitude than the Realizable $k-\epsilon$ model, but both model predicts an amplitude that is within the experimentally determined one by Becker *et al.* [5] in figure 3.4. As the standard and Realizable $k-\epsilon$ models both provided reasonable results, it is hard to say whichever is better. However, the standard $k-\epsilon$ model was less influenced by choosing a lower spatial discretization scheme than the Realizable $k-\epsilon$ model.

The Reynolds stress model performed rather poor, never reaching a steady oscillation frequency. With the the Linear pressure strain relation providing a more regular frequency than the quadratic relation. One explanation could be that all cases using the Reynolds stress model was discretized with the second order upwind

scheme instead of QUICK for stability reasons.

The inclusion of turbulent two-way coupling was shown to have virtually no effect on the oscillation frequency expect when the Troshko Hassan model was used. The Troshko Hassan model influenced the turbulent equations in such a way that the eddy viscosity was under predicted and caused velocity fluctuations with all turbulence models, similar to the ones that was present when the RNG $k-\epsilon$ model was used.

The inclusion of turbulent two-way coupling was shown to have virtually no effect on the oscillation frequency expect when the Troshko Hassan model was used. The Troshko Hassan model influenced the turbulent equations in such a way that the eddy viscosity was under predicted and caused velocity fluctuations with all turbulence models, similar to the ones that was present when the RNG $k-\epsilon$ model was used. In conclusion, the standard and Realizable $k-\epsilon$ models both showed promising results with virtually the same oscillation frequency, with the standard $k-\epsilon$ model performing the best. the RNG $k-\epsilon$ model performs poorly and underestimates the eddy viscosity.

6.3. INTERACTION FORCE

The interaction force is the most important feature of the Eulerian-Eulerian multiphase model. From the sensitivity study of the drag force it was concluded that the drag force has a major influence on the amplitude of the oscillations, with a higher drag coefficient leading to a higher amplitude. Fluent had two groups of drag models to choose from. One group of models that assumed the dispersed phase consisted of non deforming spherical bubbles that only depended on the bubble Reynolds number, and another group of models that incorporated the effect of deformation which depended only on the Eotovos and Morton number in the terminal regime. The difference in amplitude between the model groups were large, but within the group the differences were more subtle. Interestingly, it was possible to get a very good agreement with the simulated data by performing a simple force balance as shown in appendix A. The predicted slip velocity agreed almost perfectly with the one estimated by the force balance, thus highlighting that the drag force has a major influence on the predicted flow field.

The inclusion of the turbulent dispersion force did influence the dispersion of the bubble plume. If it was excluded the plume exhibited virtually no dispersion, thus showing that in this case it should always be included

Including the lift force did not have any significant impact on the oscillation frequency, and did not have the same impact on the solution as had been reported by many authors in the literature that performed studies on square bubble columns (Zhang *et al.* [33], Gupta and Roy [36]). The lift force only had a small dispersive effect, but also pushed the bubbles towards the back and from wall as was also reported by Loncle [4]. Including the wall lubrication force did counteract this effect, whilst keeping the dispersive properties of the lift force.

6.4. NUMERICAL METHODS

The spatial discretization did not have any noticeable effect other than that the QUICK scheme was shown to predict a steadier oscillation frequency. The multidimensional gradient limiter did reduce the stability of the solution, and using it together with the *RNG* prevented the model from converging. As the QUICK scheme provided the best results, and always kept its stability, it should be used in future studies as it is more accurate and less diffusive than the second order upwind scheme.

The time step was shown to have a large influence on the oscillation frequency, which started o increase rapidly if the time step was set lower than 4 ms. Decreasing the time step from 3 to 2.5 ms showed that the oscillation frequency doubled compared to that of using a time step of 5 ms. Thus showing that care should be taken when choosing time step, and that a time step of 5 ms is sufficient.

6.5. CONCLUSIONS

Fluent seems to have been a useful tool for modelling the wandering phenomena of the bubble plume, and manages to reproduce findings in literature. The results from this study are similar to those found by Loncle

[4], and Fluent does not seem to have changed in any major way other than adding more turbulence and interaction force models. Even so, the standard $k-\epsilon$ which was also available in Fluent at that time, was found to perform the best. The interaction force models for turbulent dispersion and two way coupling by Simonin and Viollet [18] that was used in the majority of the study was also available in Fluent in 1999, and changing models did not cause any significant change in the result. So other than being able do more computationally expensive simulation due to the better hardware that is available today, the current version of Fluent does not seem to be able to model the Becker case better than in 1999.

The biggest flaw of the Eulerian-Eulerian model is all the inherent uncertainty that comes from all the empirical models that are involved. This makes it hard for the user to properly chose which interaction force models that should be used. As computer hardware improves, it would be more interesting to move on to a Eulerian-Lagrangian modelling.

A

Estimating the Terminal Velocity of a Rising Bubble

When doing CFD simulations it is good practice to compare simulated data with estimated values from simple analytical models to ensure that the simulated data is in the right order of magnitude. This was done by calculating the terminal velocity of a single air bubble, rising in surrounding water.

When a single bubble has reached its terminal velocity, the drag force is equal to the buoyancy force:

$$F_D = F_B \tag{A.1}$$

The gravitational force was neglected due to the large density ratio between water and air. The magnitude of buoyancy force acting on the immersed bubble is equal to the weight of the surrounding water that is displaced by the bubble:

$$F_B = \rho_q V g \tag{A.2}$$

The drag force acting on the bubble can be calculated by the drag equation:

$$F_D = \frac{\rho_q (u_{\text{slip}} C_D A)}{2} \tag{A.3}$$

If equations A.2 and A.3 is inserted into equation A.1, and the volume of a bubble equals to $V = \frac{4}{3} r^3 \pi$ and its cross sectional area equals to $A = r^2 \pi$, the following simple expression can be derived for the terminal slip velocity:

$$u_{\text{slip}} = \sqrt{\frac{8gr}{3C_D}} \tag{A.4}$$

Equation A.4 was solved with all the drag coefficient models mentioned in section 2.3.1. The estimated slip velocities are shown in table A.1. If the estimated slip velocity is compared with the simulated column profile in figure A.1, it shows a near perfect agreement.

Table A.1: Estimated slip velocity for a single rising bubble with different drag models available in Ansys Fluent

Drag model	Estimated Slip Velocity (m/s)
Schiller - Naumann	0.34
Morsi - Alexander	0.34
Grace et al.	0.25
Tomiyama	0.24
Universal	0.23

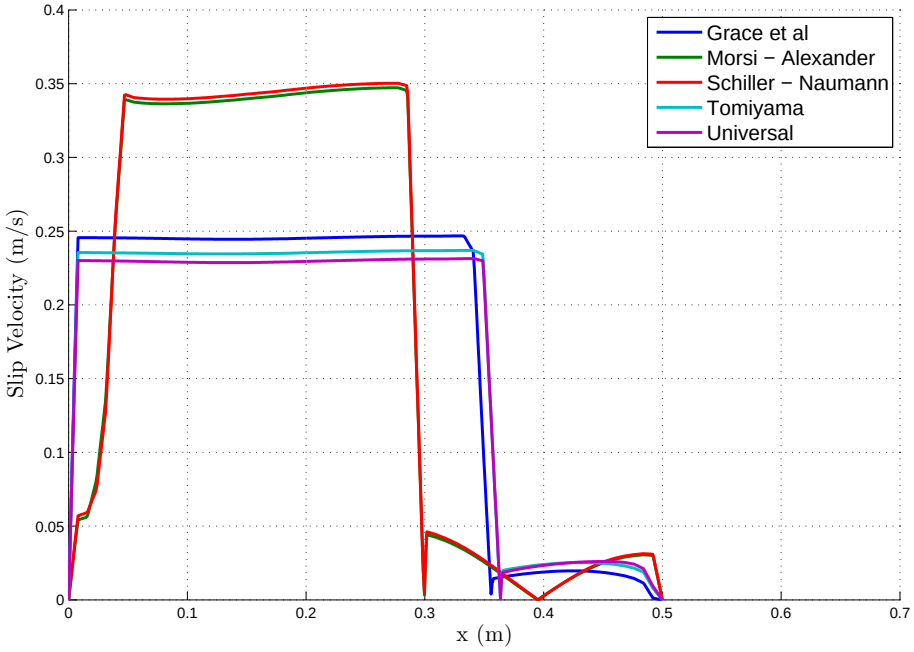

Figure A.1: The difference in vertical water and air velocity at the top of the column at $t = 300$.

B

INITIAL VALUES

To save time, the majority of the simulations made in this study were initialized from an already developed flow field that used a turbulence model that corresponded to the case setup. Three base cases were initially made to serve as initial field for the remaining simulations.

The interaction force term included contributions from virtual mass, the drag force by Schiller and Nauman [14], turbulent dispersion and two way coupling by Simonin and Viollet [18]. The time series from the monitor point is depicted in figure B.1

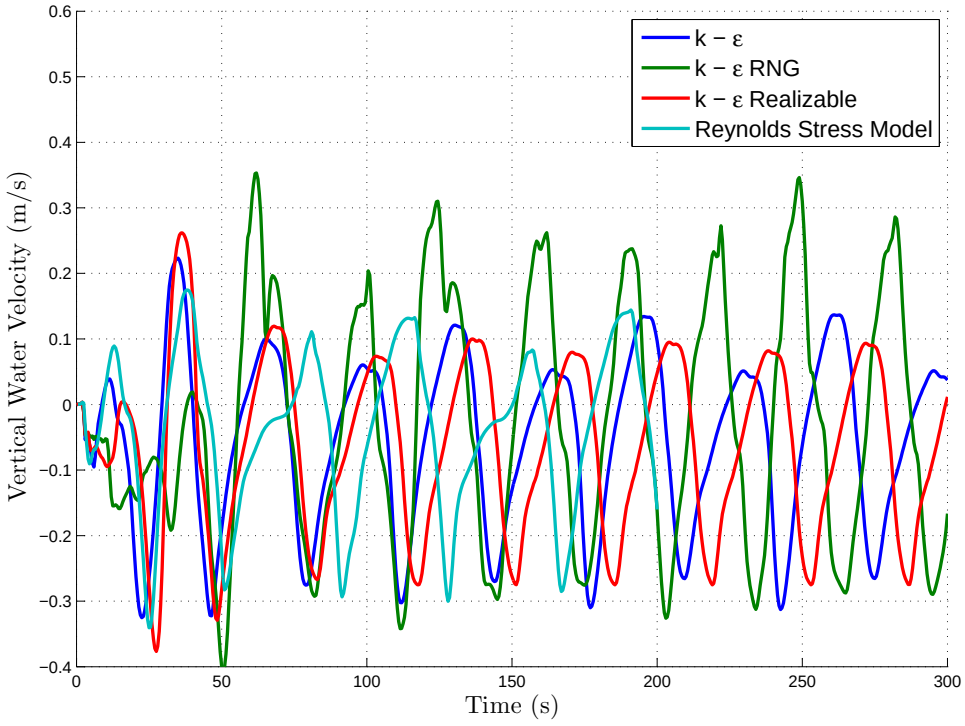

Figure B.1: Drag coefficient as a function of the Reynolds number for different drag models

BIBLIOGRAPHY

[1] T. Wilkinson and A. Spek, *Design parameters estimation for scale-up of high-pressure bubble columns,* AIChE Journal **38**, 544 (1992).

[2] R. Mudde and H. Van den Akker, *Dynamic behavior of the flow field of a bubble column at low to moderate gas fractions,* Chemical Engineering Science **54**, 4921 (1999).

[3] A. Sokolichin and G. Eigenberger, *Applicability of the standard $k-\epsilon$ turbulence model to de dynamic simulation of bubble columns: Part I. detailed numerical simulations,* Chemical Engineering Science **54**, 2273 (1999).

[4] C. Loncle, *3D Transient simulations of bubbly flow in an asymmetrically aerated flat bubble column,* Master's thesis, Delft University of Technology (2000).

[5] S. Becker, A. Sokolichin, and G. Eigenberger, *Gas-liquid flow in bubble columns and loop reactors: Part II. comparison of detailed experiments and flow simulations,* Chemical Engineering Science **49**, 5747 (1994).

[6] H. Versteeg and W. Malalasekera, *An Introduction to Computational Fluid Dyanmics: The Finite Volume Method*, 2nd ed. (Pearson Education Limited, Edinburg Gate, Harlow, Essex CM20 2JE, England, 2007).

[7] M. Ishii, *Thermo-fluid dynamic theory of two-phase flow,* (1975).

[8] D. Drew, *Mathematical modeling of two-phase flow,* Ann. Rev. Fluid Mech **15**, 261 (1983).

[9] T. Anderson and R. Jackson, *A fluid mechanical description of fluidized beds,* Ind. Eng. Chem Fundamentals **6**, 527 (1967).

[10] R. Oey, *Gas Liquid flows in a Two-Fluid Formalisms - Modelling and validation of closure relations*, Ph.D. thesis, Delft University of Technology (2005).

[11] *Fluent Theory Guide*, ANSYS-Inc, 15th ed. (2013).

[12] V. Ranade, *Computational Flow Modeling for Chemical Reactor Engineering* (Academic Press, Harcourt Place, 32 Jamestown Road, London NW1 7BY, UK, 2002).

[13] R. Masood and A. Delgado, *Numerical investigation of the interphase forces and turbulence closure in 3D square bubble columns,* Chemical Engineering Science **108**, 154 (2014).

[14] L. Schiller and A. Z. Nauman, Ver. Deut. Ing **77**, 318 (1933).

[15] S. Morsi and A. Alexander, *An investigation of particle trajectories in two-phase flow systems,* Journal of Fluid Mechanics **55**, 193 (1971).

[16] J. Grace, M. Weber, and R. Cliff, *Bubble, Drops and Particles* (Academic Press, 24/28 Oval Road, London NW1, 1978).

[17] A. Tomiyama, I. Kataoka, I. Zun, and T. Sakaguchi, *Drag coefficients of single bubbles under normal and micro gravity conditions,* JSME International Journal, Series B: Fluids and Thermal Engineering **41**, 472 (1998).

[18] O. Simonin and P. Viollet, *Predictions of an Oxygen Droplet Pulverization in a Compressible sub-sonic coflowing hydrogen blow*, Tech. Rep. FED91 (1990).

[19] B. E. Launder and D. B. Spalding, *The numerical computation of turbulent flows,* Computer Methods in Applied Mechanics and Engineering **3**, 269 (1974).

[20] O. Borchers, A. Sokolichin, and G. Eigenberger, *Applicability of the standard k−ϵ turbulence model to de dynamic simulation of bubble columns: Part II. comparsion of detailed experiments and flow simulations,* Chemical Engineering Science **54**, 5927 (1999).

[21] V. Yakhot, S. Orszag, S. Thangam, T. Gatski, and C. Speziale, *Development of turbulence model for shear flows by a double expansion technique,* Physics of Fluids **4**, 1510 (1992).

[22] T. Shih, W. Liou, A. Shabbir, Z. Yang, and J. Zhu, *A new k - ϵ viscosity model for high Reynolds number turbulent flow,* Computers & Fluid **24**, 227 (1995).

[23] B. Launder, G. Reece, and W. Rodi, *Progress in the development of a Reynolds-stress turbulence closure.* Journal of Fluid Mechanics **68**, 537 (1975).

[24] D. Cokljat, M. Slack, S. Vasquez, A. Bakker, and G. Montante, *Reynolds-stress model for eulerian multi-phase,* Progress in Computational Fluid Dynamics **6**, 168 (2006).

[25] B. Daly and F. Harlow, *Transport equations in turbulence,* Physics of Fluids **13**, 2634 (1970).

[26] F. White, *Fluid Mechanics*, Seventh ed. (McGraw-Hill, Avenue of the Americas, New York, NY 10020, 2011).

[27] A. Troshko and Y. Hassan, *A two-equation turbulence model of turbulent bubbly flow,* International Journal of Multiphase Flow **22**, 1965 (2001).

[28] Y. Sato and K. Sekoguchi, *Liquid velocity distribution in two-phase bubbly flow,* International Journal of Multiphase Flow **2**, 79 (1979).

[29] S. Patankar, *Numerical Heat transfer and fluid flows.* (Hemisphere, 1980).

[30] A. Sokolichin and G. Eigenberger, *Gas-liquid flow in bubble columns and loop reactors: Part I. detailed modelling and numerical simulation,* Chemical Engineering Science **49**, 5735 (1994).

[31] R. Oey, R. Mudde, and H. Van den Akker, *Sensitivity study on interfacial closure laws in two-fluid bubbly flow simulations,* AIChE Journal **49**, 1621 (2003).

[32] N. Deen, B. Hjertager, and T. Solberg, *Comparsion of PIV and LDA measurement methods applied to the gas-liquid flow in a bubble column,* in *10th International Symposium on Applications of Laser Techniques to Fluid Mechanics* (Lisbon, Portugal, 2000).

[33] D. Zhang, N. Deen, and J. Kuipers, *Numerical simulation of the dynamic flow behavior in a bubble column: A study of closures for turbulence and interface forces,* Chemical Engineering Science **61**, 7593 (2006).

[34] A. Sokolichin, G. Eigenberger, A. Lapin, and A. Lübbert, *Dyanamic numerical simulation of gas-liquid two-phase flows: Euler/euler versus euler/lagrange,* Chemical Engineering Science **52**, 611 (1997).

[35] R. Mudde and O. Simonin, *Two- and three- dimensional simulations of a bubble plume using a two-fluid model,* Chemical Engineering Science **54**, 5061 (1999).

[36] A. Gupta and S. Roy, *Euler-euler simulation of bubbly flow in a rectangular bubble column:experimental validation with radioactive particle tracking,* Chemical Engineering Journal **225**, 818 (2013).

[37] N. Deen, T. Solberg, and N. Hjertager, *Large eddy simulation of the gas-liquid flow in a square cross-sectioned bubble column,* Chemical Engineering Science **56**, 6341 (2001).

[38] F. Bombardelli, G. Buscaglia, G. Marcelo, and D. Enzo, *Simulation of wandering phenomena in bubble plumes via a k−ϵ model and a large-eddy-simulation(LES) approach.* Mecánica Computacional **23**, 2273 (2004).

[39] A. Tomiyama, *Drag, lift and virtual mass forces acting on a single bubble,* Third International Conference on Multiface FLow. (2004).

[40] B. Niceno, M. Boucker, and B. Smith, *Euler-Euler large eddy simulation of a square cross-sectional bubble column using the neptune cfd code,* Science and Technology of Nuclear Installations **2009**, 1 (2007).

[41] M. Milelli, *A Numerical Analysis of Confined turbulent bubble plumes*, Ph.D. thesis, Swiss Federal Institute of Technology (2002).

[42] M. Dhotre, N. Deen, B. Niceno, Z. Khan, and J. Joshi, *Large eddy simulation for dispersed bubble flows: A review,* International Journal of Chemical Engineering **2013**, 1 (2013).

[43] R. Sungkorn, J. Derksen, and J. Khinast, *Modeling of the turbulent gas-liquid bubbly flows using stochastic lagrangian model and lattice-boltzmann scheme,* Chemical Engineering Science **66**, 2745 (2014).